UNIVERSITY OF CALIFORNIA SAN DIEGO

Structural analysis and mechanical properties of amorphous steel composites

A dissertation submitted in partial satisfaction of the

requirements for the degree

Doctor of Philosophy

in

Materials Science and Engineering

by

Arash Yazdani

Committee in charge:

Olivia A. Graeve, Chair
Nicholas Boechler
Javier E. Garay
Waguih Ishak
Ping Liu
Jian Luo

2020

The Dissertation of Arash Yazdani is approved, and it is acceptable in quality and form for publication on microfilm and electronically:

_____

_____

_____

_____

_____

_____

Chair

University of California San Diego

2020

DEDICATION

I humbly dedicate this work to my parents. I wish there was a more heartfelt way to say thank for everything that you have done for me as no words of gratitude can ever be enough and I promise to work hard every single day of my life to make you proud.

TABLE OF CONTENTS

LIST OF FIGURES

LIST OF TABLES

ACKNOWLEDGEMENTS

I have come a long a way towards completion of my PhD program and it was impossible without Prof. Olivia Graeve's technical and emotional support, her flawless coaching skills and optimistic attitude to overcome difficulties throughout my research profession. No words of gratitude could ever be enough.

I truly appreciate the support from Prof. Günther W.H. Höhne from Germany. A huge part of this research on developing the new methodology using DSC could not fulfilled without his help. All our communications were through the emails and messages, without, unfortunately, any in-person meeting. However, he was so knowledgeable and patient that his insight and comments always helped us to overcome technical and scientific challenges.

Special thanks to Professor Jian Luo, Professor Javier E. Garay, Professor Ping Liu, Professor Nicholas Boechler, and Dr. Waguih Ishak for being part of my committee. I deeply appreciate their support and valuable advice.

Moreover, I would like to thank our research scientist and lab assistant Dr. Ekaterina Novitskaya (Katya) for all her help during my PhD program as she truly helped me with various aspects of my research and instruments.

I would like to thank Prof. Javier E. Garay, Prof. David Kisailus, Prof. Marc Meyers, and Joseph Magallanes who provided us with their scientific insight as well as their lab facilities and various instruments.

I also would like to thank Darren Dewitt, Wei Huang, Haocheng Quan, and Huiyang Luo for their help with sample preparation, mechanical testing and intellectual discussion.

Lastly, and most importantly, I would like to thank my parents, and family members for their endless encouragements and support. Everything that I have achieved and what I have become so far, and all my future achievements are only possible because of you.

Chapter 3, in part, is a reprint of the material as it appears in PLOS ONE 2020. A. Yazdani, G.W.H. Höhne, S.T. Misture, and O.A. Graeve. The dissertation/thesis author was the primary investigator and author of this paper.

Chapter 3, in part is currently being prepared for submission for publication of the material. A. Yazdani, D. Dewitt, W. Huang, R. Borja-Urby, H. Luo (Karagozian & Case, Inc.), J. Magallanes (Karagozian & Case, Inc.), D. Kisailus, J. E. Garay, O. A. Graeve. The dissertation/thesis author was the primary investigator and author of this material.

VITA

2007	Bachelor of Science, Iran University of Science and Technology (IUST)
2010	Master of Science, Iran University of Science and Technology (IUST)
2016-2020	Teaching Assistant, University of California San Diego
2020	Doctor of Philosophy, University of California San Diego

SELECTED PUBLICATIONS

O.A. Graeve, A. Yazdani, J.P. Kelly, R. Kanakala, and J. Tinsley, "Effect of SiO_2 on the Sintering of Cerium-doped Lutetium Oxyorthosilicate," *Optical Materials*, **100**, 109650 (2020).

A. Yazdani, G.W.H. Höhne, S.T. Misture, and O.A. Graeve, "A Method to Quantify Crystallinity in Amorphous Metal Alloys: A Differential Scanning Calorimetry Study," *PLOS ONE*, **15** [6] e0234774 (2020)

A. Yazdani, D. Dewitt, W. Huang, R. Borja-Urby, H. Luo (Karagozian & Case, Inc.), J. Magallanes (Karagozian & Case, Inc.), D. Kisailus, J. E. Garay, O. A. Graeve, "Effect of Crystallinity on The Mechanical Properties of an *in situ* Amorphous Steel Matrix Composite", In preparation.

A. Yazdani, O.A. Graeve, "A critical review: Mechanical Properties of High Entropy Alloys and Ceramics", In preparation.

A. Yazdani, C. Bagon, O.A. Graeve, "Stability and thermal conductivity of nano fluids", In preparation.

ABSTRACT OF THE DISSERTATION

Structural analysis and mechanical properties of amorphous steel composites

by

Arash Yazdani

Doctor of Philosophy in Materials Science and Engineering

University of California San Diego, 2020

Professor Olivia A. Graeve, Chair

In the first part of this research, we developed a differential scanning calorimetry method for calculating the initial crystallinity, change of crystallinity and crystallinity percentage of amorphous metal alloys as a function of temperature. Using thermodynamic enthalpies of amorphous, crystalline and partially devitrified specimens, our methodology can determine crystallinity percentages as low as a few percent. This technique also eliminates the need for expensive *in situ* accessories, such as those required in electron microscopy. In the second part, we report the effect of crystallinity percentage on the compressive deformation response of partially devitrified *in situ* Fe-based bulk metallic glass matrix composites (SAM2×5-Dev), consisting of an amorphous matrix and evenly dispersed nanocrystals (BCC iron, carbides, and borides) of sizes smaller than 20 nm. The SAM2×5-Dev specimens were obtained by consolidating SAM2×5 powders using the spark plasma sintering technique. The crystallinity percentage of the sintered samples varied between 20% and 61% depending on the sintering temperature. Macroscopically, bulk samples tested under compression exhibited an ~8% elastic

deformation, which is significantly higher than elastic strains of other Fe-based bulk metallic glass composites, and strengths of ~2 GPa at fracture. Indentation toughness of the samples was below 1.6 MPa•$m^{0.5}$, which categorizes the material as a brittle composite. Compression tests on micro-pillars resulted in specimen failure from the propagation of one principle shear band. Here, yield strength was corrected for the effect of taper angle of the micro-pillars and values above 5 GPa were obtained, making the material an ultra-hard composite. Such a high strength is attributed to the extremely small Poisson's ratio (< 0.1) and higher glass transition temperature (883 K) of this material Both the compressive strength and fracture toughness of the specimens were negligibly dependent on the crystallinity percentage, implying that the radii of the plastic zones at the crack tips are smaller than the distance between nanocrystals on the specimens. Moreover, we find that SAM2×5-Dev shows a very high sample size dependency of strength (above 200%), which indicates a significant defect sensitivity. As a result, the residual porosity despite being minimal, strongly deteriorates the strength of the materials.

Chapter 1

Bulk metallic glasses (BMGs): Structure, fabrication and mechanical properties

1. Introduction

1.1. Amorphous metallic alloys

Crystalline solid-state materials with a variety of chemical bonds, including van der Waals, hydrogen, covalent, ionic, and metallic, could be transformed into amorphous phase if an appropriate technique is applied [1, 2]. Historically, rapid cooling (quenching) from the liquid state will result in the formation of an amorphous material which is called glass. The term "amorphous" refers to the lack of translational symmetry in their atomistic configuration [2]. The process of amorphization (vitrification) of the liquid has been the main approach to obtain a glass. The cooling rate which yields a glass, strongly depends on the material itself and incorporated technique. According to one of the wildly accepted definitions, metallic glasses (MG) could be introduced as disordered atomic-scale structural arrangement of atoms formed as a result of rapid cooling of complex alloys system directly from their melt state to below room temperature with a large undercooling and a suppressed kinetics in such a way that supercooled state is retained [3-5]. Amorphous microstructure of metallic glasses accompanied by metallic bonds create an exceptional structural and functional properties superior to their crystalline counterparts. That is the reason that recently, a great deal of attention has been dedicated towards understanding and modeling the microstructure of metallic glasses and explore their unique characteristics for engineering applications [6-9].

Glasses are formed via amorphization process during which the liquid id fast-cooled or quenched. However, if the quench rate is not high enough, system kinetics allows the crystalline phase to nucleate below the melting temperature (T_m) and consequently, the liquid transforms into a crystalline solid. In another scenario, if the quench rate of liquid is sufficiently high, the

nucleation process in the liquid will be hampered. Consequently, the liquid phase could be cooled be cooled down below T_m with crystallization has been impeded. Existence of liquid below melting temperature takes place since the liquid is in the supercooled state which is a metastable one compared to the crystalline state. As the cooling of a supercooled liquid proceeds, its viscosity increases until, at a certain temperature below T_m, the viscosity of supercooled liquid reaches the value around 10^{12} Pa.s (10^{13} Poise) which is almost 14-15 orders of magnitude higher than that of the same liquid at T_m. This threshold temperature is conventionally called glass transition temperature, T_g, where atomic structure of the supercooled liquid remains almost unchanged [10]. In the rapid quenching process, the critical cooling rate (R_c) is the minimum cooling rate that impedes the crystallization of liquid. In another expression, critical cooling rate is a measure of glass forming ability (GFA). An alloy with a smaller R_c, has a better GFA than an alloy with a larger R_c. Also, the cooling rate and sample dimension (thickness) are related. As a result, R_c is associated with the critical thickness (d_c) which is the maximum thickness of the part that can yield a glassy sample from an arbitrary alloy [2, 10].

Compared to inorganic/oxide glass forming materials, pure metals and alloy systems, upon quenching, crystallizes much easier. That is why the fabrication of glassy metals and alloys is significantly harder than the manufacturing of inorganic glasses. Klement *et al,* [11] applied a very fast cooling rate of 10^6 K/s to form the first metallic glass from Au-Si alloy and succeeded to produce a small piece with dimension of 50 μm. in order to produce a glassy specimen from many of alloys and elements, very fast cooling rates of 10^5 to 10^{10} K/s is needed. These metallic glasses (MG) are called conventional metallic glasses. Metallic glasses could be classified based on different criteria such as their main alloying component, nature of their constituent elements, and their GFA. More information has been provided in the future sections.

Contrary to conventional MGs with critical thickness in the range of sub-millimeter, there is another group of amorphous alloys that have goof GFA and from which samples with a thickness up to 1mm could be cast. This category of amorphous alloys is bulk metallic glass (BMG) [12]. The first BMG was produced using Pd-Cu-Si alloy system with a cooling rate of 1000 K/s [12]. After that, parts with thickness of one centimeter were produced from Pd-Ni-P alloy system using a small cooling rate of 10 K/s [13, 14]. However, these parts had a significant thickness, the use of expensive Pd restricted their manufacturing to the laboratories. Inoue *et al.,* in the late 1980s, systematically investigated the GFA in ternary systems of Fe and Al metals with rare-earth elements and obtained exceptional BMGs such as La–Cu–Al samples with thicknesses of several millimeters and low critical cooling rates [15, 16]. Based on these findings, quaternary and quinary BMGs, such as La–Al–Cu–Ni, were synthesized with low cooling rates of less than 100 K/s. Further research revealed similar BMG forming alloys designed by partially replacing the rare-earth metals with Mg (an alkaline metal), such as Mg–Cu-Y, Mg–Ni-Y, etc., [17], along with a family of multicomponent Zr-based BMGs, such as Zr–Cu–Ni, Zr–Cu–Ni–Al [18].

1.2. Three rules

Formation and stability of bulk metallic glasses could be explained by their ability to retain their glassy state at room temperature after being cooled down or quenched. Although the knowledge about amorphous microstructure had been gained much earlier, it was quit challenging to obtain homogeneous, uniform glassy structure across the whole thickness of part at room temperature until recently. Back in days, alloys with a very narrow compositional window cooled at very high cooling rates could form amorphous microstructure [11, 13, 19]. Any deviation from

these parameters could end up with crystallization. This requirement to form an amorphous structure is called glass forming ability (GFA) [20]. GFA is a crucial factor which affect the formation and evolution of amorphous alloys. There has been a considerable amount of research on enhancement of GFA of variety of systems [21-23] by changing the chemical composition of alloys and processing conditions [7, 24, 25]. Nowadays, amorphous alloys with multicomponent composition can be cast even at slow cooling rate owing to their superior GFA [23, 26-29]. A significant amount of research has been carried out to analyze and quantify the glass forming ability of different alloy systems which all ended up with three basic rules which are universally accepted for the formation of any BMG system [30]. Any glass forming system consisting of multiple elements must:

1- Have at least three elements.
2- Have three elements whose atomic size difference is larger than 12%. Larger atoms are assumed to enhance the GFA of alloy system.
3- Have a negative mixing enthalpy among three elements. This criterion ensures the retention of amorphous structure at room temperature.

Generally, the chemical composition of bulk metallic glasses is formulated based on (1) alloy systems that show a deep eutectic which decreases the extent of undercooling required to obtain liquid, and (2) alloys that exhibit a large atomic mismatch which creates lattice stresses that postpone crystallization [30].

1.3. Classification of MGs

Inoue *et al*, [25, 31] classified bulk metallic glasses into three different categories:

1- Metal-metal type

2- Pd-metal-metalloid type

3- Metal-metalloid type

This classification is based on how easily one group of elements can react with other groups of elements in order to form a glassy structure. The criteria that have been considered for this classification include chemical affinity, atomic size, electron configuration and so forth. The proposed atomic arrangement, size, and crystal structure are depicted in **Figure 1**. Metal-metal amorphous alloys consist of icosahedral-like ordered atomic configurations. Zr-Cu-Al-Ni and Zr-Cu-Ti-Ni-Be are two commons examples of this type of BMG. Pd-transition metal-metalloid type glassy alloys have highly dense and packed configurations of two types of polyhedral of Pd-Cu-P and Pd-Ni-P atomic pairs. Typical examples of this category are Pd-Cu-Ni-P systems. *Metal–metalloid type* amorphous alloys have network-like atomic configurations in which a disordered trigonal prism and an anti-Archimedean prism of Fe and B are connected to each other. In this configuration, the face and edge are shared through connecting atoms of Ln and early transition metals (ETM) of Zr, Hf, and Nb. Fe–Ln–B and Fe–(Zr, Hf, Nb)–B ternary systems are typical examples for this category of glassy alloys. These icosahedral-, polyhedral-, and network-like ordered atomic configurations can effectively suppress the long-range rearrangements of the constituent elements that are necessary for onset of crystallization process. Among the three structures described, the second and third types are similar in a sense that they both contain trigonal prism structure but are different in that the latter forms a well-developed connected structure of prisms by sharing their vertices and edges, which results in highly stabilized supercooled liquid leading to the formation of bulk metallic glass even at very slow cooling solidification processes [25]. Bulk metallic glasses could be also classified from an engineering point of view which is

based on their applicability. They could be categorized into seven different types which could be further divided into two main types according to their behavior in phase diagram. These two groups include:

1- Host-metal based type: Zr–Cu–Al–Ni, Fe–Cr–metalloid, Fe–Nb– metalloid, and Fe–Ni–Cr–Mo–metalloid systems.

2- Pseudo-host metal based type: Zr–Cu–Ti–Ni–Be, Zr–Cu–Ti–(Nb, Pd)–Sn, and Cu–Zr–Al–Ag systems.

It can be seen that from the viewpoint of application, Fe- and Zr-based bulk metallic glasses are the two most important groups of BMGs. Zr-based BMGs could be further classified into subgroups whose details are available in the literature [25].

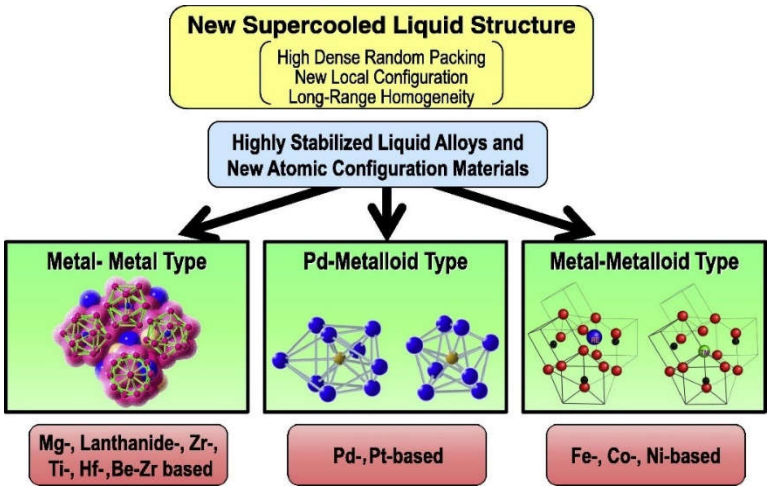

Figure 1. Schematic illustration of structural features of different categories of glassy alloys [25].

1.4. Structure of MGs

For decade since the discovery of metallic glasses, the precise atomic configuration of metallic glasses has been the topic of many debates. Transmission electron microscopy (TEM) is

powerful characterization method that has significantly contributed to resolve this issue. Figure 2 a and b are TEM images of a prototypical crystalline metal and metallic glass, respectively, which illustrate the difference between atomistic packing in these two states. TEM micrograph of crystalline alloy (Figure 2 a), clearly shows the long-range order (LRO) packing which is discerned via translational symmetry of atoms within well-defined crystal planes. However, when it comes to amorphous glass, TEM image (Figure 2 b) cannot reveal any distinguishable structure or order [32]. Selected area electron diffraction (SAED) patterns of crystalline and amorphous alloys are also presented in the inset of Figure 2 a and b, respectively. The SAED pattern for the crystalline alloy shows a set of sharp and bright spots, each of which is the result of strong interference peaks that originate from long-range ordering (LRO) of similar crystalline planes. However, in the absence of LRO in the glassy material, the interference peaks are smeared out and create diffuse halos. Although such a pattern of diffusive halos is a signature of metallic glasses, it does not provide further information on details of their atomic structure [2].

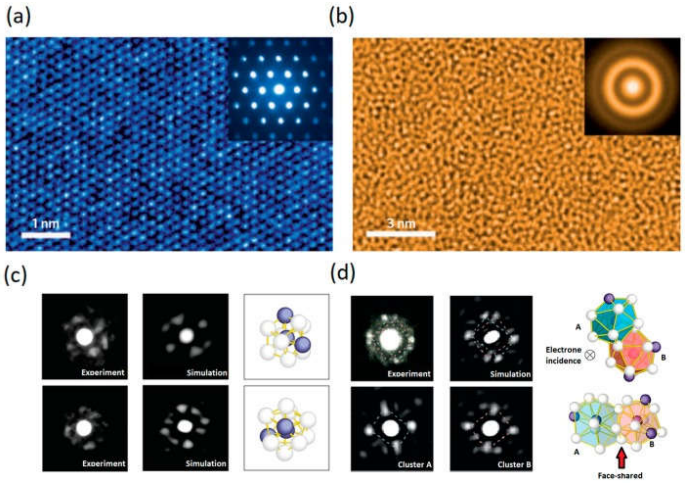

Figure 2. Atomic resolution TEM image of (a) crystalline low-carbon steel showing well-defined and long-range order packing of lattice planes. The corresponding selected-area electron diffraction (SAED) pattern reveals sharp crystalline spots; and (b) a $Zr_{67}Ni_{33}$ metallic glass, illustrating a prototypical maze-like pattern in MGs. The corresponding SEAD pattern of MG exhibits diffusive haloes; and (c, d) Nanometer diameter electron beam diffraction revealed the short- and medium-range order in MGs [32, 33].

In addition to incorporating experimental methodologies to study the amorphous microstructure of metallic glasses, a great deal of time and effort has been spent on modeling and simulation [34-37] as comprising interpenetrating quasi-equivalent clusters, i.e., coordination polyhedral, as initially had been suggested by Kasper and Frank, to model the structure of complicated alloys [38, 39]. According to this very first model, each atom in the glassy alloy is surrounded by a preferred number of neighboring atoms. These atoms are arranged in their nearest neighbor shell with a preferred chemical composition. These local atomic configurations at the length scale of nearest neighbor shell define the short-range order (SRO) motifs of the MGs [40, 41]. These SRO clusters then connect, and even overlap, with each other throughout the glassy alloy and form different arrangements beyond the nearest-neighbor shell, on a scale of a few to almost 10 Å, which is known as medium-range order (MRO).

The SRO- and MRO-based model of the MG structure has been strongly supported by realistic computer modelling based on first principles calculations and large-scale molecular dynamics simulations [37, 41-47] and has successfully and extensively been applied to explain experimental observations [45, 47, 48]. Recently, nanobeam electron diffraction (NBED) experiments with the help of a sub nanometer diameter electron beam has been employed for direct observation of SRO and MRO structures in MGs (Figure 2 c and d) [33].

1.5. Mechanical properties of BMGs

The nature of atomic bonds in both glassy and crystalline metallic alloys is very similar since the metallic bonds are the dominant bonds in these materials. However, it should be noted that despite the similarity of atomic bond's nature in glassy and crystalline metallic alloys, metallic

glasses have significantly superior mechanical properties than their crystalline counterparts which is due to the lack of grain boundaries [2].

1.5.1. Strength

Metallic glasses, compared to their crystalline counterparts, have a significantly higher hardness and strength which are very close to the theoretical values for these materials. Also, it has been shown that (bulk) metallic glasses have an extraordinarily high resiliency and elastic limit which makes make outstanding candidates for applications which require adsorption a high amount of elastic energy per unit volume [49]. It is believed that such unique mechanical behaviors of metallic glasses raise from their amorphous nature and lack of translational symmetry in their atomic structure which lead to the absence of well-defined crystallographic slip systems and dislocation-mediated yield mechanisms. Lack of dislocation in the metallic glasses caused them to show high yield strength very close to the theoretical limit and about 2.6% of elastic deformation at room temperature [2, 50]. On the other hand, metallic glasses severely suffer from lack of tensile ductility and fracture toughness (some of MGs) at room temperature which remarkably limit their structural and engineering applications.

1.5.2. Elastic properties

As mention previously, lack of slip system in metallic glasses results in very high strength which is close to the theoretical value. Researchers have shown that the elastic moduli of the atomic nearest-neighbor shell in metallic glasses are similar to those of corresponding metallic

crystals [49, 51]. However, topological instabilities taking place under loading due the lack of long-range order can lead to the local anelastic deformations which emerges macroscopically as reduced stiffness and smaller Young's modulus (E) compared to the crystalline counterparts [51]. That is the reason that metallic glasses have an unusual combination of high yield strength (σ_y) and low Young's modulus (E). Mechanical properties of some of well-known metallic glasses are compared with more than 1500 engineering alloys and other materials and the results are shown in Figure 3. Also, in this figure, contours for yield strain (σ_y/E) and the resilience (σ^2_y/E) are shown. Interestingly, most of the metallic glasses show an elastic strain limit of about 2,67% which is significantly high. Resilience indicates the ability of mechanical damping which is the capacity of material to store the elastic energy per unit volume. Higher resilience leads to a lower loss coefficient in cyclic elastic loading which represents the contribution of local plastic flow in the energy loss [52]. According to Figure 3, most of metallic glasses are very resilient materials.

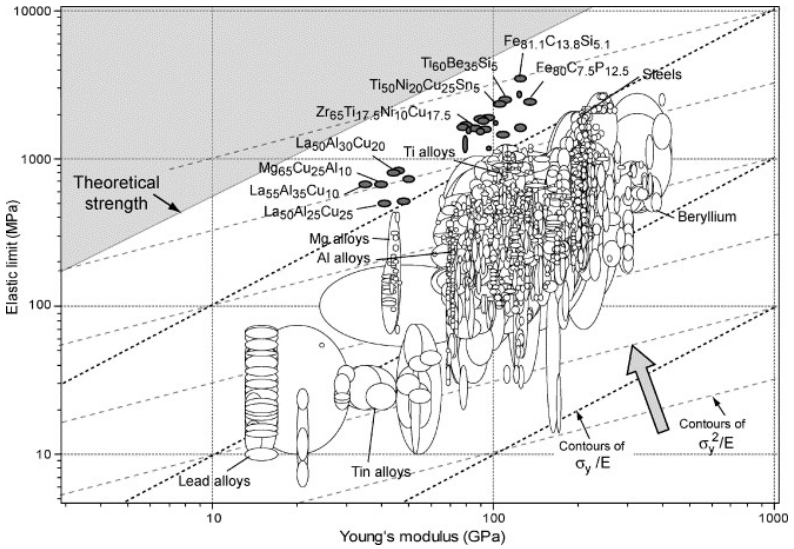

Figure 3. Elastic limit (σ_y) versus Young's modulus (E) for 1507 metals, alloys, metal matrix composites and metallic glasses. The contours represent the yield strain (σ_y/E) and the resilience (σ^2_y/E) [52].

Combination of high elastic strain and resilience of metallic glasses nominates them as ideal candidates for diverse applications such as elastic pressure gauges, flowmeters, sports goods and nano scale devices [49, 53-55]. Additionally, exceptional resilience along with low loss coefficient make metallic glasses appealing for vibrating-reed systems such as fast- acting springs, gyroscopes and elastic wave transmission [52].

1.5.3. Plastic properties

Although absence of crystalline structural defects such as dislocations and slip systems grants metallic glasses exceptional yield strength and elastic properties, it negatively affects their plastic deformation after yield strain. At room temperature and under quasi-static deformation regime, (bulk) metallic glasses yield almost zero tensile plasticity and fail catastrophically which is very similar to the behavior of brittle materials such as conventional glasses [56, 57]. However, metallic glasses and conventional brittle glasses have pronounced differences when their fracture surfaces are explored [58]. Firstly, the tensile fracture cross section of metallic glasses has a degree of about 45^{o} with regards to the loading axis since it provides the plane with the maximum resolved shear stress. But when it comes to brittle glasses, the fracture plane is perpendicular to the loading axis (Figure 4a). Secondly, Though metallic glasses shows catastrophic failure under tensile loading, their fracture surface has characteristics of vein or river patterns (Figure 4a) [59, 60]. The abnormality of showing brittle catastrophic failure under tensile loading while the fracture surface yields vein pattern which belongs to ductile deformation could be explained by the unique deformation mechanism which dominate the deformation of metallic glasses. In (bulk) metallic

glasses, the plastic deformation is severely localized in microscopically narrow bands which are called shear bands [56, 57, 61-67]. We discuss them more in the next part.

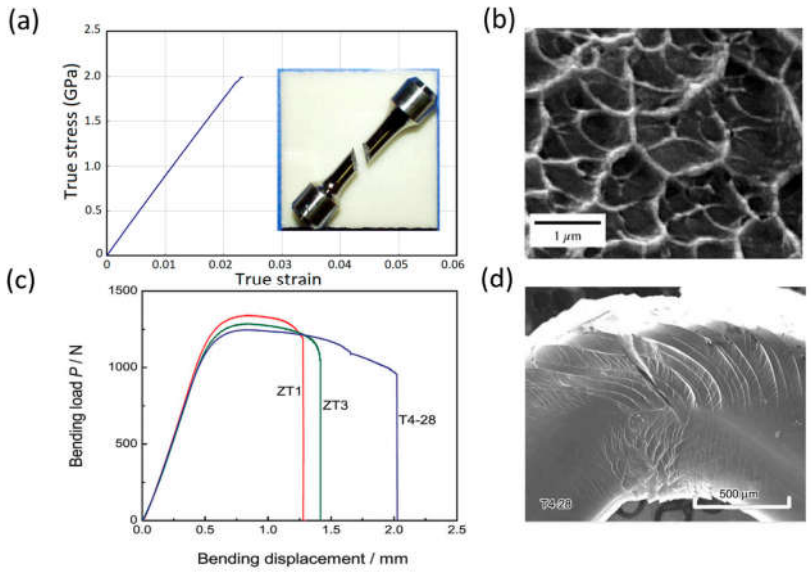

Figure 4. Room temperature ductility and failure of metallic glasses under different loading conditions. (a) A typical tensile fracture in bulk metallic glasses with almost zero plasticity. The inset shows the formation of the principle shear band with the angle of 45 degrees with regards to the tensile loading axis. (b) Vein morphology of fracture surface which corresponds to the stress-strain curve shown in (a). (c) Large bending plasticity observed for a Zr-based bulk metallic glass with different chemical compositions. (d) Formation of multiple shear bands which leads to the extensive bending ductility shown in (c) [2, 9].

1.6. Deformation and failure mechanisms in bulk metallic glasses (BMGs)

As mentioned previously, bulk metallic glasses have elastic modulus which is the same order of magnitude as that of crystalline counterparts, however their room temperature strength is significantly higher. Also, there is nothing such as strain hardening, and their plastic deformation is governed by shear and normal stresses. Deformation in bulk metallic glasses takes place heterogeneously through plastic strains restricted in localized shear bands. However, at high temperatures and under low stresses, BMGs show stable Newtonian flow [68]. Lund and Schuh [69] have suggested that macroscopic yield and failure of metallic glasses include many small-

scale events such as (1) nucleation of shear transformation zones in which atoms accommodate the applied shear stress, (2) propagation of shear bands [70, 71], (3) adiabatic heating in localized deformed regions [72-75], (4) nucleation of nano crystallites inside or near the shear bands [74, 76-78], (5) nucleation of nano voids inside the shear bands [79, 80], and (6) coalescence of voids leading to the failure [81]. In the following, the main features of deformation and failure mechanisms and their influence on the mechanical response of metallic glasses would be reviewed.

1.6.1. Plastic flow and deformation response

There have been numerous mechanistic studies on exploring the deformation behavior of BMGs. It is known that under an applied stress, the shear strain, at the atomic scale, is accommodated via local rearrangements of atoms around free volume regions. This rearranging theory which was proposed by Argon [82], introduces two different modes of thermally-activated shear transformation. At temperatures between $0.6T_g$ and T_g, the transformation involves diffuse rearrangements of atoms with small shear strain in spherical regions whose diameter is of five-atom diameter. At temperatures below $0.6T_g$, the transformation proceeds through the formation of narrow disk-shaped volume element which is called shear transformation zone (STZ) which is very similar to the formation of dislocation loop in crystalline materials. The fundamental unit of plasticity during the inhomogeneous deformation of BMGs could be the shear transformation zone or the free volume for local diffusive jumps. As illustrated in Figure 5a [83], shear transformation zones (STZs) are basically tiny clusters of closely-packed atoms and cooperatively rearrange to accommodate the applied shear strain [69, 70, 82, 84]. STZ will experiences an inelastic shear distortion from an initial to final equilibrium state by passing through an intermediate activated

state of high-energy and large volume. As shear strain is continuously applied, the STZ creates a localized distortion of surrounding atoms which initiates the formation of large planar bands of STZs or so-called shear bands [83]

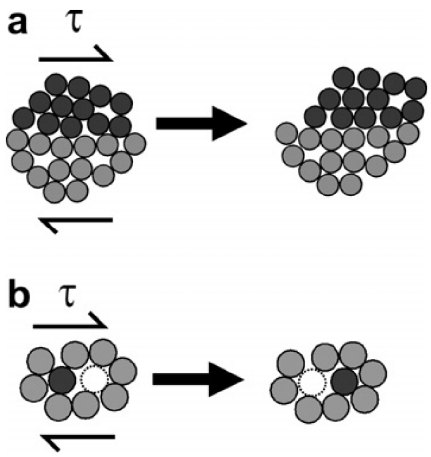

Figure 5. Two different mechanisms proposed for deformation of bulk metallic glasses at room temperature. (a) Formation of shear transformation zone and (b) local atomic jump [83]

Spaepen [70] proposed another model to describe the deformation of BMGs which is based on free volume model [85]. According to Saepen's model, deformation in BMGs takes place as a series of diffusion-like local atomic jumps into vacant sites in regions of large free volumes (Figure 5b) [83]. It is clear that the activation energy for strain accommodation through atomic jumps is smaller than that for distortion of STZ. A significant amount of effort has been put into modification and improvement of these two commonly used models. For instance, Steif *et al.* [84] modified Spaepen's model by including additional free volume change due to pressure. Khonik [86] proposed a directional structural relaxation model suggesting that each rearrangement event can be interpreted as a thermally-activated shear due to local atomic structures and subsequently nearly athermal viscous flow by external stress. There are other models that use different concepts

to depict the deformation mechanism and strain accommodation in BMGS. However, Spaepen's [70] and Argon's [82] models are the most popular ones yet.

1.7. Amorphous steel

1.7.1. Discovery of Fe-based metallic glasses (MGs)

Duwez *et al*, [87] introduced the first iron-based metallic glasses based on Fe-P-C systems around 1967. Conventional Fe-based metallic glasses are commonly fabricated in the form of powders, ribbons or wires which require quenching metallic melt at cooling rates beyond 10^6K/s. Iron-based metallic glasses, compared to their crystalline counterparts, have a cheaper production cost, lower coercive force, higher saturation magnetization which combined make them ideal candidates for high-performance soft magnetic materials for energy saving [88]. Therefor, seeking new Fe-based metallic glasses with enhanced magnetic properties has been the topic of many researches. As a result, a variety of iron-based metallic glasses like Fe-P-B [89] and (Fe,Co, Ni)-Si-B [90] were developed. Nowadays, some of these Fe-based metallic glasses such as FINEMET, NANOPERM and HITPERM have been successfully commercialized owing to their excellent soft magnetic properties [91]. Nevertheless, their low GFA limits the thickness of these alloys' ribbon to less than 50μm which leads to a low packing density of the transformer core and increase the Joule losses [92].

1.7.2. Discovery of Fe-based bulk metallic glasses (BMGs)

Inoue *et al*, [93] introduced the first Fe-based bulk metallic glass with a chemical composition of $Fe_{73}Al_5Ga_2P_{11}C_5B_4$ in 1995. Typical XRD patterns and DSC heat flow graphs of $Fe_{73}Al_5Ga_2P_{11}C_5B_4$ bulk metallic glass produced with different thicknesses are shown in Figure 6. Regardless of cast part's thickness, the large halo peak in XRD pattern confirms the amorphous nature of rods. Also, casting in the form of either ribbons or rods does not significantly change the glass transition temperature and the onset temperature of crystallization [93].

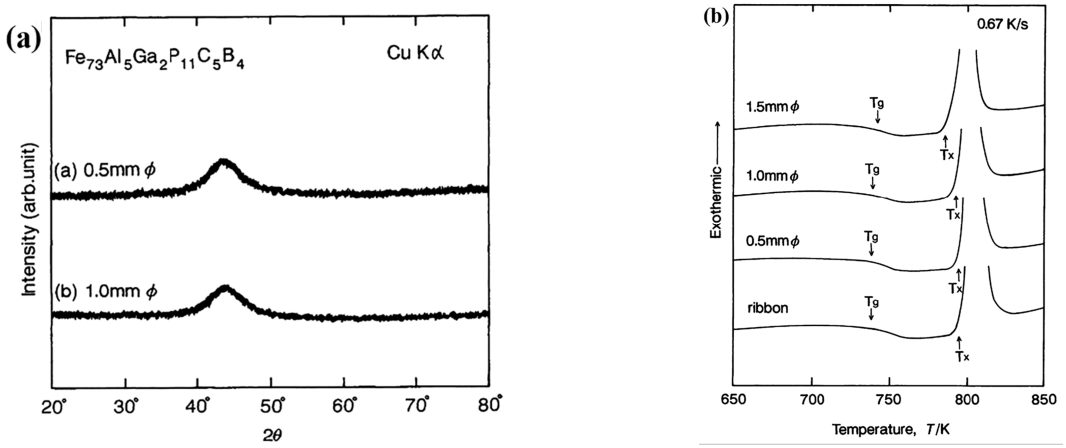

Figure 6. Typical (a) XRD patterns and (b) DSC thermograms of amorphous $Fe_{73}Al_5Ga_2P_{11}C_5B_4$ rods with different diameters produced via injection casting method [93].

After Inoue's discovery, more researchers started to look into finding large-sized Fe-based BMGs which ended up with introduction of new systems such as Fe-(Nb, Cr, Mo)-(Al, Ga)-(P, B, C) [94], Fe-Co-(Zr, Hf, Nb)-(Mo, W)-B [95], Fe-Co-Nd-Dy-B, Fe-Co-Ga-(P, C, B) [96], Fe-(Co, Cr, Mo, Ga)-(P, C, B) [97], Fe-Ni-P-B [98], and Fe-B-Si-(Zr, Nb) [99] from which parts with critical diameter between 1 and 6 mm were be successfully produced. It was around 2004 that centimeter-sized Fe-based bulk metallic glasses were produced by addition of Er [100] and Y

[101]. The largest Fe-based bulk metallic glass with a chemical composition of $(Fe_{0.8}Co_{0.2})_{47}Cr_{15}Mo_{14}C_{15}B_6Tm_3$ and a thickness of 18 mm was successfully produced in 2013 [102]. Today, there are more than ten types of centimeter-sized Fe-based BMGs and they are all based on Fe-C-B alloys. Interestingly, the largest GFA, reported so far, for Fe-based BMGs (which is 18 mm), is still below that of Pd-[103], Zr-[104], Ti-[105], La-[106], Cu-[107], Mg-[108], Ni-[109], and Pt-based bulk metallic glasses [110].

Although GFA has been a crucial criterion for development of Fe-based BMGs, cost reduction has been another issue which helped the widespread application of this type of material. With this regard, several approaches have been proposed, including: (1) fabricating Fe-based BMGs using industrial raw materials, (2) minimizing the total amount of alloying elements, (3) excluding expensive RE elements, and (4) fabricating Fe-based BMGs under low vacuum conditions or even in air without any inert gas protection. Another important factor is improving the performance of Fe-based BMGs. For the applications which do not concern their magnetic properties, room-temperature brittleness has strongly limited the industrial application of amorphous steels. In contrast to other types of BMGs such as Zr-based ones, the amorphous steels yield brittle fracture response and most of the time they fragment under quasi static deformation regime. Their behavior is very similar to that of ceramics. Hence, a significant amount of research has been devoted to increase the ductility/plasticity of amorphous steels through formation of composite microstructures, manipulating the atomic bonding in the amorphous matrix, controlling the intrinsic elastic properties, and geometric refinement [111-116]. Fe-based bulk metallic glasses also take advantage of other unique properties such as excellent corrosion resistance, good wear resistance, high hardness, ion radiation resistance, and decent catalytic characteristics [102, 117].

1.8. Glass formation and GFA

1.8.1. Mapping the GFA

Enhancement of GFA or the critical thickness of the parts which could be produced with an amorphous nature has been the bottleneck of developing Fe-based BMGs since they have been discovered. One of the guidelines for achieving this goal is theory proposed by Greer in 1993 which is known as confusion theory according to which the GFA of BMGs increases as the number of constituent elements of the amorphous alloy increases. And the reason is the existence of more elements in the chemical composition of an alloy will postpone the crystallization during quenching process [118]. Now, it could be clearly understood that why the majority of Fe-based BMGs with a higher GFA have 4 up to 9 elements in their chemical composition. However, there are systems in which there is below four elements and still they have the capability of producing bulk parts. $Fe_{80}P_{13}C_7$ [119], $Fe_{66}Nb_4B_{30}$ [120], and $Fe_{80}P_{11}C_9$ [121] are some of the examples of such systems. Another theoretical guideline for predicting the GFA of bulk metallic glass systems was proposed by Inoue [122]. Their theory which is known as “three empirical rules” has been introduced earlier. It should be noticed that these theories, even combined, can provide us some helpful guidance in developing new classes of BMGs. The process of glass formation, by itself, is a complex one. Also, there are many other factors which play an important role and include chemical composition of alloy, mutual interactions among constituent elements, atomic size of element, and production method. Quantifying the contribution of each of these factors in predicting GFA of BMGs is very hard. This issue becomes harder when Fe-based BMGs are considered since they have relatively lower GFA. Consequently, it seems that the process of fabrication of amorphous steels is mainly based on the “trial and error” approach. Recently, Sun *et al*. proposed

a model which is based on applying support vector machine (SVM) method which can predict the GFA of binary metallic alloys from random compositions [123]. Figure 7 illustrate the flowchart which shows the complete modeling steps which basically consists of four main steps. These steps include building the data set, SVM learning process, model evaluation, and model prediction [123]. According to their results, their model has a high accuracy in identification of good glass formers. However, its performance could be enhanced by refining the input description selection.

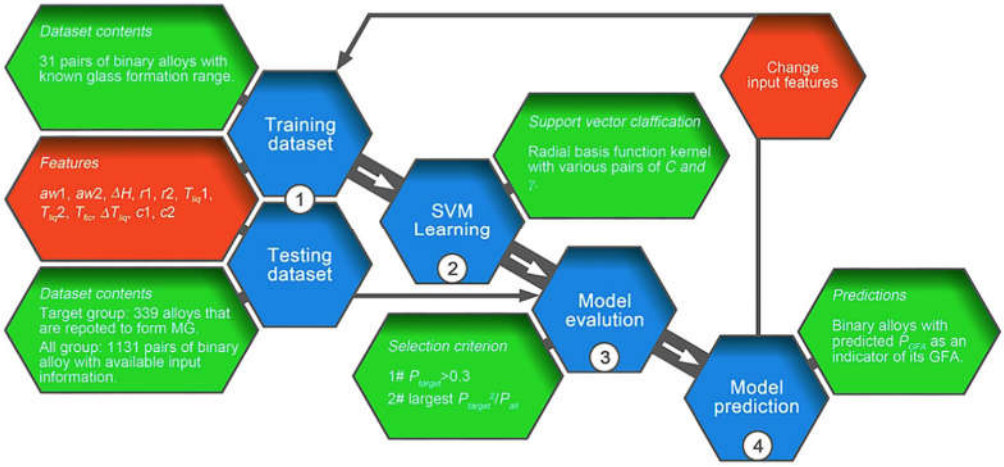

Figure 7. A schematic illustration of steps in SVM modeling process [123].

1.8.2. Thermodynamics of glass formation

From the point of view of thermodynamics, bulk metallic glasses show a weak driving force for crystallization in the supercooled region. Also, the driving force for crystallization could be calculated by the Gibbs free-energy differences between undercooled liquid and crystalline solid ($\Delta G_{l\text{-}s}$) which is expressed using the following Equation [124, 125]:

$$\Delta G_{l-s}(T) = \Delta H_f - \Delta S_f T - \int_T^{T_f} \Delta C_p^{l-s}(T) dT + T \int_T^{T_f} \frac{\Delta C_p^{l-s}(T)}{T} dT \quad (1)$$

Where ΔH_f is the fusion enthalpy at T_f, ΔS_f is the fusion entropy at T_f, and there is a relationship of $\Delta H_f = T_f . \Delta S_f$. T_f is the temperature at which Gibbs free energies of crystalline and undercooled liquid are equal which is often approximated to be the melting point (T_m) [124-127]. ΔC_p^{l-s} is the difference between the specific heat capacities at undercooled liquid and crystalline solid states which could be measured by thermal analysis. A small ΔG_{l-s} is associated with a small ΔH_f and a large ΔS_f. Given an alloy system, when the number of alloying elements increases, the fusion entropy increases as well. Also, decrease in fusion enthalpy and solid/liquid interface energy is favorable. Therefore, a relatively small Gibbs free-energy difference is assumed to be a strong factor affecting the high GFA. There are numerous reports trying to interpret the change of GFA of amorphous steels with regards to thermodynamics [127-130]. For instance, Shen *et al*, [127] calculated ΔG_{l-s} for $Fe_{48-x}Co_xCr_{15}Mo_{14}C_{15}B_6Y_2$ (x = 0, 3, 5, 7, 9) BMGs which turned out to be 1.6 and 2 kJ/mol at $0.8T_m$ for Co7 and Co-free alloys, respectively. They claimed that the excellent GFA of Co7alloy originates from its lower Gibbs free-energy difference between the supercooled liquid and crystalline solid states [127]. However, there are some systems that do not follow this trend [129].

1.8.3. Kinetics of glass formation

When the viscosity of a liquid increases, the intrinsic resistance to atomic diffusion also increases which leads to the enhancement of time scale for atomic movement. In this case where the crystallization is sluggish, the undercooled liquid can vitrify. In other words, viscosity plays a

key role in GFA of bulk metallic glasses [131-133]. The change of viscosity as a function of temperature around glass transition temperature is called fragility (m). Depending on the bonding structure and the way that bonds break down upon heating, glass forming melts could be categorized as strong liquids (m=20-40), intermediate liquids (m=40-60), and fragile liquids (m=60-150). Most of bulk metallic glass formers sit in intermediate liquids group. Hyun Na *et al*, [134] studied the vitrification behavior of five different Fe-based bulk metallic glass formers and stablished a relationship between the critical cooling rate and fragility of these liquids (Figure 8). Fragile Fe-based BMGs have a smaller critical cooling rate. Also, when the fragility of liquid decreases, the GFA enhances which could be interpreted by the enhancement of liquid rigidity with decreasing the temperature in such a way that crystallization process is postponed.

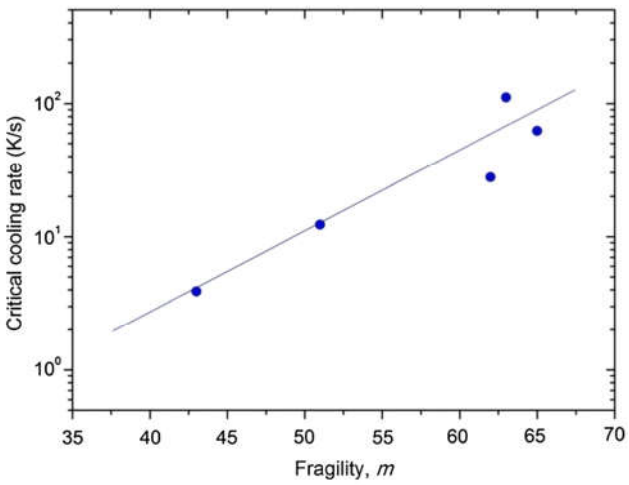

Figure 8. Relationship between critical cooling rate and fragility of five amorphous steel formers [134].

It is worth mentioning that correlation between free volume, viscosity and GFA has been studied [135, 136]. They concluded that a smaller density of free volume would suppress the movement of atoms and lead to a higher viscosity and GFA [135, 136]. In some of amorphous

steels that have a relatively large driving force for crystallization, there is still room for improving the GFA [129]. Johnson *et al,* [134] has classified bulk glass formers into two groups namely thermodynamically stabilized and kinetically stabilized glasses. The former term refers to glasses whose formation is mainly controlled by thermodynamic suppression of stable crystalline phases and are accommodated by a small driving force for devitrification. This type of systems generally shows an incremental trend in GFA with decreasing the Gibbs free energy difference between the supercooled liquid and the crystalline solid. Kinetically stabilized bulk metallic glasses include glasses whose formation is governed by the kinetic suppression of competing crystalline phases. The GFA of these alloys could not be evaluated only based on thermodynamics of crystallization. However, other factors, especially those affecting the kinetics of glass formation such as electronic structures must be taken into consideration [134].

1.8.4. Effect of alloying elements on GFA

1.8.4.1. Addition of elements with a negative enthalpy of mixing

One of the most effective approaches for improving the GFA of glass formers is to wisely choose alloying elements in such a way that chemical interactions and atomic size differences among the constituent elements help to enhance GFA [4, 137]. Basically, alloying elements could be classified into two categories: (i) elements with a negative enthalpy of mixing, and (ii) elements with a positive enthalpy of mixing. When elements from group (i) are added, their effect on glass forming heavily depends on their atomic sizes. Figure 9 shows the atomic radii of feasible elements to be alloyed in bulk metallic glass formers which could be divided into three groups [138]. These

groups include small atoms, intermediate atoms and large atoms. In the next section, the effect of alloying elements based on their size would be discussed and analyzed.

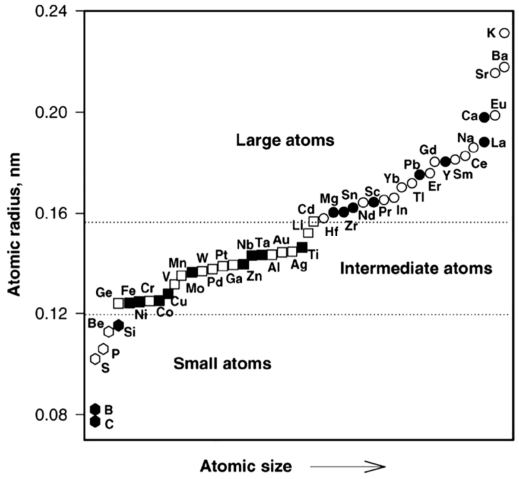

Figure 9. Atomic radius of alloying elements for glass formers [138].

1.8.4.1.1. Addition of small atoms

Small atoms include C, Si, B, P, S, and Be. Effect of adding Be and S on the GFA of amorphous steels has not been deeply studied yet. On the other hand, the role of C, Si, B, and P, due to their important contribution to GFA, has been extensively studied. Except for handful numbers of Fe-based BMGs [139], one or more metalloid elements from C, Si, B, and P must be added to attain the high GFA for Fe-based BMGs [140]. The tangible effects of metalloid elements on GFA, thermal stability and crystallization of Fe-based bulk metallic glasses could be understood thermodynamically and kinetically. Thermodynamically, in order to impede the crystallization, two factors should be considered. Driving force for glass formation ($-\Delta H^{amor}$) and resistance against crystallization ($\Delta H^{amor} - \Delta H^{inter}$) which is the difference between the driving force for the

glass and that of intermetallic compounds [141, 142]. Wu *et al* [141], reported that for alloys with chemical composition of (Fe, Cr)-metalloid (metalloid=C or B or P), carbon has the highest impact on increasing the GFA. Figure 10 shows the correlation between ($-\Delta H^{amor}$) and ($\Delta H^{amor} - \Delta H^{inter}$) with concentrations of metalloids in Fe-metalloid alloy systems. It is clearly seen that Fe-C system has the largest driving force for glass formation and the highest resistance against the crystallization from which the significant role of carbon in improving the GFA could be understood. Kinetically, P, compared with C and B, has a larger solubility in iron alloys. Therefore, when α-Fe precipitates, more of C and B need to diffuse compared to P. Consequently, C and B are more effective in retarding α-Fe precipitation and enhancement of GFA [141].

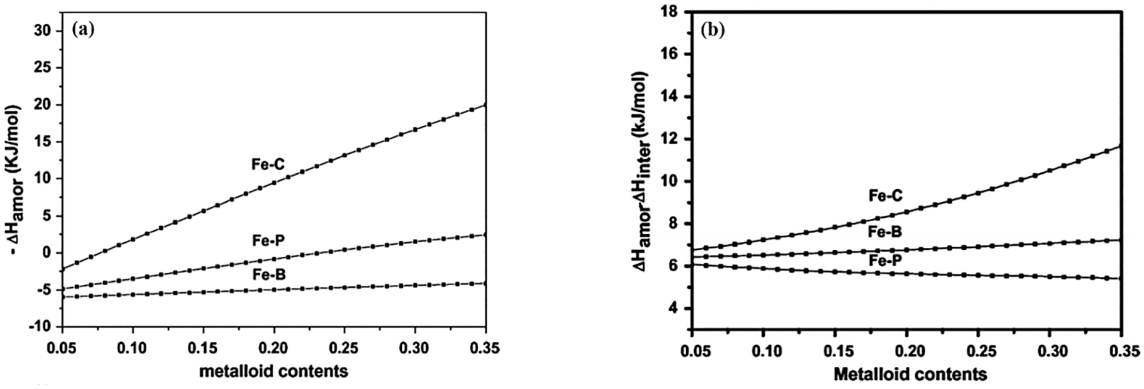

Figure 10. Correlation between (a) ($-\Delta H^{amor}$) and (b) ($\Delta H^{amor} - \Delta H^{inter}$) with concentrations of metalloids in Fe-metalloid alloy systems [141].

According to the literature, GFA of iron-based alloys strongly depends on the concentration of metalloid elements such as C, B, Si, and P. However, the optimized concentration of each of them is different. According to binary phase diagram of each of these elements with Fe, the eutectic point at Fe-C, Fe-B, and Fe-P systems is near 17 at%. For Fe-Si system, the eutectic point is observed beyond 30 at%. Generally, the total concentration of metalloid additions in Fe-based bulk metallic glasses sits in the range of 17 at% to 25 at% [141].

1.8.4.1.2. Addition of intermediate atoms

Elements with intermediate atomic sizes include mainly transition group metals. These typical transition group elements consist of Co [127], Ni [143], Cr [143], Mo [144], Nb [145], Al [129], Ga [146], Mn [147], W [148], Ti [149], Ta [150], V [151], and Pt [152]. In order to elaborate the effects of these elements on the change of GFA, Jiao *et al*, [153] selected a pseudo-binary Fe-(Si, P, C, B) alloy, with a maximum diameter of 1 mm for glass formation, as a master alloy and studied the role of adding individual transitional metals including Al, Ti, V, Cr, Mn, Co, Ni, Ga, Nb, Mo, and Ta on the GFA of the alloys. Figure 11 depicts the correlation between the critical diameter for glass formation and the concentration of alloying elements for different transition metals. It is seen that the alloy with 3 at% of Mo shows the highest GFA (5 mm) followed by 1 at% Ga (3 mm), 0.3 at% Cu (3 mm), 5.0 at% Ni (3 mm), 7.0 at% Co (3 mm), 1.0 at% Cr (2 mm), and 1.0 at% Al (2 mm). Also, they reported that alloys with a higher GFA are those whose chemical compositions are closer to eutectic.

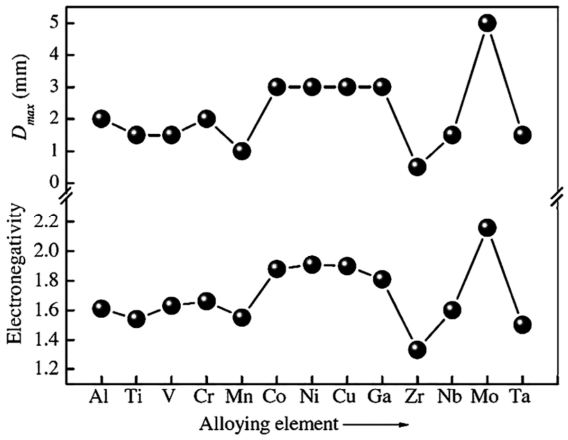

Figure 11. The critical diameter values as a function of concentration of alloying elements in Fe-(Si, P, C, B) master alloy [153].

Correlation between the critical diameter for glass formation and electronegativity for alloying elements in Fe-(Si, P, C, B) master alloy is shown in Figure 12. Variation of GFA is in a good agreement with that of electronegativity of alloying elements meaning that the larger the electronegativity of alloyed element is, the higher the GFA and the larger the critical diameter. Furthermore, the larger absolute value of the electronegativity difference between Fe and alloyed element will result in a lower optimum concentration of alloying element. This means that a higher amount of alloying elements with a similar electronegativity as Fe (Co, Ni) has to be added to the master alloy in order to attain a higher GFA [153]. The reason for such observation is that those elements whose electronegativity is slightly smaller or larger than that of Fe, have a very strong tendency to form solid solutions. Hence, even a very small quantity of these elements can strongly affect the GFA. On the other hand, elements whose electronegativity stand far away from that of Fe, can destabilize the glassy liquid phase, if they are added in a high concentration. As a result, new competing crystalline phases would form during cooling. Also, the appropriate addition of elements with electronegativity values larger than that of Fe, can create a denser atomic structure in the supercooled liquid and increase the atomic packing density which leads to the stabilization of supercooled liquid. On the contrary, the addition of elements with electronegativity values smaller than that of iron destabilizes the liquid phase due to formation of weak bonding atomic pairs. So, the optimum concentration of these elements are smaller [88].

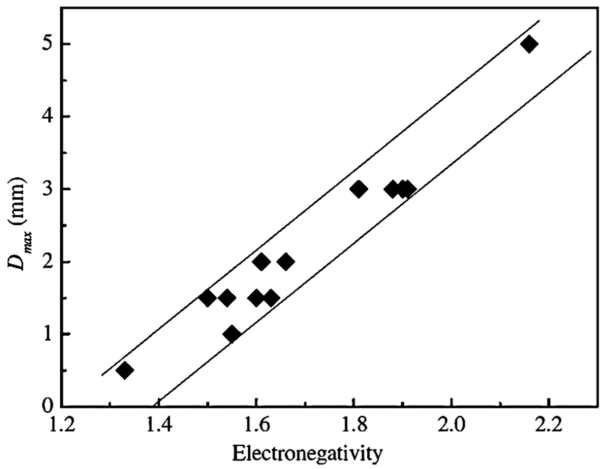

Figure 12. Correlation between the critical diameter for glass formation and electronegativity for alloying elements in Fe-(Si, P, C, B) master alloy [153].

1.8.4.1.3. Addition of large atoms

This type of atoms includes mainly Zr, Hf, Y, Nd, Er, Gd, Sm, and Tm. Addition of such large atoms has two consequences. First, they would expand the atomic size distribution in the alloy and second, they usually have a large negative mixing enthalpy with Fe and/or metalloid elements. These two consequences, combined, increase the topological and chemical short-range order which will end up with the formation of a dense atomic structure and stabilization of supercooled liquid owing to the difficulty in the long-range rearrangement of the constituent elements against crystallization. Addition of large RE elements like Y and Er, destabilizes the competing $Fe_{23}M_6$ crystalline phase and shift the alloy composition closer to the eutectic point [100, 101]. Also, RE elements have a strong affinity for oxygen, so their addition to the master alloy can hunt the oxygen and suppress the heterogeneous nucleation and consequently improve the GFA [101]. The optimized atomic size distribution and the larger negative mixing enthalpy between RE elements and other elements such as metalloids can facilitate the formation of dense packing structure, stabilize the supercooled liquid, and postpone the devitrification process [88].

1.8.4.2. Addition of elements with a positive enthalpy of mixing

There are important elements whose mixing enthalpy with iron is positive. Some of these elements include Cu, Sn, Zn, Ag, In, La, and Yb [154]. According to the literature, there are a few papers that report the effects of adding Sn and Yb on the GFA of Fe-based bulk metallic glasses [155, 156]. However, there is a good amount of information about the effect of copper on the GFA of amorphous steels. Positive mixing enthalpy of copper with iron, facilitates the formation of Cu-enriched clusters which gradually develop and transform into an FCC lattice during annealing process. That is why the primary α-Fe would nucleate at Cu/amorphous interface and refine the α-Fe grains. Improved soft magnetic properties is one of the advantages of grain refinement in α-Fe phase [157-160]. High-resolution transmission electron microscopy (HRTEM) images and corresponding SAED patterns of as-cast ribbons and rods of $Fe_{76}C_{7.0}Si_{3.3}B_{5.0}P_{8.7}Cu_x$ (x = 0, 0.3, 0.7) alloys are shown in Figure 13 [161]. By adding 0.3 at%Cu, the GFA of alloy improves significantly (Figure 13 a, b). however, when no copper has been added or higher concentrations of Cu have been used, the GFA decreases and α-Fe nano crystals start to precipitate within the amorphous matrix (Figure 13 a, d, c, f).

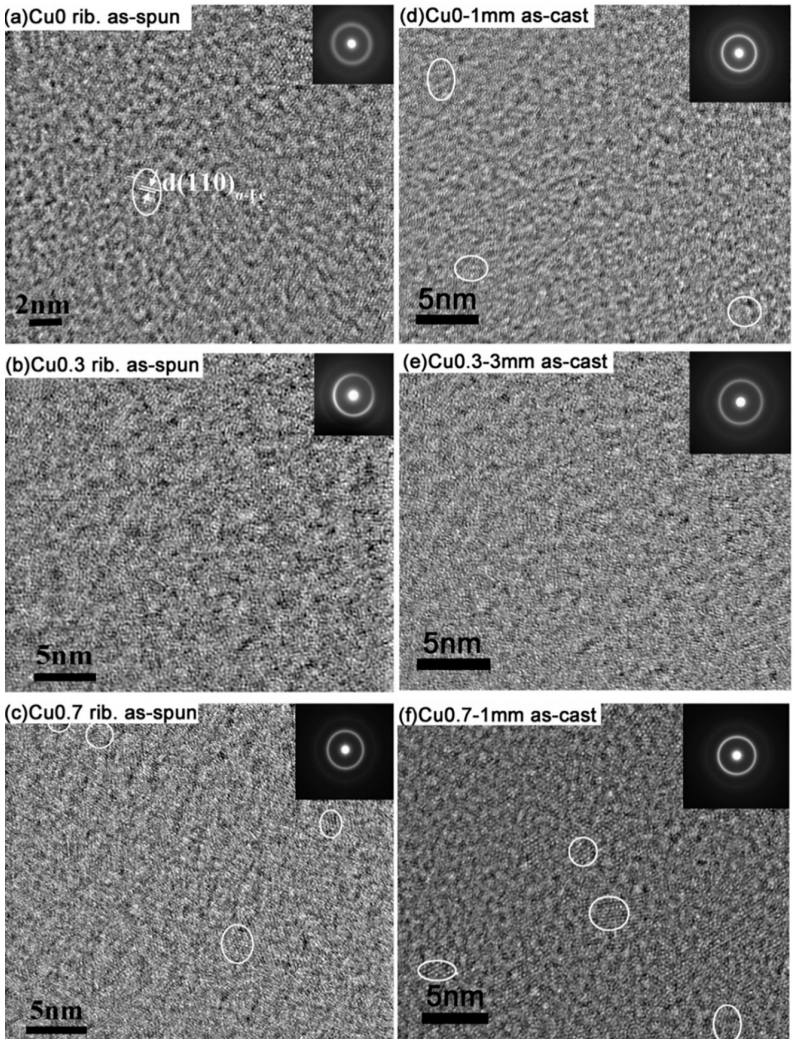

Figure 13. HRTEM images and corresponding SAED patterns of the as-cast ribbons and rods of the investigated $Fe_{76}C_{7.0}Si_{3.3}B_{5.0}P_{8.7}Cu_x$ alloys: (a) $Cu_{0.0}$, as-spun ribbon; (b) $Cu_{0.3}$, as-spun ribbon; (c) $Cu_{0.7}$, as-spun ribbon; (d) $Cu_{0.0}$, as-cast rod; (e) $Cu_{0.3}$, as-cast rod; (f) $Cu_{0.7}$ as-cast rod [161].

Atom probe tomography (APT) was also incorporated to confirm the effect of Cu concentration on the GFA (Figure 14) [161]. This image shows the APT result of $Cu_{0.3}$ and $Cu_{0.7}$ alloys annealed at 729K for 30 min. For annealed $Cu_{0.3}$ alloys, only amorphous phase without any trace of nano crystals are observed (Figure 14a) and all the elements are uniformly distributed within the amorphous phase without any sign of elemental segregation (Figure 14b). When the concentration of copper increases ($Cu_{0.7}$), a large quantity of ultrafine spherical nuclei for

devitrification (Figure 14c) as well as many tiny regions smaller than 2nm(Figure 14d) would form [161]. The constructive role of Cu on enhancement of GFA could be interpreted as following. Since Fe is the main component of the master alloy, there is a large tendency for the segregation of iron atoms and formation of clusters during the supercooling. When 0.3 at% cu is added to the master alloy, the redistribution of copper atoms impedes the formation of α-Fe which results in a higher GFA. Also, crystallization process of Cu-included alloy is diffusion controlled three-dimensional growth which requires the long-range diffusion of copper atoms to form α-Fe nano crystals. Therefore, the resistance against the crystallization increases owing to the high activation energy barrier which finally leads to the improvement of GFA [88].

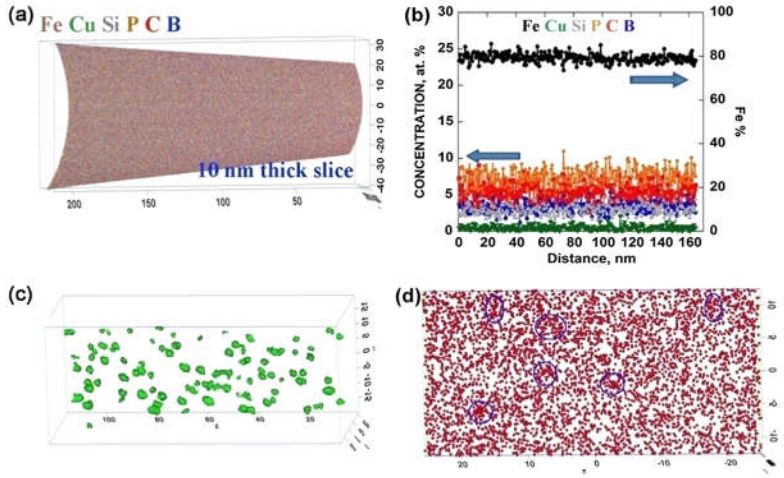

Figure 14. Results of APT analysis of $Cu_{0.3}$ and $Cu_{0.7}$ alloys annealed at 729 K for 30 min: (a) a 10-nm-thick atom map of the annealed $Cu_{0.3}$ alloy; (b) the corresponding elemental concentration profile along the length direction; (c) the 10% Cu iso-concentration surface of the annealed $Cu_{0.7}$ alloy and totally 102 Cu-rich precipitates; (d) the corresponding atom map of the C distribution. The circles in (d) indicate the locations where the C atoms are concentrated [161].

1.9. Crystallization of amorphous steels

Considering a supercooled liquid, if the liquid phase stability and its crystallization resistance are high, the GFA of alloy would be high. In order to understand the GFA of amorphous

steels, it is important to explore the crystallization characteristics and phase competition mechanism between the amorphous and crystalline phases. Table 1represents the chemical composition, critical thickness, crystallization mode and primary devitrified product for some typical iron-based bulk metallic glasses [102].

Table 1. Alloy composition, maximum diameter for glass formation, crystallization mode and the primary crystallization phase for some typical Fe-based BMGs [102].

Chemical composition	D_c (mm)	Crystallization mode	First crystallized phase
Fe-(C, B)-(P, Si)	1-3	Single stage	α-Fe
Fe-(C, B)-(P, Si)-(Cr, Mo)	5	Single stage	$(Fe, Mo)_{23}(B, C)_6$
(Fe, Co)-B-Si-Nb	5.5	Single stage	$(Fe, Co)_{23}(B, Nb)_6$
(Fe, Co)-(C, B)-(P, Si)-Mo	5	Single stage	$(Fe, Co, Mo)_{23}(B, C)_6$
Fe-B-Mo-Y	6.5	Multi-stage	$(Fe, Mo)_{23}B_6$
(Fe, Co)-B-(Nb, Hf)-Y	7	Multi-stage	$(Fe, Co, Nb)_{23}B_6$
Fe-(C, B)-(Cr, Mo)-Tm	12	Multi-stage	χ-FeCrMo
Co-(C, B)-(Cr, M)-Tm	10	Multi-stage	χ-FeCrMo
(Fe, Co)-(C, B)-(Cr, Mo)-Tm	18	Multi-stage	χ-FeCrMo

Depending on the chemical composition of alloy, the crystallization process could be either single- or multi- stage. The first product of devitrification process in Fe-based bulk metallic glasses could be α-Fe or $Cr_{23}C_6$-type phase or χ-FeCrMo phase. It has been found that in Fe-based BMGs with a high GFA, the first crystallized phase is either $Cr_{23}C_6$-type phase or χ-FeCrMo phase [100, 101, 162]. It has been shown at during crystallization of Fe84Nb7B9 amorphous alloy, BCC-like MRO regions grow and coalescence into BCC-Fe nano crystals [163]. BCC-structured atomic clusters are easily formed within the range of 1–2 nm without any long-range diffusion. The reason is that the corresponding unit cell has only two atoms which makes it very small (a = 0.286 nm).

On the other hand, the $Fe_{23}B_6$-type structure is very complex with a large unit cell (a = 1.073 nm) which includes 92 metallic and 24 metalloid atoms, and its formation demands long-range atomic diffusion. Due to the approximation between the quasicrystal-like structure and $Fe_{23}B_6$ structure, it would be similarly difficult to form this kind of complex quasicrystal-like structure. Therefore, the atomic ordering process becomes more complex and difficult, compared to that of the bcc-type structure. Hence, the crystallization process of the alloys with the $Fe_{23}B_6$-type primary phase is kinetically suppressed compared to the alloy with the BCC Fe-type primary phase, leading to its stronger crystallization resistance and thus higher GFA [88, 163].

1.10. Fabrication of amorphous steels

At the beginning of amorphous steels development, due to their low GFA, Fe-based bulk metallic glasses were usually in the form of ribbons which were produced via single-roller melt spinner or splat quenching methodologies to guarantee a very fast quenching rate of 10^5-10^6 K/s. However, with discovery of new multi-component Fe-based alloys with a remarkably higher GFA, other techniques such as injection-casting ad suction-casting of a melt into copper molds became available for the fabrication of amorphous steels [91, 102, 117, 164-166]. Furthermore, manufacturing of RE-containing Fe-based bulk metallic glasses with a critical size of higher than 1cm became feasible using drop-casting technique [101, 127]. Recently, many more methods such as centrifugal casting [167, 168], mechanical alloying [169, 170], consolidation of amorphous powder through clod pressing, hot pressing or pulse current sintering [171-173], spark plasma sintering [174, 175], and pressure die casting [176] have been extensively used for the fabrication of Fe-based BMGs.

Gan *et al,* [177] combined the flux melting and copper mold casting techniques and invented a novel copper mold casting set up (Figure 15) which provides large supercooling as well as a fast quenching rate. They successfully produced $(Fe_{40}Ni_{40}P_{14}B_6)_xGa_{100-x}$ BMGs with a diameter of 3 mm from industrial raw materials.

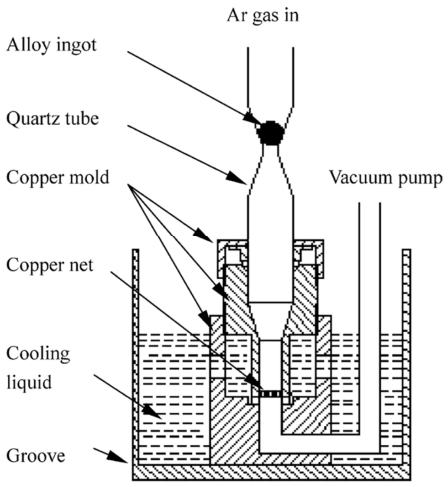

Figure 15. A schematic presentation of novel copper mold casting set up introduced by Gan et al, [177]

J-quenching is another appealing technique which was specifically invented for the fabrication of Fe-based BMGs [178]. As shown in Figure 16, this system has a J-shaped silica tube of which the upper portion has a length of 5-10 cm and an inner diameter of 10-13 mm. the lower part of this set up is significantly thinner meaning that it is 5-10 cm long with a wall thickness of 0.1-0.3 mm. The master alloy would be loaded at the bottom of the upper tube. The J tube would be pumped down using a mechanical pump, and then high-purity argon gas would be blown into the system to ensure a certain vacuum. The ingot is then melted by a torch and pushed into the smaller fused tube by the argon gas. In the next step, the whole J system is transferred to a furnace which includes a heating coil as shown in Figure 16. The ingot in the smaller tube will be heated

above its liquidus temperature and held there for a period to stabilize at that temperature. Finally, the tube with the sample will be removed from the furnace and quenched in salted ice-water. By implementing these steps, amorphous rods with the inner diameter of the smaller tube can be successfully fabricated [178].

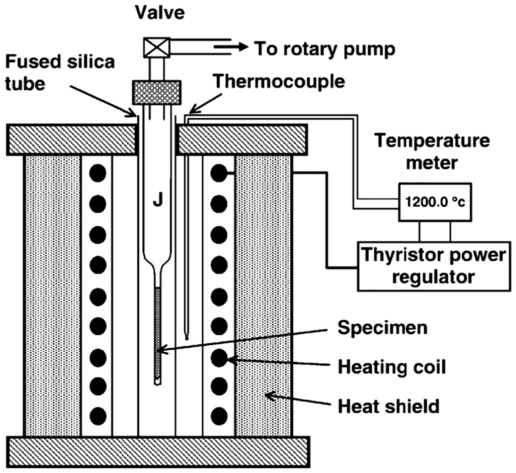

Figure 16. A schematic presentation of J-quenching set up [178].

Interestingly, J-quenching method has two important merits compared to other manufacturing methods of amorphous steels. Besides enhanced GFA, the specimens prepared by J-quenching show significantly improved compressive plasticity [88]. Figure 17, compares the compressive response of an amorphous steels produced via two different methods of conventional copper mold casting and J-quenching. The alloy which was produced by conventional copper mold casting method shows almost zero plasticity, however for the specimens fabricated using J-quenching technique, 6% of compressive plasticity was observed. Additionally, significantly more shear bands were observed on the fracture surface of J-quenching samples. The reason for such an observation is that J-quenching technique provides a larger cooling-rate gradient from the sample

surface to the interior which is due to the low heat capacity of silica. Larger cooling-rate gradient leads to the non-uniform concentration of free volume from the surface to the middle of cast parts. A higher concentration of free volume on the outer surface of cast samples can trigger the nucleation of shear bands under compressive loading which enhances the plasticity [88].

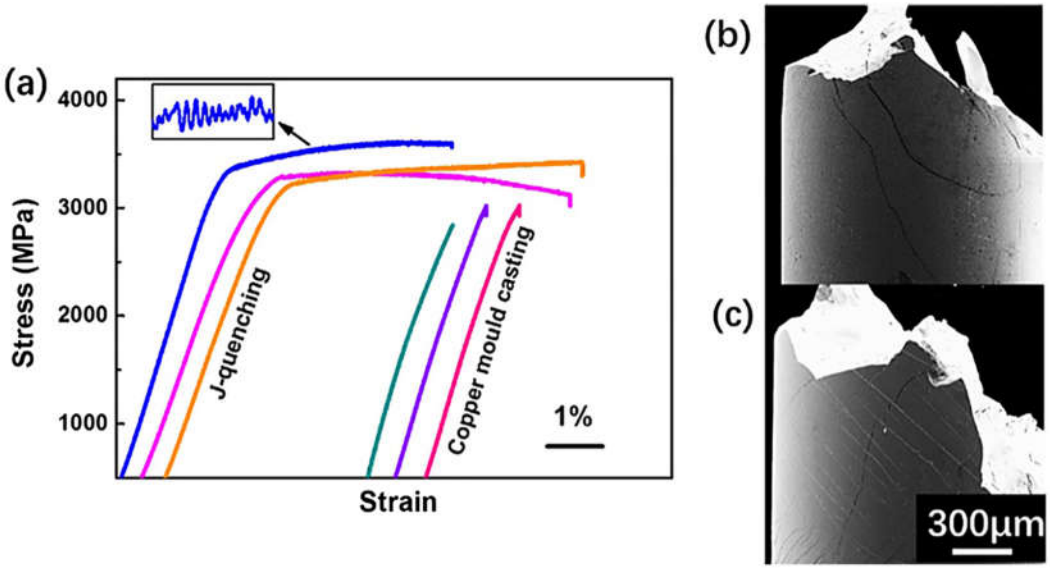

Figure 17. (a) Compressive stress-strain curves for an amorphous steel produced by J-quenching and copper mold casting methodologies, (b) fracture surface of a specimen produced by suction casting and (c) J-casting [88].

Recently, additive manufacturing or 3D printing technology has been vastly used for the fabrication of Fe-based bulk metallic glasses and their composites [179-184]. The first attempt was made by Pauly *et al*, [180] in 2013 during which $Fe_{74}Mo_4P_{10}C_{7.5}B_{2.5}Si_2$ BMG was manufactured by selective laser melting (SLM). In this process, amorphous powder was melted by laser irradiation and then built up layer by layer into a 3D BMG part [180]. The main drawback was that the printed specimens were partially crystallized, and many process-induced cracks formed due to the large thermal stress during the manufacturing process. Following this attempt, Jung *et al*, [181] in 2015, reported that by decreasing the scan speed to <2500 mm/s and increasing the

laser power to >300W in SLM method, BMG samples with a chemical composition of $Fe_{68.3}C_{6.9}Si_{2.5}B_{6.7}Cr_{2.3}Mo_{2.5}Al_{2.1}$, and a relative density higher than 99% could be manufactured. The printed parts turned out to be fully amorphous and their crystallization behavior and intrinsic magnetic properties (T_c and M_s) are identical to those of their parent gas-atomized powders. However, there is a small difference in the initial part of M-H hysteresis loop [181]. Nevertheless, the existence of micro pores and fine cracking are the crucial limitations od SLM techniques which need to be addressed. According to the literature, employing post treatments such as online annealing, re-scanning using a ow energy density, pre-laid powders, thermal spray 3D printing, and manufacturing BMG composites by introducing a second phase with high toughness have all been proposed to attenuate crack, voids and/or high residual stresses [181-184]. However, producing a crack-free, dense, and fully amorphous Fe-based bulk metallic glass implementing 3D printing approach has remained a big challenge due to the complexity and inherent limitations of 3D printing.

1.11. Mechanical properties of Fe-based bulk metallic glasses and their composites

1.11.1. Compression

It is clearly known that due to the lack of crystalline microstructural defects such as dislocations, grain boundaries, and crystalline secondary phases, amorphous alloys possess high strength, hardness, high elastic strain, low Young's modulus and super plasticity in supercooled region [88]. Figure 18 compares the Vicker's micro hardness, Young's modulus and tensile strength of typical amorphous alloys and conventional crystalline materials [122]. Interestingly, amorphous alloys exhibit significantly higher strength and hardness compared to those of

crystalline counterparts, however they suffer from a relatively lower Young's modulus. Bulk metallic glasses are classified base on their chemical composition. Among different types of BMGs, Fe-based bulk metallic glasses or amorphous steels have higher strength and hardness value. Though their Young's modulus is very close to that of conventional steels, the strength and hardness of amorphous steels are 3-4 times higher than those of super high-strength steels [122]. For instance, most of amorphous steels show a compressive strength higher than 3GPa. So far, $(Fe_{0.335}Co_{0.335}Nb_{0.06}B_{0.27})_{99.8}Cu_{0.2}$ BMG has shown a compressive strength of 4.93 GPa which is the highest value reported for bulk metallic glasses [185].

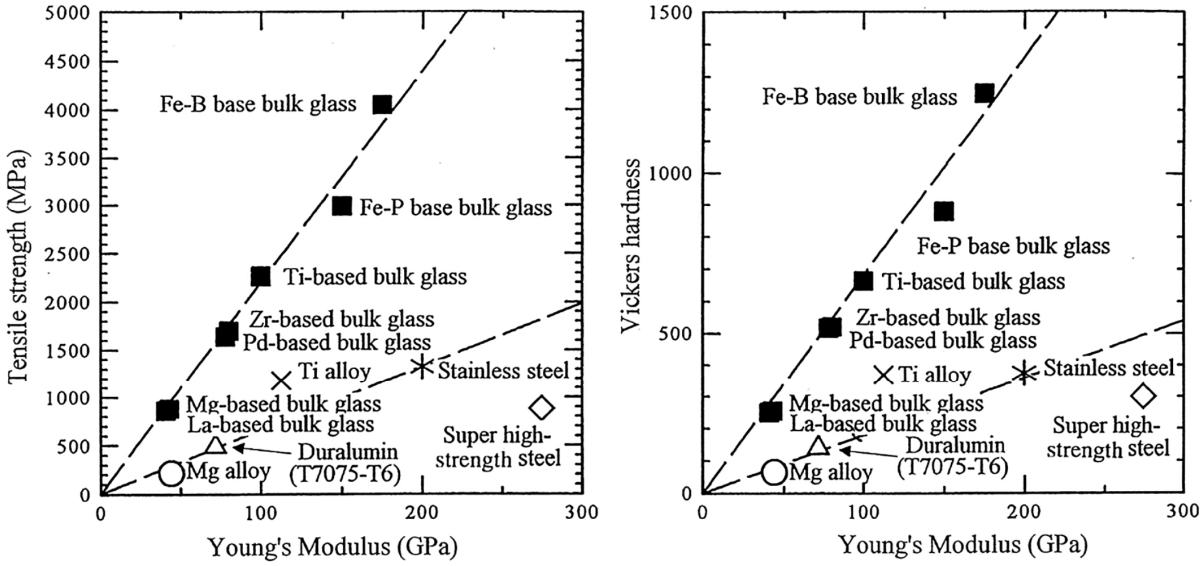

Figure 18. Comparison between Vicker's micro hardness, Young's modulus and tensile strength of typical amorphous alloys and conventional crystalline materials [122].

Recently, enhancement of room temperature plasticity of amorphous steel has received a great deal of attention since lack of this crucial property has limited the application of Fe-based bulk metallic glasses as structural materials significantly. Generally, there are five different approaches through which the plasticity of amorphous steels could be improved.

(i) Designing Fe-based BMGs by aiming the high Poisson's ratio and/or low shear modulus [114, 186-188],

(ii) Designing amorphous steels with a high room-temperature plasticity via manipulating the atomic bonding [114, 189, 190],

(iii) Inclusion of structural heterogeneities through phase separation and/or short/medium range order clusters [113, 191-193],

(iv) Geometric confinement by decreasing the aspect ratio of the samples, applying lateral confining sleeves, and use of electroplating coatings [194-196], and

(v) Developing a composite microstructure within the amorphous matrix by precipitating ductile crystalline phases or nano crystals [112, 197-200].

Brittleness of crystalline metals is associated with the ratio of shear modulus (G) to the bulk modulus (K) or equivalently, the Poisson's ratio (υ=G/K) [201]. When G/K ratio, in a crystalline metal, goes beyond a critical value, the metal become brittle. When it comes to metallic glasses, Chen *et al*, [202] in the 1975 reported that increase in Poisson's ratio will lead to the enhancement of ductility. After that in 2005, Lewandowski *et al*, [201] found a similar relationship between Poisson's ratio and compressive plasticity in bulk metallic glasses. The G/K ratio of ductile BMGs has been found to be < 0.41–0.43 corresponding to a Poisson's ratio > 0.31–0.32. In an agreement with this statement, Gu *et al*. [187] reported that a transition from brittle to plastic deformation for Fe-based BMGs takes place as the Poisson's ratio exceeds the critical value of 0.32. Having this knowledge about the effect of Poisson's ratio on the ductility of amorphous steels has set a pathway to choose and add alloying elements whose Poisson's ratios are high and show a significant compressive plasticity. For instance, addition of Ni, which has a high Poisson's ratio,

to FeMoPCB metallic glasses, it compressive plasticity increased up to 8.5% [188]. Guo *et al*, [203] studied FeC(B)-, FeB- and FeP(C)-based bulk metallic glasses and came up with a composition-ductility map which is shown in Figure 19.

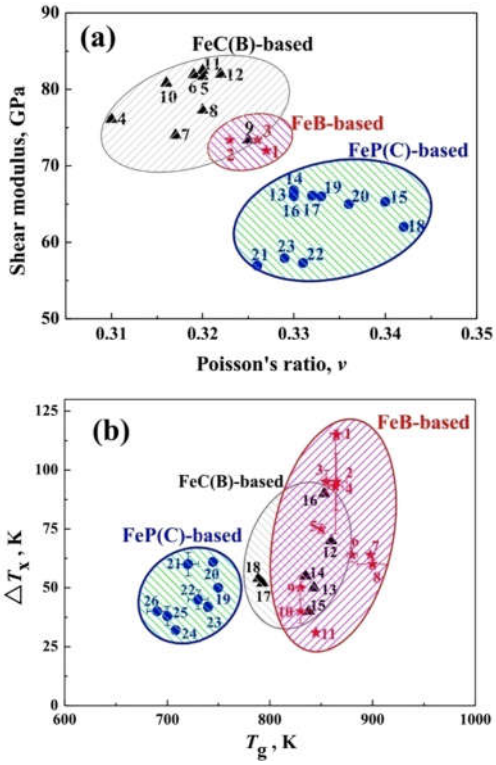

Figure 19. Relationship between (a) shear modulus and Poisson's ratio, and (b) ΔT_x and T_g for FeB-, FeC(B)-, FeP(C)-based BMGs [203].

They observed that FeB-, FeC(B)-based BMGs show brittle behavior, while FeP(C) exhibits ductile deformation response which has a higher Poisson's ratio, a lower shear modulus and a lower glass transition temperature. Additionally, $Fe_{62}Ni_{18}P_{13}C_7$ BMG could be plastically deformed more than 50% at room temperature which is the largest value reported so far for amorphous steels [203].

Manipulating the atomic bonding in amorphous steels is another effect approach to increase their room-temperature plasticity. The structure of amorphous steels at atomic level could be

considered as a space-filling network of polyhedral. Metalloid atoms occupy the centers of atomic clusters which are either connected by intercluster metal-metal bonds or by sharing the metal atoms to form edge-sharing or face-sharing cluster pairs. So, it is obvious that mechanical characteristics of amorphous steels are strongly influenced by the interplay of the intracluster metal-metalloid bonds and intercluster metal-metal bonds in an amorphous network. Enhancement of the compressive plasticity which takes place through the mitigating the shear bands formation, could be triggered by weakening the strong covalent bonds (metal-metalloid bonds) and strengthening the metal-metal bonds in an amorphous structure. This goal could be fulfilled by choosing appropriate combination of metal and metalloid elements [114, 189, 190]. For instance, addition of 30 at% of Ni to $Fe_{80}P_{13}C_7$, increases the compressive plasticity to beyond 20% which is remarkably higher that of corresponding Bi-free BMGs (<5%) [190].

The plastic deformation of bulk metallic glasses is governed by the number of shear bands that form under straining. Alloys whose atomic packing is lees denser, can generate more shear bands. The reason is that the energy barrier in front of atomic rearrangement related to the formation of multiple shear bands is smaller. Also, in bulk metallic glasses whose structure has a loose atomic packing, there is a larger concentration of free volume in comparison to alloys with denser atomic packing. A higher density of free volume can facilitate the formation of multiple shear bands and promotes the plastic deformation [1]. Different methodologies have been introduced for the synthesizing BMGs with a loose atomic packing among which those based on phase separation are the most effective ones. Atomic-scale separation will lead to the formation of soft and hard regions with different chemical compositions and packing densities. These soft and hard regions create inhomogeneous distribution of modulus and critical shear stresses in the BMG microstructure. Under loading, shear bands start to form from the soft regions that have a higher

density of free volume and a lower critical shear stress. Theses shear bands can also form at the interface between soft and hard regions. When shear bands propagate and reach to a hard region with a higher critical shear stress, its propagation will be impeded which results in changing the propagation direction of shear band and helps the multiplication of shear bands and enhancement of compressive plasticity [88]. Phase separation in amorphous alloys could be induced by adding elements that have a large difference in mixing enthalpy with the major elements of the alloy, or doping with an element with a positive enthalpy of mixing with the major elements of the alloy [111, 191]. Multiple amorphous steels with enhanced plasticity have been successfully produced using the phase separation methodology [113, 191, 193]. Engineering compressive stress-strain curves for $Fe_{52}Co_{(20-x)}B_{20}Si_4Nb_4V_x$ alloys as well as EDS line analysis of Fe, Co, and V elements from the HR-TEM analysis for $Fe_{52}Co_{20}B_{20}Si_4Nb_4$ and $Fe_{52}Co_{17.5}B_{20}Si_4Nb_4V_{2.5}$ alloys are shown in Figure 20 [191].

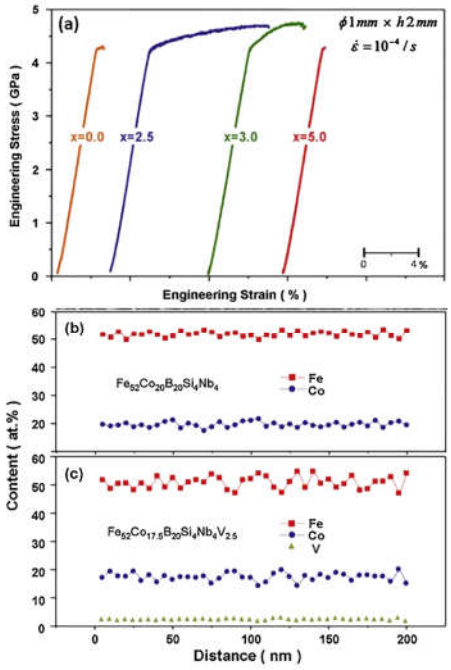

Figure 20. (a) Engineering stress-strain curves of $Fe_{52}Co_{(20-x)}B_{20}Si_4Nb_4V_x$ alloys and EDS line profiles of Fe, Co and V elements from HRTEM analysis for (b) $Fe_{52}Co_{20}B_{20}Si_4Nb_4$, and (c) $Fe_{52}Co_{17.5}B_{20}Si_4Nb_4V_{2.5}$ BMGs [191].

Figure 20a shows that by addition of 2.5 at% of V, the plastic deformation of base alloy increases from almost zero to 6.3%. The EDS analysis (Figure 20B) shows that by adding 2.5 at% of V, the amplitudes of the compositional fluctuations of Fe, Co and V increases which confirms the occurrence of atomic-scale phase separation within the V-containing alloy (Fig. 40(b)).

It is worth mentioning to explore the mechanism through which soft and hard regions can improve the plasticity of amorphous steels. Sarac *et al,* [193] observed some heterogeneities in the $Fe_{50}Ni_{30}P_{13}C_7$ BMG via aberration corrected HR-TEM, as presented in Figure 21.

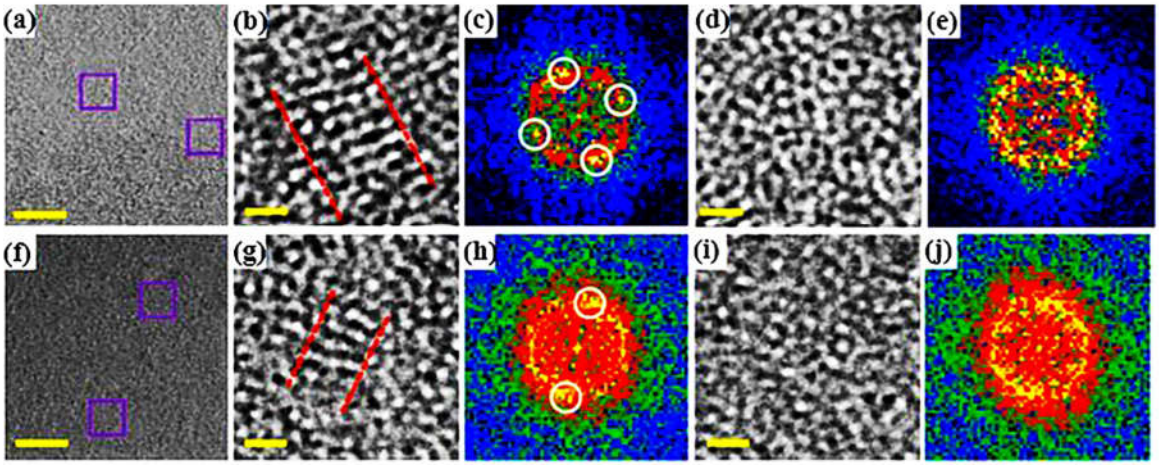

Figure 21. HR-TEM study of heterogeneities. (a), (f) 1A and 2A regions show nanocrystals in the amorphous matrix (1B and 2B). (b), (d), (g), (i) HR-TEM images and (c), (e), (h), (j) corresponding FFT patterns taken from two different regions of the specimen with 8-nm thickness. The spots encircled by white circles in the FFT patterns in (c) and (h) corroborate the presence of nanocrystals in the specimen, whereas no speckles are observed in the FFT patterns in (e) and (j) (scale bars, (a) and (f)-5 nm, (b), (d), (g), and (i)-0.5 nm) [193].

They found out that there is local atomic ordering in the soft regions (Figure 21 b and g) which are basically nano crystals with the size of 1-1.5 nm that are uniformly distributed through the whole specimen as proved by bright spots on the broad halo in the FFT patterns (Figure 21c and h). However, the hard region (matrix) shows the a maze-like amorphous pattern with a broad diffuse diffraction halo with no point maxima in the FFT diffraction pattern (Figure 21 e and j). It has been found that, upon loading, the deformation of nano crystals can initiate the formation of

shear transformation zones (STZs) with similar atomic volumes. Also, nano crystals can hinder the propagation of shear transformation zones [193]. Therefore, the absorbed energy can be dissipated through the regions with the nano crystals which are shown in gray color in Figure 22 . Since size of plastic zone (20μm) is significantly larger than the average space between the soft zones, formation of multiple shear bands takes place, shown by thin black lines in Figure 22. Multiplication of shear bands will lead to an enhanced plasticity of $Fe_{50}Ni_{30}P_{13}C_7$ BMG [193].

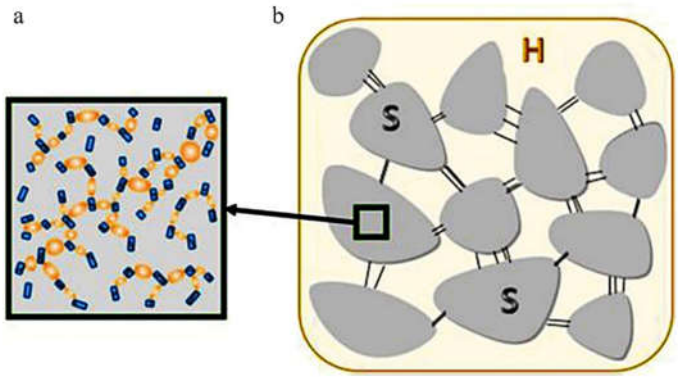

Figure 22. A Schematic illustration of multiscale deformation behavior in $Fe_{50}Ni_{30}P_{13}C_7$ BMG. (a) Nanocrystals (blue particles) have a lower shear modulus compared to the matrix and therefore deform first (small gray lines within NCs). Deformation proceeds by the formation of homogenously dispersed STZs between NCs. (b) On the micro-scale, shear bands do not develop into cracks because the distance between the soft regions is smaller than the critical crack length of the BMG [193].

Besides phase separation, introduction of short-/medium-range ordered clusters can also enhance the compressive plasticity of BMGs [185, 192, 204]. Copper is one of the promising candidates for inducing the clusters in the microstructure of amorphous steels. Zhao *et al*, [185] reported that by adding 0.1 at% of copper to chemical composition of $(Fe_{0.335}Co_{0.335}Nb_{0.06}B_{0.27})_{100-y}Cu_y$, the compressive plasticity increases from 1.4% to 3.7% with no change in the strength which was found to be due to the formation of 1-2nm scale MRO [185]. Beneficial effects of SRO/MRO on the compressive plasticity have been ascribed to two principle function of clusters. First of all, clusters can alter the distribution of free volume and facilitate the nucleating of multiple shear

bands through the bulk. Secondly, clusters can cause the branching of the shear bands which distributes the plastic strain on the shear bands and consequently suppresses the crack initiation which postpones the failure of specimen. However, it should be noticed that if the concentration of clusters exceeds the optimum value, it can deteriorate the plasticity [112].

Another effective approach to improve the compressive plasticity of amorphous steels is introducing a secondary ductile phase within the amorphous matrix. By doing that, propagation direction of shear bands would be deflected upon shear bands meet the ductile phase and will result in the shear band branching. Also, the shear bands are blocked or branched by other intersected shear bands. Formation of multiple branched shear bands can end up with a significant enhancement in the plasticity. Introduction of the secondary ductile phase or fabrication of Fe-based bulk metallic glass composites could be fulfilled via nano crystallization or introduction of crystalline phases and ductile dendritic phases into the amorphous matrix [112, 197-200, 205, 206]. Figure 23 represent the stress-strain curves of $(Fe_{0.76}Si_{0.096}B_{0.084}P_{0.06})_{100-x}Cu_x$ amorphous alloys with and without Cu content as well as corresponding HR-TEM images and SAED patterns [199]. It is evident that even by adding 0.1 at% of copper, the compressive plastic deformation shows a remarkable increase. HR-TEM images confirms the formation of a high density of α-Fe clusters with a diameter below 10nm in the amorphous matrix of the as-cast rods alloyed with 0.1 at% Cu. It is believed that under compressive loading, α-Fe clusters act as nucleation sites for the nano crystallization of α-Fe. This stress-induced nano crystallization has been introduced as the main reason for the recording a large plasticity in the Cu-containing alloy [199].

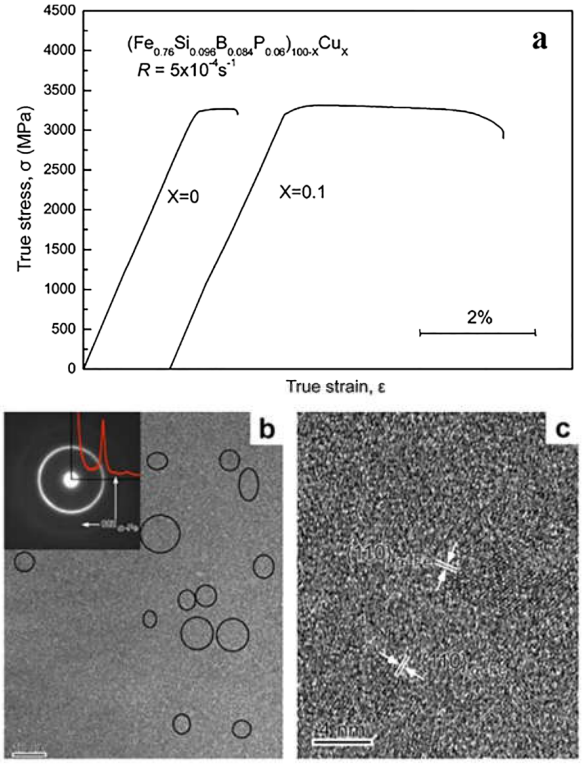

Figure 23. (a) Compressive deformation behavior of $(Fe_{0.76}Si_{0.096}B_{0.084}P_{0.06})_{100-x}Cu_x$ amorphous alloys with and without Cu content and (b, c) corresponding HR-TEM images [199].

Bulk metallic glass composites could be manufactured by adding ductile micro-crystalline phases into the amorphous matrix. Figure 24 shows the SEM images of an amorphous steel composite, XRD pattern and engineering stress-strain curve recorded under uniaxial compression [197]. $Fe_{77}Mo_5P_9C_{7.5}B_{1.5}$ alloy has a composite microstructure consisting of an amorphous matrix in which α-Fe dendrites are uniformly distributed. The maximum fracture strength and plastic strain of this composite are 3 GPA and >30%, respectively. The formation of ductile α-Fe dendrites was introduced as the main reason for the enhancement of plasticity in this alloy.

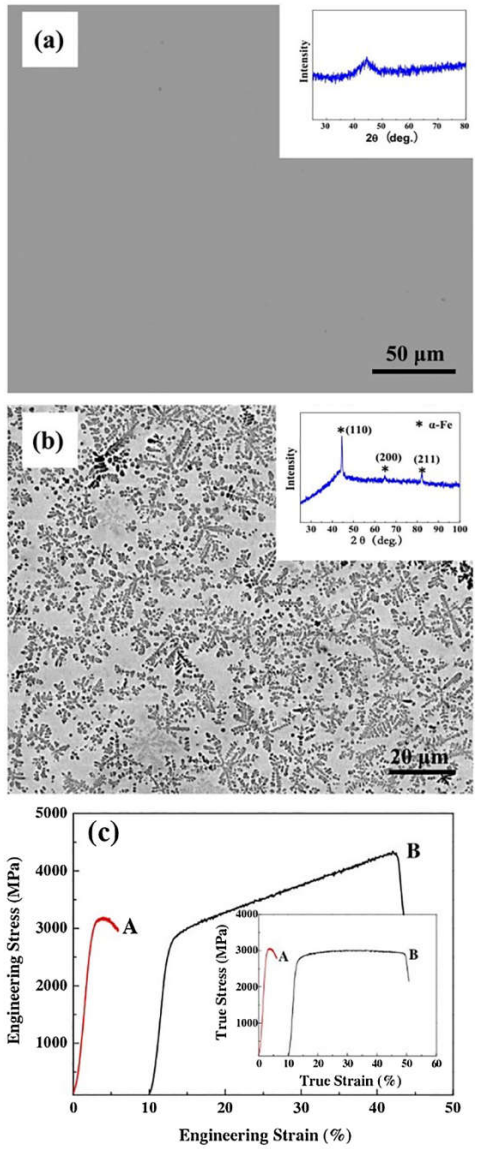

Figure 24. (a) SEM images of $Fe_{75}Mo_5P_{10}C_{8.3}B_{1.7}$ BMG, (b) *in situ* $Fe_{77}Mo_5P_9C_{7.5}B_{1.5}$ composites, and (c) the corresponding engineering stress-strain curves under uniaxial compression [197].

Geometrical confinement is another technique to increase the plasticity of bulk metallic glasses. This could be fulfilled by applying lateral sleeves, decreasing the aspect ratio of samples, and deposition of coatings by electroplating method. Engineering compressive stress-strain curves for $Fe_{62}Cr_{13}Mo_4P_{10}C_5B_6$ bulk metallic glasses with a diameter of 2mm and different aspect ratios (AR) from 0.19 to 2, are shown in Figure 25 [196]. It is seen that as the aspect ratio of testing samples decreases, different fracture modes including fragmentation (AR≥0.35), distensile

(0.35<AR<0.19), and constrained shearing (≤0.19) takes place. When the aspect ratio is small, the stress increases progressively with strain to a very high value even after yield point and constrained deformation happens until the sample is compressed into a thin disc. Also, the large friction between the platen and top surface of sample promotes the multiplication of shear bands which triggers the plastic deformation [196].

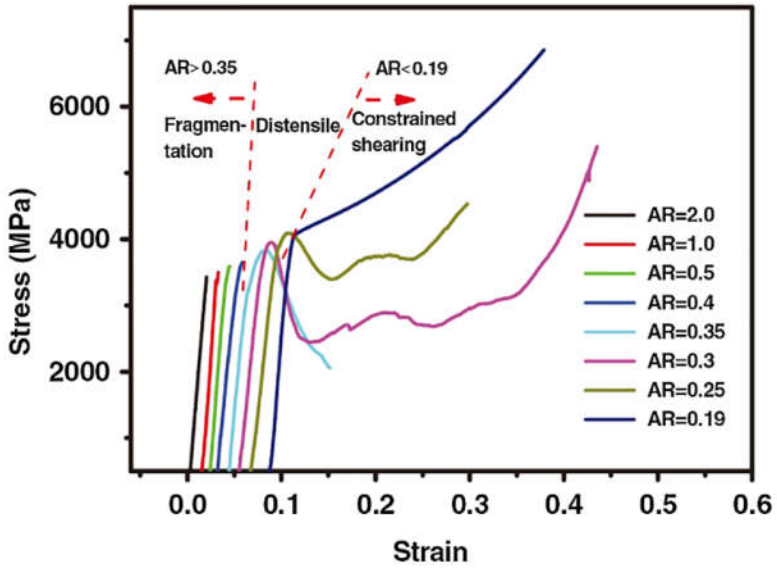

Figure 25. Engineering compressive stress-strain curves for $Fe_{62}Cr_{13}Mo_4P_{10}C_5B_6$ bulk metallic glasses with a diameter of 2mm and different aspect ratios [196].

Applying a lateral coating by electrodeposition method is another approach to enhance the plasticity of amorphous steels. Chen *et al* [194], applied an Ni coating with different thicknesses on $Fe_{75}Mo_5P_{10}C_{8.3}B_{1.7}$ BMG. Cross sectional images and corresponding stress-strain curves are shown in Figure 26. It is obvious that by increasing the thickness of Ni coating, the extent of plastic deformation increases too. It has been proposed that the Ni coating acts as barrier which impedes the propagation the shear bands under loading that finally leads to enhancement of compressive plasticity [194].

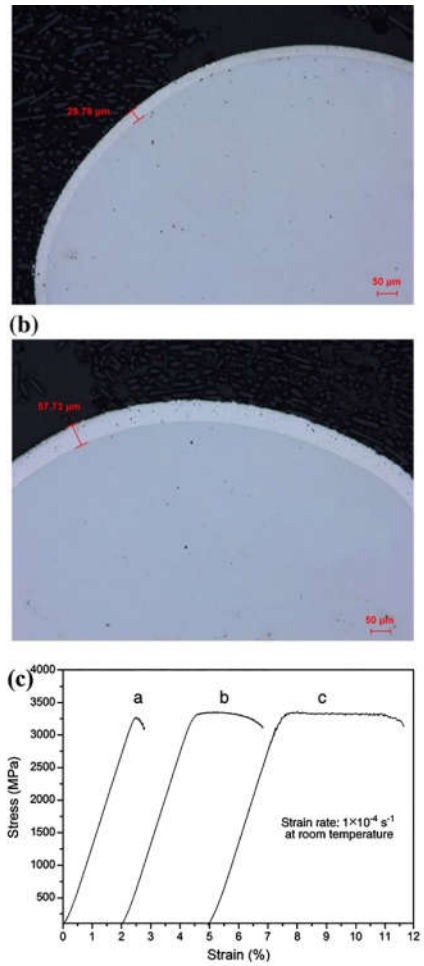

Figure 26. (a, b) Cross sectional images of the $Fe_{75}Mo_5P_{10}C_{8.3}B_{1.7}$ amorphous steel laterally coated by Ni with different thicknesses, and (c) corresponding compressive stress-strain curves. In image (c), curve (a) belongs to the sample without Ni coating, (b) Ni coating thickness of 29.79μm, and (c) Ni coating thickness of 57.73μm [194].

1.12. Quantification of crystallization process in amorphous systems

Amorphous materials including metals, alloys, ceramics, and polymers have received a great deal of attention due to their unique properties [207-211]. For example, amorphous silicon is widely used in fabrication of solar cells and thin film transistors. Amorphous chalcogenides are used as phase-change memory materials [212-214], biosensors [215-217], and infrared optical fibers [218-220]. For the case of amorphous metals, their high hardness, strength and wear

resistance, offers the promise of creating a new class of structural materials for applications in diverse areas, including shot peening balls and fine precise polishing media [221], as well as micro gears [222]. Also, high corrosion resistance combined with high strength and elastic modulus make bulk metallic glasses potential candidates for biomedical applications as sensors [223, 224], medical implants [225, 226], and self-expanding stents [2, 227, 228].

The quantity of devitrified (crystalline) phases in amorphous materials such as silica glasses and amorphous metal alloys, can drastically affect the mechanical properties [229, 230]. For instance, Khanolkar *et al.* [231] studied the shock wave response of partially devitrified $Fe_{49.7}Cr_{17.7}Mn_{1.9}Mo_{7.4}W_{1.6}B_{15.2}C_{3.8}Si_{2.4}$ and reported that the presence of a small amount of crystalline phases within the amorphous matrix results in an outstanding elastic limit. Magnetic [232-234] and corrosion [235, 236] properties of amorphous materials are also influenced by their crystallization behavior. Zhukova *et al*. [233] explored the effect of stress annealing on magnetic properties and high frequency impedance of $Fe_{75}B_9Si_{12}C_4$ amorphous glass-coated microwires. Annealing significantly decreased the coercivity and modified the hysteresis behavior. Additionally, the coercivity, remanent magnetization, and magnetoimpedance effect of microwires was altered by changing time and temperature during the stress-annealing process. Zhou *et al*. [237] studied the effect of crystallinity percent on corrosion behavior of $Mg_{65}Cu_{25}Y_{10}$ and $Mg_{70}Zn_{25}Ca_5$ bulk metallic glasses and reported that fully amorphous BMGs possess a lower i_{corr} and more noble E_{corr} compared to their crystalline counterparts.

In order to quantify the level of devitrification of amorphous materials, many techniques have been used, including X-ray diffraction (XRD), electron backscatter diffraction (EBSD), and thermal analysis routes such as differential scanning calorimetry (DSC) [238, 239]. Among these methods, XRD is the most extensively used, following two major approaches for quantification,

either employing individual peaks in the XRD pattern or employing the entire pattern to define a relationship between the phase composition and the intensity and/or cumulative area of peaks. As an example of the former category, Hermans and Weidinger [240, 241] developed a procedure for crystallinity quantification of polymers by XRD based on three assumptions: (i) it should be possible to demarcate and measure the crystalline intensity (I_c) and amorphous intensity (I_a) of samples with varying crystallinity percentages, (ii) there is a proportionality between the experimentally measured crystalline intensity and the crystalline fraction (X_c) in the sample, and (iii) there is a proportionality between the experimentally measured amorphous intensity and the amorphous fraction (X_a) in the sample. Thus,

$$X_c = p\, I_c \tag{2}$$

$$X_a = q\, I_a \tag{3}$$

$$X = X_a + X_c \tag{4}$$

where p and q are proportionality constants. Combining these Equations, one obtains:

$$q\, I_a = X - p\, I_c \tag{5}$$

and:

$$I_a = X/q - p\, I_c/q \tag{6}$$

The values of I_a and I_c can be determined for samples with different crystallinity percentages. Plotting I_a versus I_c should result in a straight line whose slope is p/q. The intercepts on the x and y axes provide the intensity values of 100% crystalline and 100% amorphous samples, respectively. The crystallinity percentage, X_{cr}, is given by:

$$X_{cr} = \frac{X_c \cdot 100}{X} = \frac{I_c \cdot 100}{I_c + \frac{q \cdot I_a}{p}} \tag{7}$$

Although this method is widely used, it has major limitations. For samples with preferred grain orientation, the peak intensity for a specific direction is intensified leading to significant errors in the calculation. In powders, this effect could be limited by reducing the particle size by grinding. However, the process of grinding can cause other unwanted effects, such as polymorphic transformations or devitrification of amorphous samples. The crystallites should be small enough to yield reproducible diffracted intensities, but not too small since reduced particle size can lead to broadening of the XRD peaks [242, 243]. Also, determination of crystalline (I_c) and amorphous (I_a) intensities from experimentally recorded XRD patterns can be difficult because it depends on a potentially subjective determination of the baseline intensity of the pattern due to thermal and air scattering [240, 243]. Additionally, generating a calibration curve requires preparing samples with various crystallinity percentages, which is accomplished by mixing appropriate proportions of crystalline and amorphous standard phases. Here, heterogenous mixing and sampling can affect the results, especially when preparing mixtures of extreme compositions (either very dilute or concentrated) [244]. Inhomogeneity is probably the greatest source of error for many quantitative methods, especially with crystalline and amorphous components where the bulk density difference

between the two is significantly large. Problems can arise in the calibration and validation samples, as well as samples with active ingredients [245].

Nunes *et al.* [244] proposed that gradual crystallization of an amorphous component, usually through heating, is similar to incorporating a series of physical mixtures prepared with increasing percentage of crystalline component. In other words, the *in situ* crystallization method can circumvent the problem of preparing solid mixtures containing very small amounts of either crystalline or amorphous components. Generally, this technique requires using an XRD unit equipped with a hot-stage to provide high temperatures and suffers from the limited time resolution and sensitivity leading to a lack of detection of subtle changes in the crystallinity and, as mentioned earlier, the presence of an amorphous phase makes it quite challenging to precisely define the baseline in XRD patterns. In order to quantify the content of crystalline phases, XRD peaks corresponding to such phases need to be identified and labeled properly. This could be problematic for systems with phases whose peaks overlap. For the case in which one peak is assigned to more than one phase, there is always the possibility that phase identification and peak deconvolution steps cannot be implemented properly. In general, conventional XRD techniques are less accurate for characterization of nanostructured materials and samples containing amorphous phases since diffraction patterns become significantly broader and crystalline features may be less discernible.

Quantification of XRD patterns could be improved by implementing whole pattern methods. One of these commonly used techniques is Rietveld refinement, by which all reflections are simulated by calibrated crystallographic parameters [246]. However, issues such as baseline definition can result in lack of certainty over the applicability as well as accuracy of this method. Transmission electron microscopy (TEM) can be helpful in determining crystalline phases by utilizing the electron diffraction feature of this technique. Nevertheless, sample preparation

procedures are complicated, and analysis is not always straightforward, especially for fully unknown samples. Additionally, drawing a solid and reliable conclusion requires obtaining and analyzing a great many images to make sure that the results are not local. Electron backscatter diffraction (EBSD) is used for orientation determination, as well as phase identification. In this method, the EBSD pattern is generated from the diffraction of the electron beam interacting with crystallographic planes within the specimen [247], which requires accurate surface polishing and finishing of bulk samples. In order to obtain EBSD patterns of high quality and with a high indexing success rate, surface damage typically introduced during polishing should be minimized. This could be fulfilled by ion etching, using either a broad or focused beam, which is expensive and time-consuming [248, 249]. Also, in order to index the recorded pattern and distinguish between amorphous and crystalline regions, a comprehensive knowledge of the crystal structure of devitrified phases is required.

Apart from the limitations that have been highlighted for each of the methods described above, most techniques collect signals from a small region of the sample, resulting in a bias from the extreme locality of the signal. For instance, EBSD patterns are generated from the signals coming from a small interaction volume at the surface of the sample with a penetration depth of typically less than 50-100 nm [247]. This issue might be attenuated when the XRD method is utilized. Additionally, these methods provide information about the crystallinity of samples at room temperature.

DSC is superior to most other common methods used for quantifying the crystallization process of amorphous systems. The technique can partially overcome the majority of the limitations described previously. Nevertheless, most DSC studies associated with the determination of change of crystallinity of amorphous systems, have been mainly focused on

exploring the crystallization of polymers. In order to calculate the crystallinity percentage of a polymeric sample, the specific heat of fusion for a partially crystalline polymer is measured from the area under the endothermic peak in the heat flow curve and then divided by specific heat of fusion for a fully crystalline sample. The crystallinity percentage obtained from this method, however, is an average value which is valid for the temperature region around the melting point. In other words, the change of crystallinity that takes place upon heating the sample from room temperature to the melting point is not considered. In order to obtain an accurate temperature dependence of crystallinity fraction [W_c (T)] for a polymer, variation of enthalpy as a function of temperature for the sample of unknown crystallinity should be calculated and then compared using the following Equation:

$$W_c(T) = \frac{h_{am}(T) - h_s(T)}{h_{am}(T) - h_{cryst}(T)} \tag{8}$$

Where h_{am}, h_s, and h_{cryst} are the specific enthalpies of a fully amorphous sample, the test sample, and a fully crystalline sample, respectively. The specific enthalpy of the test sample (h_s) relative to a reference state at an initial temperature, T_{ini}, can be calculated from the specific heat capacity, C_p (T), as follows:

$$h_s(T) - h_s(T_{ini}) = \int_{T_{ini}}^{T} C_p(T)\, dT \tag{9}$$

Measuring the specific heat capacity is a well-known isothermal process in which the heat flow of an empty pan (baseline) is subtracted from that of the test sample. The result is then divided

by the mass of the test sample and heating rate to obtain specific heat capacity as a function of temperature. Details of this methodology are described by Höhne *et al*. [238]. This method has yielded the most accurate results compared to other approaches in polymers. However, there is no report that has extended this technique for non-polymeric systems such as amorphous alloys and silica glasses. Some researchers have attempted to quantify the crystallization process of Fe-based metallic glasses [250, 251] using an isochronal DSC experiment. This approach was introduced by Johnson-Mehl-Avrami in order to study the kinetics of isothermal solid-state phase transformations (here glass to crystal) [252, 253]. They postulated that the fraction of crystallized component is proportional to the amount of heat evolved during crystallization, which is proportional to the area under the exothermic peak associated with the crystallization [254]. The thermal evolution of the crystallized fraction, $\alpha(T)$, can then be calculated as a function of temperature for different heating rates using:

$$\alpha\left(T\right)=\frac{\int_{T_\mathrm{o}}^{T}\left(\frac{\mathrm{d}h}{\mathrm{d}T}\right)\mathrm{d}T}{\int_{T_\mathrm{o}}^{T_\infty}\left(\frac{\mathrm{d}h}{\mathrm{d}T}\right)\mathrm{d}T}=\frac{\mathrm{A}_T}{\mathrm{A}} \tag{10}$$

Where T_o and T_∞ correspond to the temperatures of onset and end of crystallization, $\mathrm{d}h/\mathrm{d}T$ is the heat capacity at a constant pressure, A_T is the area under the DSC curve between the onset temperature and a given temperature, and A is the area under the curve between onset and end of crystallization [254]. Basically, partial integration of the heat flow curve versus temperature curve results in the heat of crystallization versus temperature function. The integration method results in a "change of crystallinity" rather than "crystallized fraction" as a function of temperature. Given

Equation (10), the initial crystallinity for any sample is an unknown. Figure 27 shows a typical DSC crystallization peak of an arbitrary sample with an unknown initial crystallinity. Crystallization starts at T_1 and ends at T_3. The area under the peak between T_1 and T_3 equals A. Assuming that during heating, the sample does not undergo crystallization until it reaches T_1, the initial crystallinity could be calculated by dividing the area under the curve between T_1 and $T_2 = T_1 + \varepsilon$ by the area under the curve between T_1 and T_3.

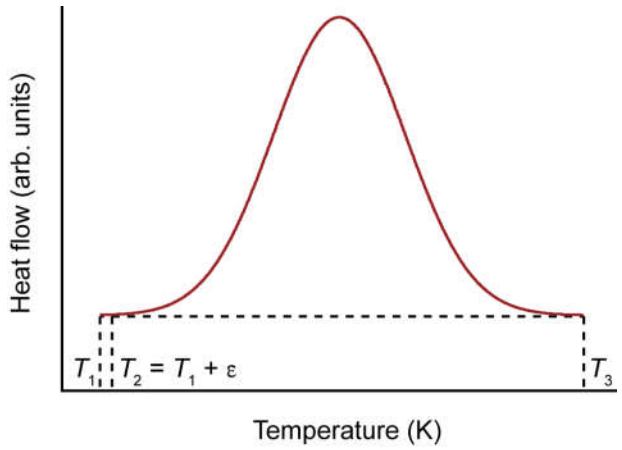

Figure 27. Schematic representation of an exothermic crystallization peak. T1 and T3 represent the temperatures at which crystallization starts and ends, respectively.

Different modes of DSC have been attempted to obtain the most reliable and accurate C_p values. Conventional DSC using a dynamic temperature program is one of the most common techniques. It consists of three segments, starts and ends with two 10- to 15-minute isothermal stabilization segments, between which a linear temperature ramp with a constant and high heating rate (10-20 K/min) is implemented [238]. In the isothermal mode, achieved by a temperature-modulated DSC (TM-DSC), there are short dynamic stages along the entire temperature range with isothermal stages before and after each heating segment to stabilize the material temperature. The temperature increase at each heating stage needs to be small, between 1 and 3 K. Since the

temperature jumps are small, the isothermal stages could be as short as 2-3 minutes ensuring thermal equilibrium of the sample [255]. Sauerbrunn *et al.* [256] claimed that temperature modulated DSC has advantages over conventional DSC for determination of heat capacity and crystallinity. However, Schawe and Hess [255] proved that the method to determine the initial crystallinity by TM-DSC does not have any advantage compared to the classical evaluation methods using conventional DSC. The claimed apparent superiority of TM-DSC over conventional DSC is simply based on a poor baseline selection. Also, the complex heating program and evaluation procedure of TM-DSC could create additional errors in the enthalpy determination [255]. Roura *et al.* [257] measured the small C_p differences between the amorphous and crystalline phases of silicon using four different approaches, namely conventional and temperature-modulated DSC at a constant heating rate and with isotherms. They concluded that conventional DSC with isotherms results in the best reproducibility for the measurement of C_p variations due to crystallization. Ferrer *et al*. [258] measured the specific heat capacity of three materials including slate, water and potassium nitrate by DSC through three different heating programs, dynamic, isostep and area methods, as described in Figure 28.

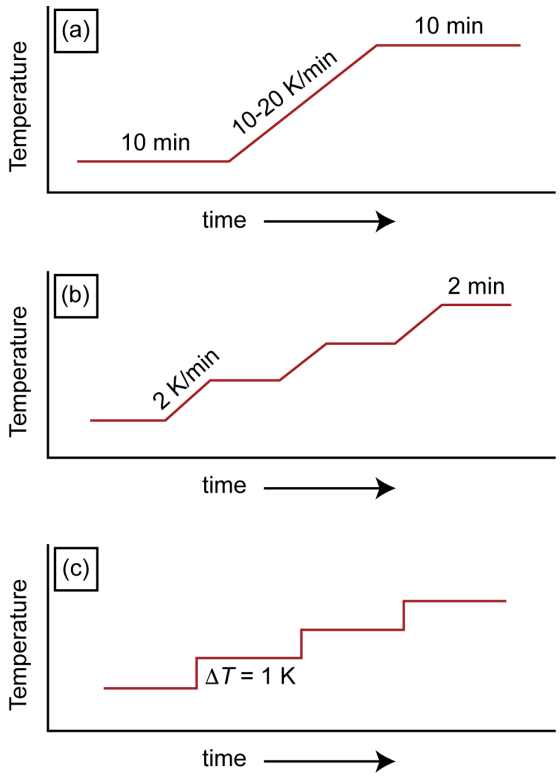

Figure 28. Three different heating programs namely, dynamic, isostep and area methods for measuring the specific heat capacity using DSC. (a) The dynamic method has an isothermal stage followed by a heating stage with a constant and high heating rate (10-20 K/min) until the final isothermal stage. (b) The isostep method consists of short dynamic stages along the whole temperature range with isothermal stages before and after each heating segment. (c) The areas method consists of consecutive isothermal segments with no heating stages in between [258]

They found relative errors smaller than 3% using the area method, while the dynamic and isostep techniques yielded values with errors up to 6% and 16%, respectively. As a consequence of high heating rates applied in the dynamic and isostep techniques, there was an abrupt temperature change at the initial and end points. Hence, DSC temperature sensors were not able to react fast enough to read and record the real temperature. Consequently, there was noise at the beginning and end of each heating segment leading to a lower measurement sensitivity.

1.13. SAM2X5 Fe-based bulk metallic glass

Recently, one of the extensively considered potential application plans has been the high-performance corrosion resistant materials program sponsored by the Defense Advanced Research Projects Agency, the Defense Sciences Office, and the U.S. Department of Energy Office of Civilian and Radioactive Waste Management [259-261]. This program led into discover a new family of Fe-based BMGs with excellent corrosion resistance which was developed as protective thermal spray coatings, such as SAM35 ($Fe_{54.5}Mn_2Cr_{15}Mo_2W_{1.5}B_{16}C_4Si_5$), SAM40 ($Fe_{52.3}Mn_2Cr_{19}Mo_{2.5}W_{1.7}B_{16}C_4Si_{2.5}$), SAM2X5 ($Fe_{49.7}Cr_{17.7}Mn_{1.9}Mo_{7.4}W_{1.6}B_{15.2}C_{3.8}Si_{2.4}$), SAM6 ($Fe_{43}Cr_{16}Mo_{16}B_5C_{10}P_{10}$), SAM7 or SAM1651 ($Fe_{48}Mo_{14}Cr_{15}Y_2C_{15}B_6$), and SAM10 ($Fe_{57.3}Cr_{21.4}Mo_{2.6}W_{1.8}B_{16.9}$). The SAM2X5 has been tested in applications as containers for the transportation, ageing and disposal of spent nuclear fuel and high-level radioactive wastes (Figure 29) [259-261].

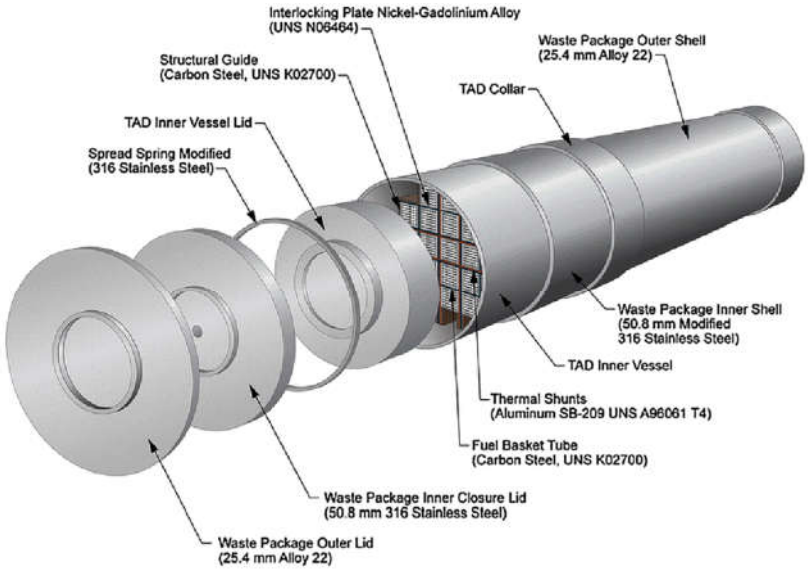

Figure 29. Spent-nuclear-fuel container with critically-control structure for 1-PWR assembly [259-261]

Due to the high boron content of SAM2X5, its neutron absorption cross section in transmission for thermal neutrons is four times larger than that of a borated stainless steel, and twice as good as a nickel-based alloy (C-4) with the additions of Gd, as shown in Figure 30 [259-261].

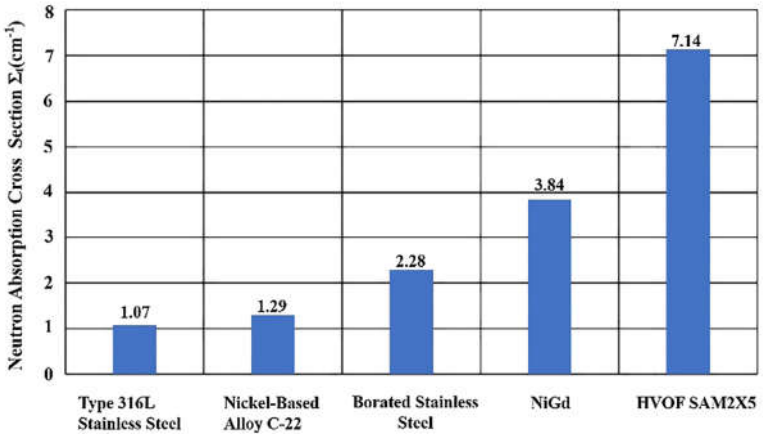

Figure 30. A comparative representation of neutron absorption cross section values in transmission for type 316L stainless steel, alloy C-22, borated stainless, a Ni-Cr-Mo-Gd alloy and SAM2X5 [259-261]

SAM2X5 has proven to be a great candidate for the applications such as the safe and long-term storage of spent nuclear fuel. Moreover, substantial cost savings may be achieved by substituting these new Fe-based BMGs for more expensive Ni-Cr-Mo and Ni-Cr-Mo-Gd alloys. In addition, the SAM2X5 and SAM1651 amorphous coatings with high hardness and low corrosion rates are being used as corrosion-resistant anti-skid decking for ships and disk cutters for tunnel-boring machines [259-261]. In addition to a very high corrosion resistance behavior, SAM2X5 has unique mechanical properties as well. Khanolkar *et al* [231], studied the effect of partial crystallization on the shock wave adsorption of sintered SAM2X5. They prepared bulk samples with different crystallinity percentages by spark plasma sintering of amorphous SAM2X5 powder at different temperatures of 600ºC (SAM2X5-600) and 630ºC (SAM2X5-630) for which

they recorded the Hugoniot Elastic Limit (HEL) of 8.58±0.53 GPa and 11.76±1.26 GPa, respectively (Figure 31). The latter HEL result is higher than elastic limits for any BMG reported in the literature thus far. Another interesting observation in this research was that by increasing the sintering temperature and consequently inducing a higher percentage of crystallinity in the bulk specimens, the catastrophic loss of post-yield strength transformed to strain-softening and retention of strength beyond the HEL. Thus, the presence of crystallinity within the amorphous matrix is seen to significantly aid in strengthening the material as well as preserving material strength beyond yielding [231]. Although efforts have been made to semi quantitatively calculate the crystallinity percentage in sintered SAM2X5 system, it is very challenging to pinpoint the crystallinity percentage as a function of temperature [262]. The reason is that there are eight elements in the chemical composition of SAM2X5 and upon its devitrification there are many possibilities for the formation of different phases. This makes it quite impossible to identify the products of crystallization with 100% of certainty. As a result, XRD method which is a very common technique for quantification of crystallization process in amorphous systems to become infective for quantitative analysis of crystallization of SAM2X5 system. percentage are determined as a function of temperature.

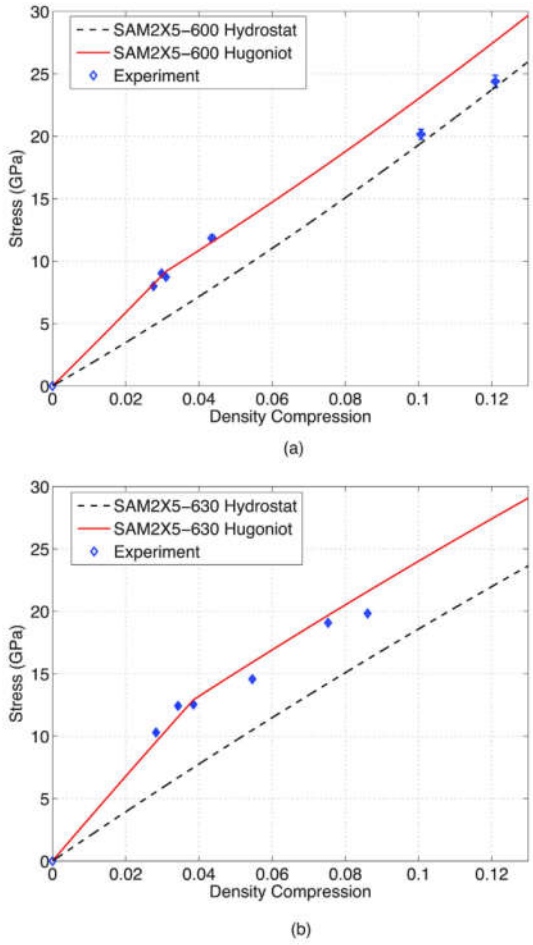

Figure 31. Calculated Hugoniot (solid line), hydrostat (dashed line) and experimental data (solid diamond marker) for (a) SAM2X5-600 and (b) SAM2X5-630 [231].

In response to the issues described above, here we present a DSC technique that can quantify the amount of devitrified phase in amorphous metal alloys over a broad range of temperatures. We calculate the heat capacity, enthalpy, change of crystallinity, and crystallinity percentage of partially devitrified Fe-based amorphous powders using a conventional DSC with a dynamic temperature program. Specific heat capacity is calculated from the heat flow curve through the integration of C_p, then an enthalpy function is obtained from which the change of crystallinity and crystallinity. In the next step, evaluate mechanical properties of sintered

specimens under quasi-static and dynamic deformation regimes and, through a mechanistic study, a correlation between crystallinity percentage and mechanical properties will be established.

Chapter 2

Experimental Procedure

2. Experimental Procedure

2.1. Structural analysis

Amorphous SAM2×5 powder with a chemical composition of $Fe_{49.7}Cr_{17.7}Mn_{1.9}Mo_{7.4}W_{1.6}B_{15.2}C_{3.8}Si_{2.4}$ was used as a starting material. To fully crystallize the amorphous SAM powder, a heat treatment to a temperature of 1323 K was implemented using a heating rate of 30 K/min in a Lindberg 59744-A tube furnace. The heat treatment time was 2 hours under a high purity N_2 atmosphere (99.999%). The powder was subsequently cooled to room temperature in the protected N_2 atmosphere.

X-ray diffraction (XRD) patterns at room temperature were obtained using a D2 Phaser (Bruker AXS, Madison, WI) using a step size of 0.014 degrees 2θ, Cu Kα radiation, and a count time of 3 s by scanning from 30 to 90 degrees 2θ. In order to determine the devitrified phases during the crystallization process, high temperature *in situ* XRD experiments were also completed in high-purity helium and 4% hydrogen in nitrogen on a D8 Advance system (Bruker AXS, Madison, WI) with an Anton Paar HTK 1200N furnace and Cu anode X-ray tube. Heating rate was set to 30 K/min for heating between scans. Hold (scanning) time for each measurement was 30 minutes. Scan step was 0.03° and count time was 1 s/step, which corresponds to a scanning rate of 1.54°/minute. Thermal analyses were carried out by differential scanning calorimetry (SDT Q600, TA Instruments, New Castle, DE) using a heating rate of 30 K/min to a temperature of 1273 K in flowing argon. Alumina crucibles of 90 μL capacity were used. All alumina pans were taken through a homogenization process, consisting of heating and cooling under the same conditions as the SAM2×5 powders in the DSC instrument. For the DSC experiments, approximately 100 mg of powder were loaded into an alumina pan and an empty alumina pan was used as a reference.

Powder samples with five different crystallinity percentages were prepared by mixing the appropriate amounts of amorphous and crystalline SAM2×5 powders. For each crystallinity percentage, three independent samples were prepared and tested using DSC. The amounts are tabulated in Table 2.

Table 2. Nominal crystallinity, chemical composition and average true crystallinity of powder batches prepared by mixing amorphous powders and crystalline powders.

Sample	Nominal crystallinity (%)	Mass of amorphous powder (mg)	Mass of crystalline powder (mg)	Average crystallinity (%) ± standard deviation
SAM5%	5	95.0	5.1	5.1 ± 0.1
		95.1	5.2	
		94.9	4.9	
SAM20%	20	80.2	20.0	20.0 ± 0.1
		80.1	19.8	
		80.1	19.9	
SAM40%	40	60.2	40.0	40.0 ± 0.2
		59.9	40.3	
		60.0	39.8	
SAM60%	60	40.1	59.9	60.0 ± 0.1
		39.8	59.9	
		40.2	60.1	
SAM80%	80	20.2	80.1	80.0 ± 0.1
		19.9	79.9	
		19.9	80.2	

Contrary to most conventional characterization techniques, the sample preparation for DSC experiments is not sensitive to the need for homogeneous mixing, since the heat flow measured by DSC is acquired from the whole material mass inside the crucible regardless of how homogenous it has been mixed and prepared. This could be considered one of the advantages of the DSC method. The heating program consisted of an isothermal heating at 323 K for 30 minutes, followed by heating from 323 K to 1208 K with a heating rate of 30 K/min, and finally another isothermal segment at 1208 K for 30 minutes. Isothermal dwell times of 30 minutes guarantees the thermal equilibrium of the sample. Additionally, a maximum temperature of 1208 K was selected because it lies between the completion of crystallization and the melting temperature (about 1473 K) of the SAM2×5 material. Using this temperature program, heat flow curves for the empty pans and the test samples were recorded under a high purity Ar atmosphere (99.999%). In order to obtain reliable and accurate results, system calibrations were completed. The TGA weight calibration made use of alumina standard specimens and the DSC heat flow calibration made use of sapphire standard specimens. After calibration, testing was completed on an empty pan, followed by testing of an amorphous powder loaded into the same alumina crucible. This cycle, including system calibration, was repeated for the crystalline and partially devitrified samples.

2.2. Evaluation of mechanical properties

Now that we succeeded to develop the precise DSC-based methodology to pinpoint the crystallinity in SAM2X5 system, we can proceed to produce bulk samples, determine their crystallinity percentage using DSC, and evaluate the mechanical properties of the bulk samples. In order to break the agglomerates, the powder was tumbled in a 125mL high-density polyethylene

wide-mouth bottle with a polypropylene cap containing 80g of powder along with 80g of zirconia ball (~6mm diameter) for 24h at a speed that maximized cascading. For powder densification, pre-determined mass of SAM powder was loaded into a graphite die (Ohio Carbon, AR14) with an inner diameter of 19mm, lined with graphite foil. The powder was uniaxially pressed at 100 MPa for 5 minutes in the die and plunger assembly, followed by lining the sample/plunger interfaces with graphite foil. The die was loaded into a custom built, current-activated, pressure-assisted densification (CAPAD) apparatus (commonly referred to as spark plasma sintering, SPS), that can be described elsewhere [263]. After reaching a vacuum of 2.5E-2 torr, the sample was uniaxially pressed to 100 MPa. As the final applied stress was reached, the sample was heated to temperature (INSERT RANGE) at a rate of 500°C/min using a PID controller, monitored by a thermocouple inserted into the side of the die that was approximately ¼ inch the edge of the sample. Final temperatures were between 888K and 948K, under a pressure of 30kN, vacuum, and maintained for an amount of time 0 min. Upon reaching the specified temperature, the current was killed, and the sample quench cooled. The load was removed upon cooling to 500°C, and the sample was subsequently removed from the chamber and extracted from the die assembly. The density of samples was measured with Archimedes method using water as a liquid. The microstructure of sintered specimens was explored using scanning electron microscopy (SEM) (FEI™ Quanta 250, FEI Company, Hillsboro, OR) and high-resolution transmission electron microscopy (HR-TEM) (JEM ARM-200CF). Porosity of each sintered specimen was quantified using image processing software ImageJ. Five micro-pillars with a diameter of 3 μm and height of 8 μm were machined from sintered specimens using a dual focus ion beam (FIB) system (FEI Company, Hillsboro, OR) using a gallium ion beam. The pillars were slightly tapered due to the divergence of the Ga ion beam and the convergence angle was smaller than 2.5°. Initially, high currents of ~30 nA were

used to mill craters around micropillars with larger than targeted diameters. Then in order to prevent FIB damage or possible crystallization caused by the gallium ions, a very low FIB current of about 0.1 nA was used in the final trimming step. In this case, the beam energy during FIB milling was limited to 3 kV•nA, which is well below the threshold value to induce significant sample damage or partial crystallization in the metallic glasses [264]. For micro-compression testing, the micropillars were compressed on a TI 950 HYSITRON TriboIndenter (Hysitron, Minneapolis, MN, USA) at a strain rate of 10^{-3} s^{-1}, room temperature, and under a displacement-control mode. Microhardness measurements were carried out using a Vickers diamond pyramidal indenter (LM-810AT, Leco Co., USA) on mirror finish metallographic samples with an applied load of 300gf and dwell time of 15s. Ten indentations were implemented on each sample and the averaged values are reported. In order to calculate the indentation toughness (Kc), a higher load of 1kgf was applied to form cracks at the corners of indents. Compression tests were performed at a strain rate of 10^{-3} s^{-1} (quasi-static regime) and room temperature using a 3367 Dual Column Testing System (Instron, Norwood, MA 02062-2643) equipped with a 30 kN load cell. Five measurements were carried out on each sample. Disk-shape specimens with a diameter of 3mm and length of 4.5mm were cut from the sintered samples using electrical discharge machining (EDM) method. In order to do micro compression test, FIB-ed micropillars were compressed in HYSITRON TriboIndenter (Model: TI 950, Manufacturer: Hysitron, Minneapolis, MN, USA) with a strain rate of 10^{-3} s^{-1}, at room temperature, and under a displacement-control mode. Post-mortem SEM characterization was carried out on compressed samples (disks and micro pillars).

Ultrasound measurement were carried out to obtain shear modulus, Young's modulus and Poisson's ratio of sintered specimens. The measurement system consists of an Olympus 5077 PR pulser/receiver; two V106-RM P-wave sensors (Olympus, 2.25 MHz, 0.5" diameter). and two

V154-RM S-wave sensors (Olympus, 2.25 MHz, 0.5" diameter). The density, ρ, is calculated via Archimedes methodology. Using the calculated density, the Young's modulus, shear modulus and Poisson's ratio are each calculated. With a pulser/receiver, to compute the wave speed, the round-trip transit time through an area of known thickness with both P-wave and S-wave transducers must be recorded. The Equation for either P- or S-wave speeds, c, is:

$$C = \frac{2L_S}{\Delta t} \tag{11}$$

Where L_s is the thickness of specimen and Δt is one-time trip transit time (the wave transit from one surface to another surface once). It is noted that the signal peak was used as a characteristic to determine the reflection of waves. For P-waves, the compressive wave is reflected into the tension wave so that the next that peak is chosen has the reverse direction of the first peak. For S-wave, the shear wave is kept the same wave, so that the next peak has the same direction, either positive or negative, as the first peak. In general, three or more good transit time with the possibly highest signal-to-noise ratios (SNR) are chosen and the average is reported. The wave speed used to calculate Poisson's ratio, v, is defined in Equation (12).

$$\vartheta = \frac{1-2(\frac{C_S}{C_p})^2}{2-2(\frac{C_S}{C_p})^2} \tag{12}$$

Where C_s is shear wave speed and C_p is longitudinal wave speed. The shear modulus, G, is calculated in Equation (13) by multiplying the square of the shear wave velocity and the density of the test specimen.

$$G = \rho C_S^2 \tag{13}$$

Young's modulus, E, can be expressed by Equation (14):

$$\mathrm{E} = \frac{\rho \mathrm{C}_\mathrm{p}^2 (1+\vartheta)(1-2\vartheta)}{(1-\vartheta)} \tag{14}$$

It is noted that when the units of wave speed and density are km/s and g/cm^3, respectively, then Young's modulus will be expressed in units of GPa.

Chapter 3

Results and discussion

3. Results and discussion

3. 1. DSC-based methodology for determination of crystallinity percentage

Figure 32 illustrates the XRD patterns of the amorphous and crystalline SAM powders. The amorphous SAM powder exhibits the typical broad pattern confirming its amorphous nature. The crystalline SAM powder exhibits sharp peaks belonging to carbides, borides, oxides and metallic iron.

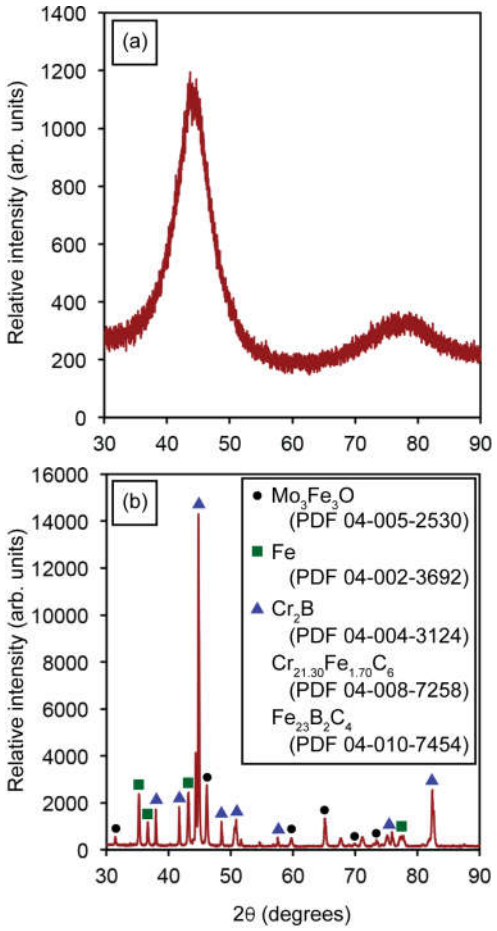

Figure 32. X-ray diffraction patterns of (a) amorphous and (b) crystalline SAM2×5 powders. The crystalline powders were obtained by heat-treating the amorphous powders at 1323 K for 2 hours under nitrogen atmosphere.

The SAM2×5 amorphous powder was initially characterized using DSC (Figure 33) resulting in a glass transition temperature (T_g) of ~883 K. The crystallization process initiated at T_{x0} = 918 K followed by three additional crystallization events at T_{x1} = 953 K, T_{x2} = 988 K, and T_{x3} = 1098 K. Finally, SAM2×5 achieved full crystallinity at T_{crys} = 1173 K.

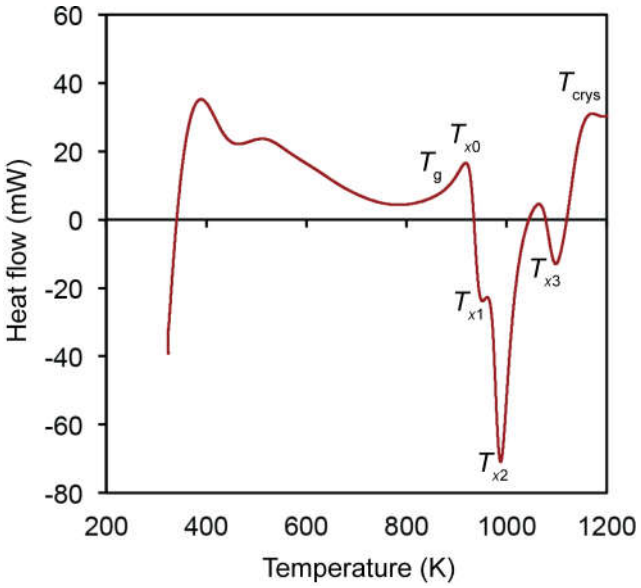

Figure 33. Heat flow curve of amorphous SAM2×5 powder obtained using a heating rate of 30 K/min in an argon atmosphere.

Figure 34 describes the methodology used in this study in order to calculate the crystallinity percentage. In the first step, heat flow curves are determined for an empty pan, an amorphous sample, a partially crystalline sample, and a fully crystalline sample [238]. Then, the change of crystallinity of a sample is calculated based on the change in enthalpy as a function of temperature, which is derived by the integration of the specific heat capacity curve using Equation (8).

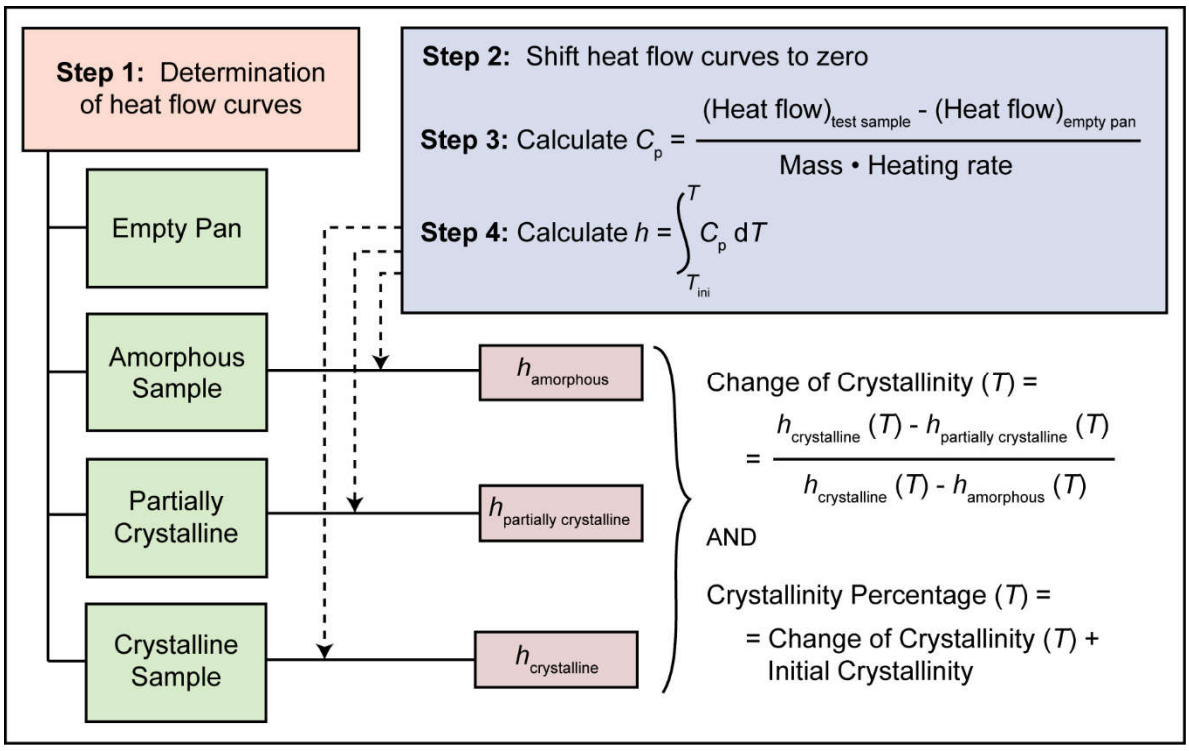

Figure 34. A schematic representation of our DSC-based methodology for determination of the change of crystallinity and crystallinity percentage.

For this purpose, using the heating program described in the previous section, the heat flow of an empty alumina pan is first recorded with respect to time. In a second experiment, the same pan is loaded with powder test sample and recorded [Figure 35(a)]. In both cases, an empty alumina pan is used as a reference. Then, the initial isothermal segment of the heat flow curves of both the empty alumina pan and test sample are shifted upwards or downwards for an initial heat flow of zero, as illustrated in Figure 35(b). Hereafter, since we aim at calculating the crystallinity percentage of the specimen at an arbitrary temperature, heat flow curves as a function of temperature, instead of time, will be used for further calculation. DSC units can provide a heat flow curve as a function of both time and temperature.

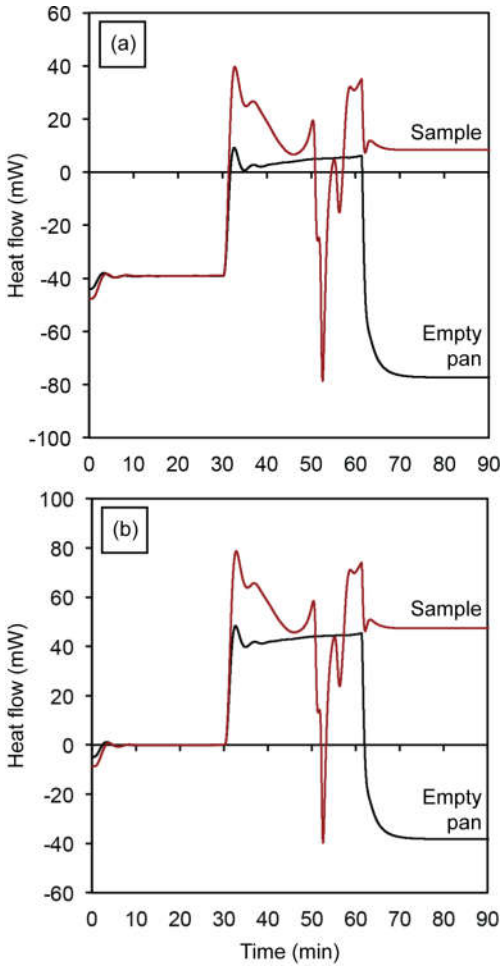

Figure 35. Heat flow curves of an empty alumina pan and the same pan loaded with powder test sample (a) as-recorded by differential scanning calorimetry and (b) after shifting upwards so that the initial isothermal segments start at zero heat flow.

Figure 36 illustrates typical heat flow curves recorded for the empty pan, the amorphous SAM2×5 powder, the powder mixture of SAM5%, and the crystalline SAM2×5 powder with respect to temperature. Crystallization of the amorphous SAM2×5 powder takes place at temperatures between 918 K and 1173 K [Figure 33 and Figure 36(a)]. The exothermic crystallization peaks shrink slightly for sample SAM5% [Figure 36(b)]. The crystallization peak in amorphous metallic systems is preceded by another exothermic event that spans a wide temperature range from approximately 600 to 900 K, as seen in the graphs of Figure 36(a)-(b).

This exothermic event represents the structural relaxation of the amorphous phase whose existence in fully crystalline SAM powder [Figure 36(c)] could be due to the existence of a very small content of amorphous phase in this powder.

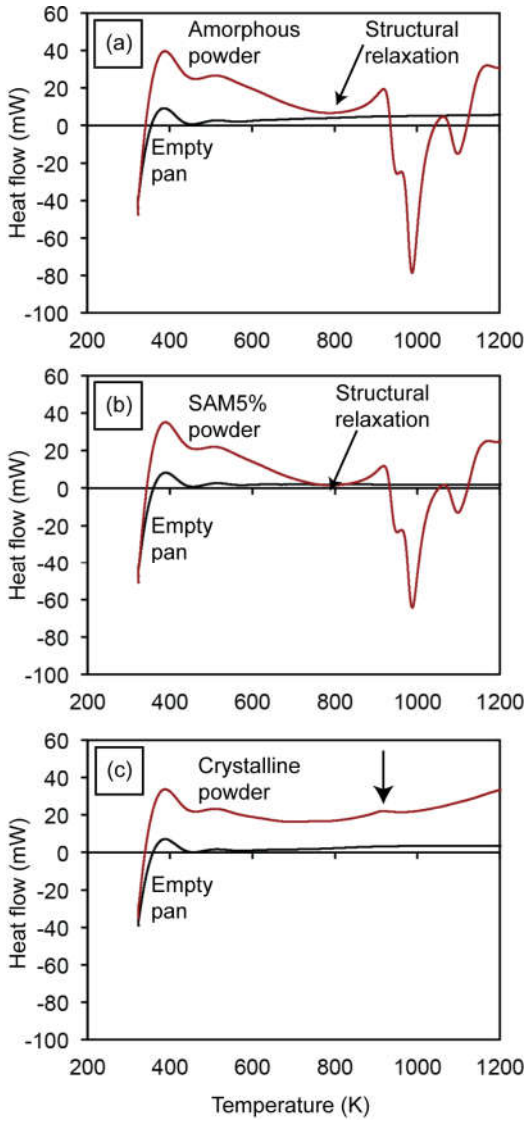

Figure 36. Heat flow curves of (a) empty pan and amorphous SAM2×5 powder, (b) empty pan and SAM5% powder mixture with a known initial crystallinity, and (c) empty pan and crystalline SAM2×5 powder, where the arrow represents a crystallization peak. Downward peaks in these charts represent exothermic reactions.

In the next step, the heat flow of the empty pan is subtracted from that of the pan containing the test powders, which results in the heat flow through the powder sample. This value is divided by the mass of the test powders and heating rate to obtain the apparent heat capacity of the powder sample. Figure 37 illustrates the apparent heat capacity curves for the three samples. The C_p value of the crystalline SAM2×5 powder is about 0.5 J/g•K, which is in a good agreement with that of steels [265].

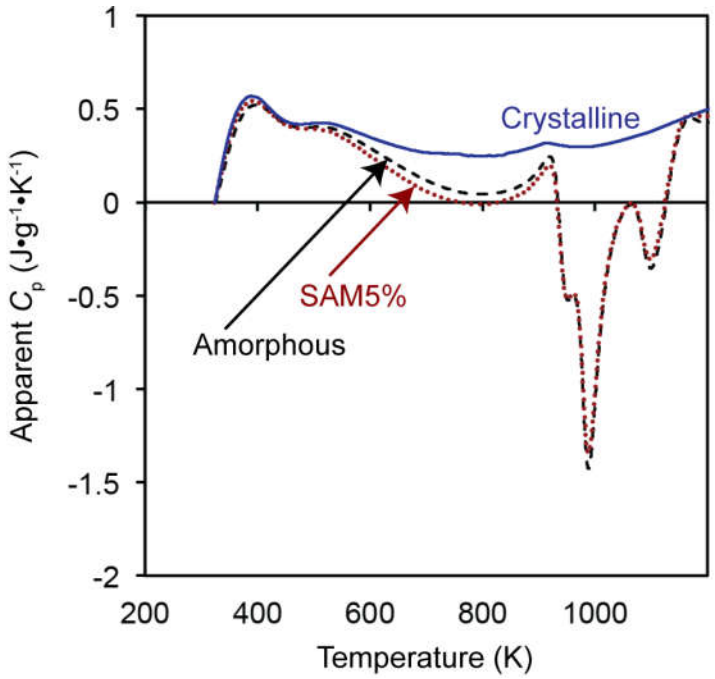

Figure 37. Apparent heat capacity, C_p, of amorphous, SAM5%, and crystalline powders as a function of temperature.

Subsequently, the variation of enthalpy for each sample is calculated using Equation (9) by integration of the apparent heat capacity curves. These calculations result in curves illustrated in Figure 38. For the sake of simplicity in the calculation, the initial enthalpy of each sample is assumed to be zero. The initial enthalpy can be any arbitrary value since the change of enthalpy is taken into consideration in subsequent calculations. Above 1173 K, where the crystallization

process ends, the *h* curves of all samples become parallel and linearly increase with an increase of temperature. The difference between the enthalpy of the SAM5% sample with that of the crystalline sample is proportional to the temperature-dependent change of crystallinity of the SAM5% sample.

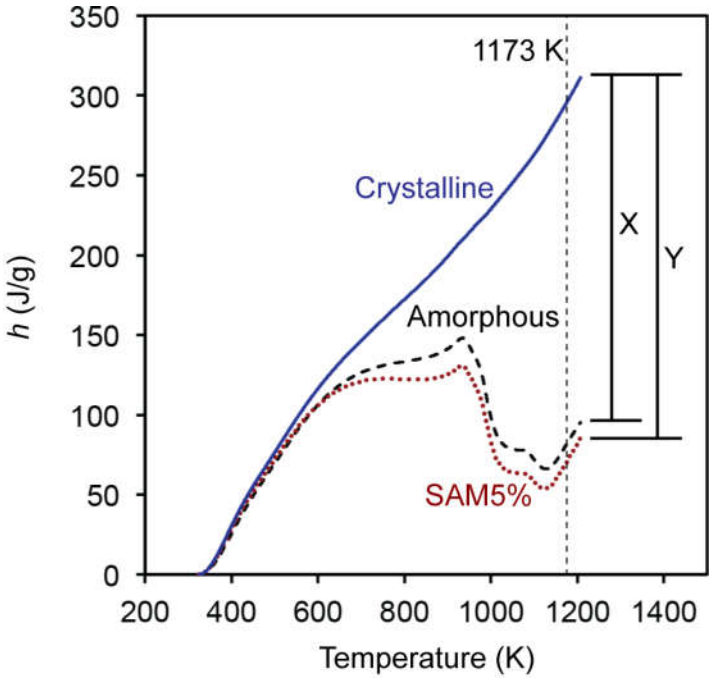

Figure 38. Enthalpy of amorphous, SAM5%, and crystalline powders as a function of temperature. The difference between the enthalpy curves of the amorphous and crystalline powder samples at temperatures above 1173 K (shown by an X) represents the enthalpy difference between amorphous and crystalline states, which is the crystallization enthalpy of amorphous SAM2×5 and is a constant value. The difference between the enthalpy curves of SAM5% and crystalline powder at any arbitrary temperature (shown by a Y) yields the crystallization enthalpy of SAM5% at that specific temperature. Therefore, Y is a function of temperature.

The difference between the enthalpy curves of the amorphous and crystalline powder samples at a temperature above 1173 K (shown by an X in Figure 38) represents the enthalpy difference between amorphous and crystalline states, which is basically the crystallization enthalpy of amorphous SAM2×5 and is a constant value. On the other hand, the difference between the enthalpy curves of SAM5% and crystalline powder at any arbitrary temperature (shown by a Y in

Figure 38) yields the crystallization enthalpy of SAM5% at each temperature across the curve. The line representing Y is moved from left to right at each point and used to obtain a value at each temperature. Therefore, Y is a function of temperature. Dividing the enthalpy difference between SAM5% and crystalline SAM2×5 (Y in Figure 38) by the difference between the enthalpy curves of the amorphous and crystalline powder samples at temperatures above 1173 K (X in Figure 38), yields the change of crystallinity as a function of temperature, as illustrated in Figure 39.

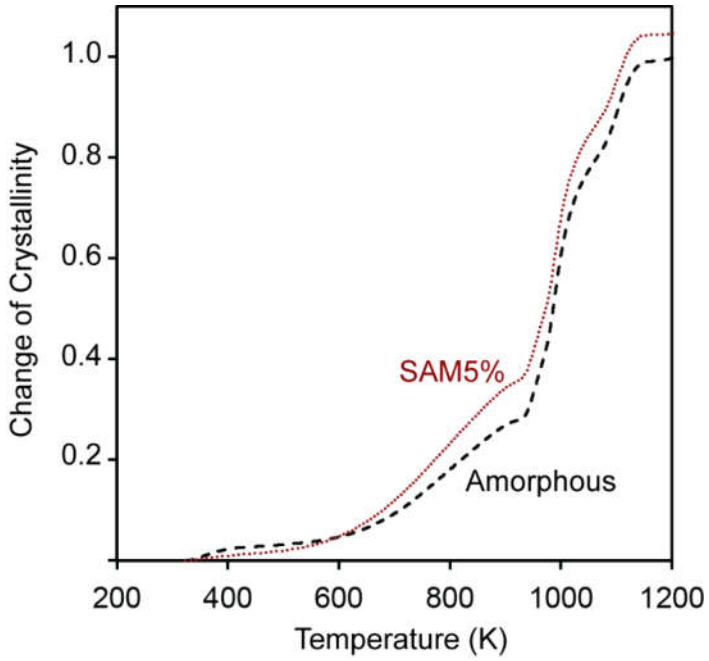

Figure 39. Variation of change of crystallinity as a function of temperature for amorphous and SAM5% powders as a function of temperature.

One can see that in Figure 38, the magnitude of X at 1173 K, which represents the crystallization enthalpy of amorphous SAM2×5, is smaller than that of Y, which is the crystallization enthalpy of partially devitrified SAM5%. Unfortunately, this will cause the change of crystallinity of SAM5% to be greater than that of the amorphous SAM2×5 powder (Figure 39), an unexpected situation since one would expect the amorphous sample to have a greater change in

crystallinity as the devitrification process evolves. Such abnormalities were not observed for other test samples with crystallinity percentages of 20, 40, 60, and 80%. The reason for this effect is that SAM5%, due to its very low crystallinity, has a crystallization enthalpy close to that of amorphous SAM2×5. As will be discussed later, we developed a procedure for correcting enthalpy curves that resolves this issue. Also, as seen in Figure 39, the crystallization process for both samples starts at a temperature between 473 K and 573 K, gradually increases until 923 K, and is followed by a more rapid crystallization process ending around 1173 K. According to previous results [201, 266-269], there is no crystallization event below the T_g of amorphous materials. The degree of disorder in amorphous metals partially depends on the occurrence of short-range order (SRO), which involves changes of the local order such as rearrangement of neighboring atoms and local bond lengths. Annealing a metallic glass below the glass transition temperature can disturb the SRO. This process is known as structural relaxation. Van Den Beuker and Radelaar [269] proposed a model for short range order that considers two different processes: (i) chemical short range order (CSRO) which is associated with redistribution of the constituent atoms, known to be reversible and is more or less analogous to short range order in crystalline alloys [267, 268] and (ii) topological short range order (TSRO) which is connected to topological changes, decreased atomic spacing and change of material volume, and generally attributed to irreversible relaxation [267, 268]. At lower temperatures, the more ordered states are favored while at higher temperatures the more disordered states dominate. Hence, temperature-dominant metastable equilibrium states would dominate. Given that true equilibrium takes place when the crystalline state is reached, CSRO and TSRO processes independently relax towards the equilibrium states [269]. What takes place below the glass transition temperature is, in fact, structural relaxation phenomena that eventually results in crystallization starting at T_g. In other words, below the glass transition

temperature we are facing densification of the glass (accompanied by a decrease in enthalpy) and possibly formation of nano-sized nuclei that enable the crystallization process above T_g (cold crystallization) [270-272]. Also, there are many reports that associate the exothermic reactions just before the glass transition to the annihilation of free volume and structural relaxation [273-276]. Figure 36 shows this feature in the heat flow curves of the amorphous, SAM5%, and crystalline samples. In order to make sure that final crystallinity values are not affected by the structural relaxation effect, regardless of its origin, the enthalpy curves for powders need to be corrected. For this purpose, as will be discussed in detail later, we can safely ignore the sections of the enthalpy curves below the temperature of crystallization. Here, we disregard the enthalpy change below 898 K, which is slightly below the temperature of crystallization onset. In order to finalize the analysis, the next step is to move the enthalpy curve of the amorphous SAM2×5 powders upwards to fit that of the crystalline sample at 1173 K [Figure 40(a)]. This is necessary because after crystallization is completed, both samples are ideally the same (*i.e.*, both are fully crystalline), and the enthalpy curves for both samples above the completion of crystallization (above 1173 K) match each other, as seen in Figure 40(a). During heating of the sample, there are two temperatures at which the slope of the enthalpy curve of the amorphous sample changes.

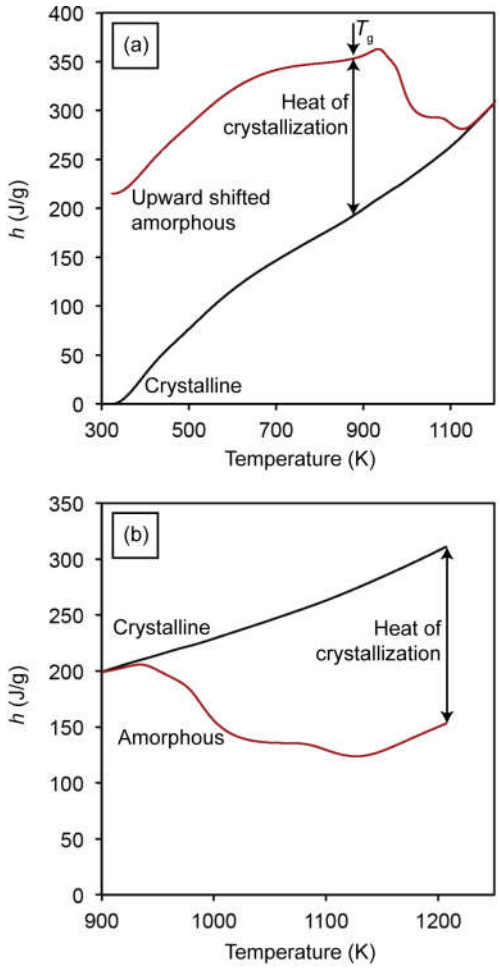

Figure 40. (a) Upward-shifted enthalpy curve of the amorphous powders and of the crystalline powders and (b) downward-shifted enthalpy curve of amorphous powders and of the crystalline powders.

The first one happens at around 573 K, which indicates the initiation of structural relaxation, and the second one occurs at around 883 K, which is the glass transition temperature. The difference between the enthalpy values of the amorphous and crystalline SAM2×5 samples at T_g indicates the true heat of crystallization, marked in Figure 40(a) with a two-sided arrow. However, for a more straightforward calculation, it is possible to move the original enthalpy curve of the amorphous SAM2×5 sample, shown in Figure 40(a), downward until it matches that of the crystalline SAM2×5 sample at T_g. We set this point at 898 K, slightly below 918 K, as illustrated in Figure 40(b). We can safely ignore the enthalpy curves below 898 K, as justified earlier, and

consider the region beyond that for further calculations. In this case, the difference between the enthalpy curves of the amorphous and crystalline SAM2×5 samples at the maximum temperature indicates the corrected heat of crystallization of the amorphous SAM2×5, which is constant value. By dividing the difference between the enthalpy of the amorphous and crystalline SAM2×5 samples, at any arbitrary temperature, by the corrected heat of crystallization (a constant), the change of crystallinity of the amorphous SAM2×5 as a function of temperature can be determined. As the temperature of the amorphous sample is increased and reaches the maximum temperature, it becomes fully crystalline, resulting in a change of crystallinity of 1 (or 100% for crystallinity percentage).

Implementing for the SAM5% sample, the change of crystallinity of the amorphous SAM2×5 and SAM5% samples can be obtained, as illustrated in Figure 41(a) using the following Equation:

$$\mathrm{CC}\left(T\right)=\frac{h_{\mathrm{crystalline}}\left(T\right)-h_{\mathrm{SAMX\%}}\left(T\right)}{h_{\mathrm{crystalline}}\left(T_{\max}\right)-h_{\mathrm{amorphous}}\left(T_{\max}\right)} \tag{15}$$

Where $h_{\mathrm{SAMX\%}}$ would correspond to the enthalpy for the SAM5% sample (i.e., $h_{\mathrm{SAM5\%}}$). The initial crystallinity of SAM5% would be the difference between change of crystallinity of the amorphous SAM2×5 and SAM5% powders at the maximum temperature. This process results in a value of approximately 0.04 for one set of SAM5% powders. Moreover, by adding this initial crystallinity value to the change of crystallinity curve at all temperatures for SAM5%, the crystallinity percentage as a function of temperature can be obtained [Figure 41(b)]:

$$\text{Crystallinity Percentage} = \left[\text{CC}(T) + \text{Initial Crystallinity} \right] \bullet 100 \qquad (16)$$

For the case of the SAM5% powders, the sample starts with a crystallinity of 4% (*i.e.*, this is the initial crystallinity). By increasing the temperature to about 1173 K, the crystallinity percentage gradually increases and reaches 100%. Further increases in temperature do not change the crystallinity, as evidenced by the flattening of the curve in Figure 41(b).

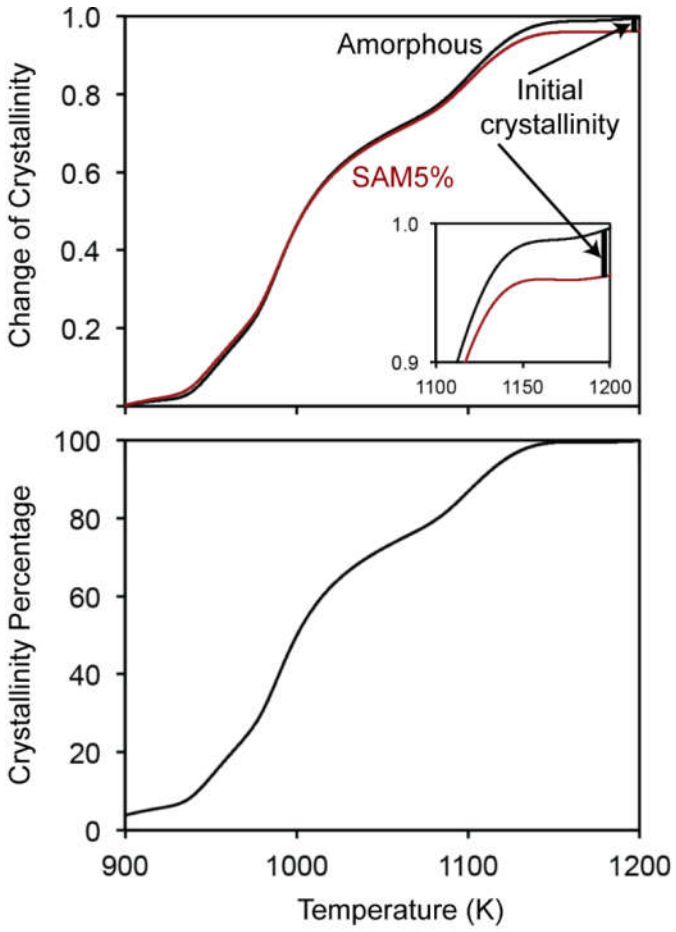

Figure 41. (a) Change of crystallinity of amorphous and SAM5% powders and (b) crystallinity percent of SAM5% powders as a function of temperature.

Crystallinity percentages of powder mixtures of SAM20%, SAM40%, SAM60% and SAM80% were calculated similarly and the results are graphed in Figure 42. Error bars along X- and Y-axis represent uncertainty associated with corresponding values which will be discussed thoroughly latter. There is a linear relationship, with a slope close to 1 and intercept of almost zero, between the crystallinity percentage calculated from DSC data and the true crystallinity based on the initial powder mixtures. In other words, the crystallinity values calculated from DSC data equal that of known samples and consequently there is no need to obtain calibration curves. This is one of the merits of our DSC-based methodology. The technique eliminates the need for preparing calibration samples (with known crystallinity percentages), which can increase the uncertainty of results when it comes to preparing mixtures of extreme compositions [244].

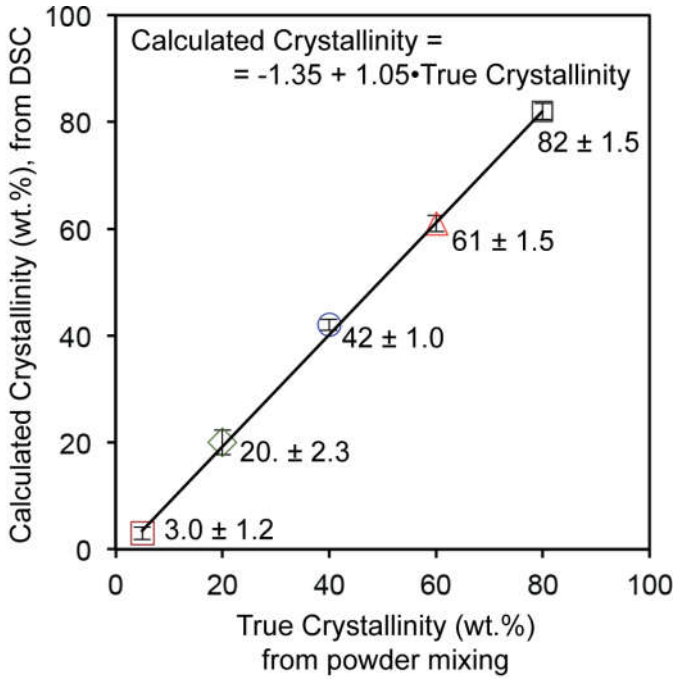

Figure 42. Correlation between calculated crystallinity from DSC results and the true values based on initial known crystallinity of mixed powders.

Figure 43(a)-(g) shows the increasing crystallinity of prepared powder mixtures. A truncated view of the XRD patterns of the amorphous SAM2×5 and SAM5% powders in a 2θ range between 30 and 60 degrees is illustrated in Figure 43(h).

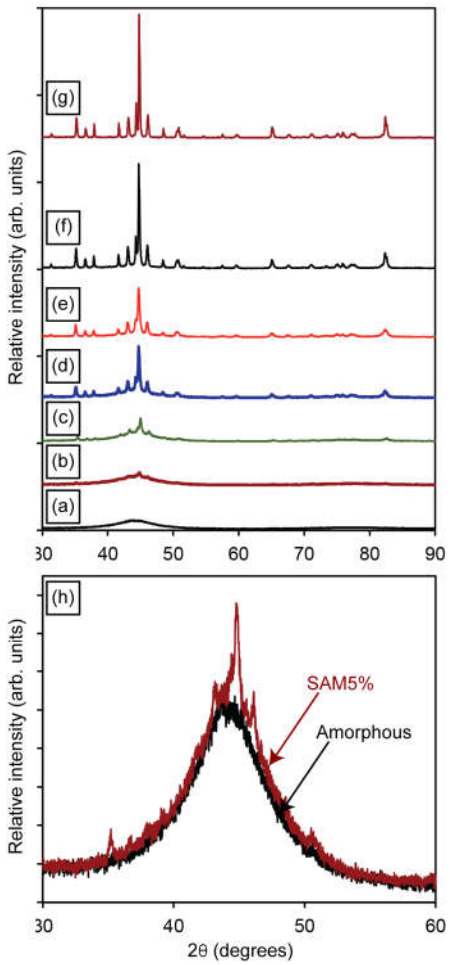

Figure 43. XRD patterns of (a) amorphous, (b) SAM5%, (c) SAM20%, (d) SAM40%, (e) SAM60%, (f) SAM80%, and (g) crystalline powders. (h) Truncated view of XRD pattern of amorphous and SAM5% powders over the 2θ range of 30 to 60 degrees.

Despite using a very slow scan rate in XRD, the patterns of amorphous SAM2×5 and SAM5% are very similar, thus it is impossible to quantify the crystallinity of SAM5% via XRD methods. This limitation is expected since the resolution of the XRD technique is about 5 wt.% for specimens without light-weight elements such as carbon and boron [277]. Lack of accuracy of

XRD quantification becomes more significant for SAM2×5 materials, which have both boron and carbon at relatively high concentrations. Difficulty in identifying the devitrified phases in SAM2×5 is another reason that precludes XRD as a technique for studying the quantification of crystallization of SAM2×5. However, DSC can overcome the XRD limitations and yield a crystallinity percentage of 3.0 ± 1.2% for SAM5%. We clarify that the crystallinity percentage of 4% obtained for the SAM5% powder [Figure 41(a)] is only from one measurement. However, the numbers reported in Figure 42 are average values determined from three independent measurements. Thus, resulting in a more accurate value that now also contains a standard error.

In order to confirm that the exothermic signals observed in DSC curves belong to the crystallization events and not phase transformations from one crystalline state to another, high temperature, *in situ* XRD experiments were completed on the amorphous SAM2×5 powder from 823 to 1273 K. The results are illustrated in Figure 44. At all temperatures below T_g (883 K), there is no sign of crystallization. At a temperature of 898 K, which is between T_g and the temperature of initial crystallization, peak splitting begins, indicating initiation of devitrification. Iron is the first phase that crystallizes. At around 1023 K the crystallization of carbide and boride phases then follows. Although experiments were conducted in a hydrogen atmosphere, at a temperature around 1023 K, oxides also start to form, and the quantities increase as the temperature increases.

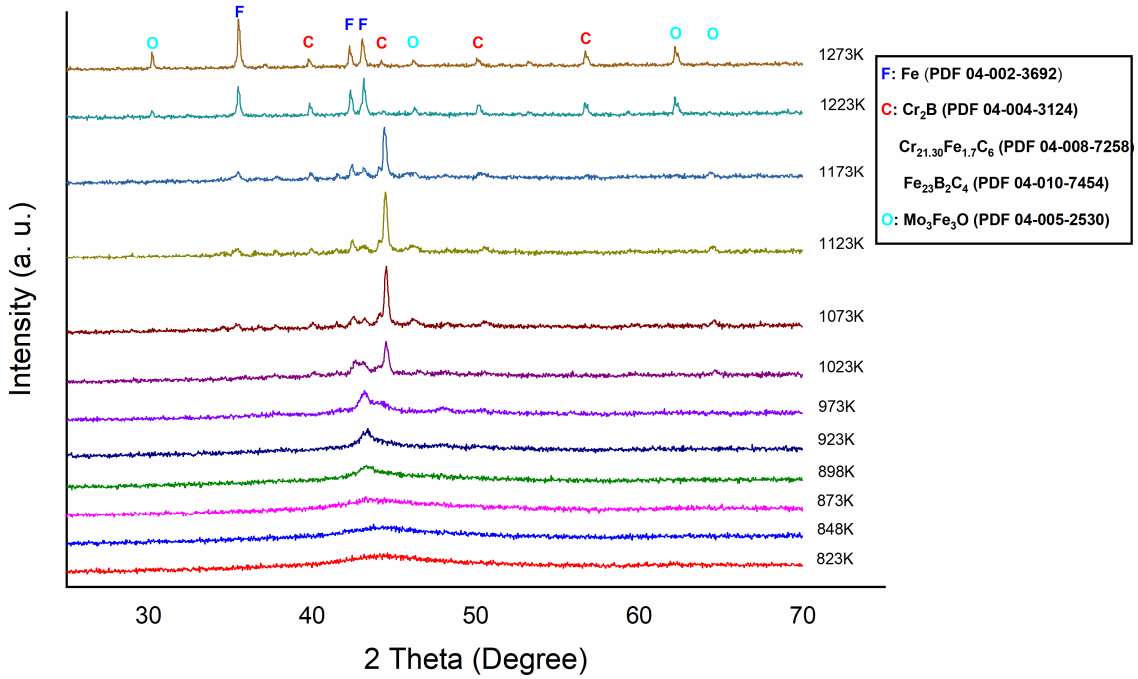

Figure 44. High temperature in situ X-ray diffraction patterns of amorphous SAM2×5 powders in the temperature range from 823 to 1273 K. The temperatures at which each pattern was obtained are (a) 823 K, (b) 848 K, (c) 873 K, (d) 898 K, (e) 923 K, (f) 973 K, (g) 1023 K, (h) 1073 K, (i) 1123 K, (j) 1173 K, (k) 1223 K, and (l) 1273 K.

In summary, an experimental DSC-based methodology using a non-isothermal approach was developed to determine the initial crystallization, change of crystallinity, and crystallinity percentage of an amorphous metallic alloy as a function of temperature. Regardless of devitrified phases, constituent elements and crystallization temperature range, this novel technique is capable of pinpointing the crystallinity percentage at an arbitrary temperature with a high accuracy. The only significant limitation is in a situation in which either an endothermic or exothermic thermal event takes place during the crystallization temperature range.

3. 2. Uncertainty Analysis

The uncertainty of the crystallinity percentage was calculated according to the Guide to the Expression of Uncertainty in Measurements (GUM) [278]. It should be noted that the uncertainty of the crystallinity percentage is a function of temperature. The reason is that, as will be discussed latter, some of the contributors to the uncertainty are temperature dependent. In the following part, we focus on obtaining the uncertainty of the crystallinity percentage at room temperature (initial crystallinity). However, the same procedure could be implemented for calculation of the uncertainty of the crystallinity percentage at any arbitrary temperature. We consider the three following assumptions: (i) crystallinity remains unchanged in the temperature region below 898 K, (ii) heating rate has been selected in such a way that crystallization takes place at temperatures between 898 K and 1208 K, and (iii) the crystallinity of all samples is assumed to be 100% when heated above 1208 K. Considering these assumptions, the initial crystallinity can be calculated as follows:

$$\text{Initial Crystallinity}\left(\%\right)=\left[1-\text{change of crystallinity}\left(\text{CC}\right)\text{ at }1208\text{ K}\right]\bullet 100 \tag{17}$$

Also, according to Equation (15), we have:

$$\text{CC}\left(1208\text{ K}\right)=\frac{h_{\text{crystalline}}\left(1208\text{ K}\right)-h_{\text{sample}}\left(1208\text{ K}\right)}{h_{\text{crystalline}}\left(1208\text{ K}\right)-h_{\text{amorphous}}\left(1208\text{ K}\right)} \tag{18}$$

Four contributors to the uncertainty of the crystallinity percentage can be identified: (i) repeatability, instrumental errors on the (ii) enthalpy of crystalline SAM2×5 at 1208 K, (iii) enthalpy of amorphous SAM2×5 at 1208 K, and (iv) enthalpy of test sample at 1208 K.

Errors in repeatability could be quantified by calculating the standard deviation of the crystallinity percentage for each sample using:

$$\mathrm{S} = \sqrt{\frac{\sum_{\mathrm{i}=1}^{n} \left(x_{\mathrm{i}} - \bar{x} \right)^2}{n-1}} \tag{19}$$

Where x_{i}, $\bar{x}$ and n represent the measured values, the average value of all the measurements, and the number of measurements, respectively. The resulting error values are shown as error bars in Figure 13. According to:

$$h\left(T\right) - h\left(898\ \mathrm{K}\right) = \int_{898\ \mathrm{K}}^{T} C_{\mathrm{p}}\left(T\right)\ \mathrm{dT} \cong \sum_{n} C_{\mathrm{p},n}\left(T_n\right) \cdot \Delta T \tag{20}$$

The enthalpy at any arbitrary temperature is a function of heat capacity as well as temperature. Thus, the following approach should be implemented in order to calculate the uncertainty in the enthalpy. When any arbitrary measured quantity Y is not measured directly, but is determined from N quantities X_1, X_2, . . ., X_N, we have:

$$\mathrm{Y} = f\left(\mathrm{X}_1, \mathrm{X}_2, \ldots, \mathrm{X}_\mathrm{N}\right) \tag{21}$$

The expectation of each X_i, where i denotes value 1, 2, . . . , N) is denoted by x_i. The standard uncertainty of y, where y is the estimate of the measured Y is obtained by appropriately combining the standard uncertainties of the input estimates $x_1, x_2, \ldots, x_N$. When the input quantities are correlated, the appropriate expression for the combined uncertainty $u(y)$ is:

$$u\left(y\right)=\sqrt{\sum_{i=1}^{N}\sum_{j=1}^{N}\frac{\partial f}{\partial x_i}\frac{\partial f}{\partial x_j}u\left(x_i,x_j\right)}=\sqrt{\sum_{i=1}^{N}\left(\frac{\partial f}{\partial x_i}\right)^2u^2\left(x_i\right)+2\sum_{i=1}^{N-1}\sum_{j=i+1}^{N}\frac{\partial f}{\partial x_i}\frac{\partial f}{\partial x_j}u\left(x_i,x_j\right)} \qquad (22)$$

Where x_i and x_j are the estimates of X_i and X_j and $u(x_i, x_j) = u(x_j, x_i)$ is the estimated covariance associated with x_i and x_j. The degree of correlation between x_i and x_j is characterized by the estimated correlation coefficient:

$$r\left(x_i,x_j\right)=\frac{u\left(x_i,x_j\right)}{u\left(x_i\right)\cdot u\left(x_j\right)} \qquad (23)$$

Where $r(x_i, x_j) = r(x_j, x_i)$ and $-1 \leq r(x_i, x_j) \leq 1$. If the estimates x_i and x_j are independent, then $r(x_i, x_j) = 0$, and a change in one does not imply an expected change in the other. From Equation (20), the uncertainty in the enthalpy is affected by the uncertainty of the temperature difference (ΔT) and of the heat capacity. Considering the three enthalpy parameters in Equation (18), we start by calculating the uncertainty of h_{cryst} (T = 1208 K) that, according to Equation (22), could be defined as follows:

$$u\left(h_{\text{cryst}}\left(1208\ \text{K}\right)\right)=\sqrt{\sum_{i=1}^{n}\left(\frac{\partial h\left(1208\ \text{K}\right)}{\partial x_{\text{i}}}\right)^{2}\cdot u\left(x_{i}\right)^{2}+2\sum_{i=1}^{n-1}\sum_{j=i+1}^{n}\left(\frac{\partial h\left(1208\ \text{K}\right)}{\partial x_{i}}\right)\left(\frac{\partial h\left(1208\ \text{K}\right)}{\partial x_{j}}\right)\cdot u\left(x_{i},x_{j}\right)} \tag{24}$$

Where n = 3, namely $C_{\text{p-crystalline\_sample}}$ (1208 K) = 0.5561 J/g (average value of all three measurements), $C_{\text{p-crystalline\_sample}}$ (898 K) = 0.35367 J/g (average value of all three measurements), and ΔT = 1208 - 898 = 310 K. Also, x_i and x_j represent different heat capacity values and $u(x_i)$ is the uncertainty from each input.

The heat capacity values of a specific sample at any two arbitrary temperatures, such as 898 K and 1208 K, are correlated input quantities. Consequently, correlation coefficients need to be considered and calculated. In this research, an online calculator [279] was used to obtain the correlation coefficients. By expanding Equation (24), we obtain:

$$u\left(h_{\text{cryst}}\left(T=1208\text{ K}\right)\right)=$$

$$=\left\{\begin{array}{l}\left(\dfrac{\partial h\left(1208\text{ K}\right)}{\partial C_{\text{p}}\left(898\text{ K}\right)}\right)^2\cdot u\left(C_{\text{p}}\left(898\text{ K}\right)\right)^2+\\ \quad+\left(\dfrac{\partial h\left(1208\text{ K}\right)}{\partial C_{\text{p}}\left(1208\text{ K}\right)}\right)^2\cdot u\left(C_{\text{p}}\left(1208\text{ K}\right)\right)^2+\\ \quad+\left(\dfrac{\partial h\left(1208\text{ K}\right)}{\partial \Delta T}\right)^2\cdot u\left(\Delta T\right)^2+\\ \quad+2\cdot\left[\begin{array}{l}\left(\dfrac{\partial h\left(1208\text{ K}\right)}{\partial C_{\text{p}}\left(898\text{ K}\right)}\right)\cdot\left(\dfrac{\partial h\left(1208\text{ K}\right)}{\partial C_{\text{p}}\left(1208\text{ K}\right)}\right)\cdot\\ r\left(C_{\text{p}}\left(898\text{ K}\right),C_{\text{p}}\left(1208\text{ K}\right)\right)\cdot\\ u\left(C_{\text{p}}\left(898\text{ K}\right)\right)\cdot u\left(C_{\text{p}}\left(1208\text{ K}\right)\right)+\\ \left(\dfrac{\partial h\left(1208\text{ K}\right)}{\partial C_{\text{p}}\left(898\text{ K}\right)}\right)\cdot\left(\dfrac{\partial h\left(1208\text{ K}\right)}{\partial \Delta T}\right)\cdot\\ r\left(C_{\text{p}}\left(898\text{ K}\right),\Delta T\right)\cdot u\left(C_{\text{p}}\left(898\text{ K}\right)\right)\cdot u\left(\Delta T\right)+\\ \left(\dfrac{\partial h\left(1208\text{ K}\right)}{\partial C_{\text{p}}\left(1208\text{ K}\right)}\right)\cdot\left(\dfrac{\partial h\left(1208\text{ K}\right)}{\partial \Delta T}\right)\cdot\\ r\left(C_{\text{p}}\left(1208\text{ K}\right),\Delta T\right)\cdot u\left(C_{\text{p}}\left(1208\text{ K}\right)\right)\cdot u\left(\Delta T\right)\end{array}\right]\end{array}\right\}^{\frac{1}{2}} \tag{25}$$

In order to calculate the uncertainty of heat capacity at 898 K, $u\left(C_{\text{p}}\left(898\text{ K}\right)\right)$, and 1208 K, $u\left(C_{\text{p}}\left(1208\text{ K}\right)\right)$, instead of calculating the standard deviation, the difference between the maximum and minimum values of heat capacity at 898 K and 1208 K are considered. This is for the purpose of incorporating larger values of the uncertainty of the heat capacity, which yields a larger safety factor for the total uncertainty. The uncertainty of the temperature difference (ΔT) of 1 K (based on information from TA Instruments), is an expanded uncertainty with a coverage

factor of 2. Since the heat capacities at 898 K and 1208 K are independent of the temperature difference (ΔT) the corresponding correlation coefficients, $r\left(C_{\mathrm{p}}\left(898\ \mathrm{K}\right)\right)$ and $r\left(C_{\mathrm{p}}\left(1208\ \mathrm{K}\right)\right)$ are zero, meaning that the last two terms in the bracket in Equation (25) equal to zero. However, from the online calculator, the correlation coefficient between heat capacities was calculated to be 0.92576. Consequently, by inserting the corresponding values into Equation (25) we obtain:

$$u\left(h_{\mathrm{cryst}}\left(T=1208\ \mathrm{K}\right)\right)=$$

$$=\left\{\begin{array}{l}\left(\Delta T\right)^2\cdot u\left(C_{\mathrm{p}}\left(898\ \mathrm{K}\right)\right)^2+\left(\Delta T\right)^2\cdot u\left(C_{\mathrm{p}}\left(1208\ \mathrm{K}\right)\right)^2+\\ \quad+\left(C_{\mathrm{p}}\left(898\ \mathrm{K}\right)+C_{\mathrm{p}}\left(1208\ \mathrm{K}\right)\right)^2\cdot u\left(\Delta T\right)^2+\\ \quad+2\left[\begin{array}{l}\left(\Delta T\right)^2\cdot r\left(C_{\mathrm{p}}\left(898\ \mathrm{K}\right),C_{\mathrm{p}}\left(1208\ \mathrm{K}\right)\right)\cdot\\ u\left(C_{\mathrm{p}}\left(898\ \mathrm{K}\right)\right)\cdot u\left(C_{\mathrm{p}}\left(1208\ \mathrm{K}\right)\right)\end{array}\right]\end{array}\right\}^{\frac{1}{2}}= \qquad (26)$$

$$=\left\{\begin{array}{l}\left(310\right)^2\cdot\left(0.1878\right)^2+\left(310\right)^2\cdot\left(0.3118\right)^2+\\ \quad+\left(0.5661+0.35367\right)^2\cdot\left(0.05\right)^2+\\ \quad+2\left[\left(310\right)^2\cdot\left(0.92576\right)\cdot\left(0.1878\right)\cdot\left(0.3118\right)\right]\end{array}\right\}^{\frac{1}{2}}=152.15\ \mathrm{J/g}$$

Similarly, $u\left(h_{\mathrm{amorphous}}\left(\mathrm{T}=1208\ \mathrm{K}\right)\right)$ was calculated and resulted in a value of 91.21 J/g. The same procedure was repeated for SAM5% and $u\left(h_{\mathrm{SAM5\%}}\left(\mathrm{T}=1208\ \mathrm{K}\right)\right)$ was found to be 69.14 J/g. According to GUM, uncertainty contributions must all be in the same units of measurement before they can be combined. In order to do that, sensitivity coefficients for each contributor to uncertainty need to be calculated. Generally, sensitivity coefficients are just a

multiplier used to convert the uncertainty components to the correct units and magnitude for uncertainty analysis. A sensitivity coefficient for each input was separately calculated by obtaining the derivative of Equation (18) with respect to the input. Thus, the sensitivity coefficients are:

$$\mathrm{SC}\left[h_{\mathrm{crystalline}}\left(T=1208\ \mathrm{K}\right)\right]=\frac{\partial \mathrm{CC}\left(1208\ \mathrm{K}\right)}{\partial h_{\mathrm{crystalline}}\left(T=1208\ \mathrm{K}\right)}= \\ =\frac{h_{\mathrm{SAM5\%}}\left(T=1208\ \mathrm{K}\right)-h_{\mathrm{amorphous}}\left(T=1208\ \mathrm{K}\right)}{\left[h_{\mathrm{crystalline}}\left(T=1208\ \mathrm{K}\right)-h_{\mathrm{amorphous}}\left(T=1208\ \mathrm{K}\right)\right]^2} \tag{27}$$

$$\mathrm{SC}\left[h_{\mathrm{SAM5\%}}\left(T=1208\ \mathrm{K}\right)\right]=\frac{\partial \mathrm{CC}\left(1208\ \mathrm{K}\right)}{\partial h_{\mathrm{SAM5\%}}\left(T=1208\ \mathrm{K}\right)}= \\ =\frac{1}{h_{\mathrm{amorphous}}\left(T=1208\ \mathrm{K}\right)-h_{\mathrm{crystalline}}\left(T=1208\ \mathrm{K}\right)} \tag{28}$$

$$\mathrm{SC}\left[h_{\mathrm{amorphous}}\left(T=1208\ \mathrm{K}\right)\right]=\frac{\partial \mathrm{CC}\left(1208\ \mathrm{K}\right)}{\partial h_{\mathrm{amorphous}}\left(T=1208\ \mathrm{K}\right)}= \\ =\frac{h_{\mathrm{crystalline}}\left(T=1208\ \mathrm{K}\right)-h_{\mathrm{SAM5\%}}\left(T=1208\ \mathrm{K}\right)}{\left[h_{\mathrm{crystalline}}\left(T=1208\ \mathrm{K}\right)-h_{\mathrm{amorphous}}\left(T=1208\ \mathrm{K}\right)\right]^2} \tag{29}$$

Considering the average values for $h_{\mathrm{crystalline}}\left(T=1208\ \mathrm{K}\right)$, $h_{\mathrm{SAM5\%}}\left(T=1208\ \mathrm{K}\right)$ and $h_{\mathrm{amorphous}}\left(T=1208\ \mathrm{K}\right)$ of 344.47, 119.68 and 125.97, respectively, the sensitivity coefficient for each enthalpy factor can be calculated. Since the units of repeatability and enthalpy are similar, the sensitivity coefficient for repeatability is assumed to be 1. Contributors to uncertainty and sensitivity coefficients have been listed in Table 3.

Table 3. Uncertainty and sensitivity coefficients.

Uncertainty source	Uncertainty	Units	Sensitivity coefficient
Repeatability	1.15	wt.%	1
$h_{\text{crystalline}}\left(T = 1208\ \text{K}\right)$	152.15	J/g	-0.000129236
$h_{\text{amorphous}}\left(T = 1208\ \text{K}\right)$	91.21	J/g	0.004705895
$h_{\text{SAM5\%}}\left(T = 1208\ \text{K}\right)$	69.14	J/g	-0.004576659

Finally, in order to combine the contributions, the following Equation was used:

$$u_c = \sqrt{\sum_i c_i^2 u_i^2} \tag{30}$$

Where u_c, c_i^2 and u_i^2 are the total (combined uncertainty), sensitivity coefficient for factor i and uncertainty regarding factor i, respectively. Using Equation (30) and data in Table 3, the uncertainty of the crystallinity percent of a powder mixture with a known crystallinity of 5% is 1.57%. Table 4 summarizes the standard deviation (error bars in Figure 42), as well as uncertainty values for examined powder mixtures. Aside from the sources of uncertainty contributing to the calculated crystallinity, it should be noted that the process of preparing calibration samples with known crystallinity also contributes to the error.

Table 4. Uncertainties of sample weighting and repeatability, combined uncertainties, and rounded combined uncertainties for calibration samples with different crystallinity percentages.

Sample	Uncertainty of sample weighting	Uncertainty of repeatability	Combined uncertainty	Rounded combined uncertainty
SAM5%	0.28	0.1	[(0.28)^2+(0.1)^2]^0.5 = 0.297	0.30
SAM20%	0.28	0.1	[(0.28)^2+(0.1)^2]^0.5 = 0.297	0.30
SAM40%	0.28	0.2	[(0.28)^2+(0.2)^2]^0.5 = 0.3440	0.30
SAM60%	0.28	0.1	[(0.28)^2+(0.1)^2]^0.5 = 0.297	0.30
SAM80%	0.28	0.1	[(0.28)^2+(0.1)^2]^0.5 = 0.297	0.30

Two main contributors to the uncertainty of crystallinity of calibration samples include (i) measuring the weight of powder samples, and (ii) repeatability. For preparing calibration samples (contributor i), appropriate amounts of crystalline and amorphous SAM2×5 were weighted with a repeatability of 0.2 g (provided by the manufacturer of the scale). Since two mass measurements were carried out for preparing each calibration sample, the theoretical uncertainty would be

$$\sqrt{\left(0.2\ \text{g}\right)^2+\left(0.2\ \text{g}\right)^2}=0.28\ \text{g}.$$

For each crystallinity percentage, three powder mixtures were independently prepared and tested, thus the contribution of repeatability could be quantified in the form of a standard deviation presented in the last column of Table 2 (contributor ii). As mentioned earlier, the sensitivity coefficient for these two types of repeatability equals to 1. Hence, using Equation (30), the rounded combined uncertainty for the crystallinity percentage of each prepared powder mixture is calculated and presented in Table 4. The uncertainty values associated with crystallinity of

calibration samples raised from experiments and calculation, in addition to Table 4, are also shown as error bars along Y- and X-axis, respectively in Figure 42. Table 5 summarizes the true and calculated crystallinities and corresponding uncertainties for all calibration specimens.

Table 5. Calculated crystallinity, standard deviation and uncertainty for powder mixtures with known crystallinity percentages. It should be noted that the values following the average crystallinity in the last column of Table 1 include the standard deviation. The errors in the initial crystallinity in this table are uncertainty values that include the standard deviation obtained from three independent measurements as well as errors originating from multiple sources explained in the manuscript.

Sample	Experiments		Calculation	
	True crystallinity (wt. %)	Uncertainty (wt. %)	Calculated crystallinity from DSC data (wt. %)	Uncertainty (wt. %)
SAM5%	5.1	0.3	3.0	1.6
SAM20%	20.0	0.3	20.0	2.5
SAM40%	40.0	0.3	42.0	1.5
SAM60%	60.0	0.3	61.0	1.8
SAM80%	80.0	0.3	82.0	1.9

It is clearly seen that for all concentrations of crystalline phase in the calibration samples, the calculated crystallinity is very close to the true one. This high accuracy is even observed for the sample with an extreme composition (dilute SAM5%). It is worth mentioning that ideally assumed amorphous samples might include some small percentage of crystalline phase, whereas the crystalline samples might include some small percentage of amorphous component. This would need to be quantified and added to the uncertainty associated with the preparation of calibration samples.

3. 3. Characterization of spark plasma sintered specimens

3. 3. 1. Structural characterization

Bulk samples were prepared by spark plasma sintering of amorphous powder at different temperatures ranging from 888K to 948K. Contrary to many other researches where mechanical properties have been expressed as a function of sintering temperature, in this report, instead of temperature, we explore how crystallinity percentage would affect the mechanical responses of sintered specimens. The reason is that, even by applying the same SPS temperature, different thermal properties of graphite utensils in various SPS machines can cause diverse crystallinity percentages in sintered samples which will result in different mechanical behaviors. However, it is not easy to quantify the crystallinity percentage in devitrified SAM system because of the following reasons. Firstly, SAM with a chemical composition of $Fe_{49.7}Cr_{17.7}Mn_{1.9}Mo_{7.4}W_{1.6}B_{15.2}C_{3.8}Si_{2.4}$ contains about 20 at. % of light weight elements like B and C which makes XRD an ineffective technique to characterize it. This limitation is expected since the resolution of the XRD technique is about 5 wt.% for specimens without light-weight elements such as carbon and boron [277]. Secondly, as will be discussed later, the products of crystallization process in SAM system could not be precisely identified which is due to existence of eight elements in its chemical composition and consequently the formation of different phases whose diffraction peaks overlap in XRD diffractogram. In our previous paper [280], we introduced a new DSC-based methodology to quantify the crystallinity percentage in amorphous systems which is independent from the chemical composite of products of crystallization, is not sensitive to the existence of light weight elements, and has an accuracy as low as 5%. According to this technique, by calculating the difference between the heat flow of an empty alumina pan and the same pan loaded with sintered sample and dividing the difference by the heating rate and mass of sample, the apparent heat capacity (C_p) as a function of temperature would be obtained. The same

procedure needs to be repeated for fully amorphous and crystalline SAM powders as well. The typical Cp curves obtained for amorphous, crystalline SAM powders, and bulk SAM sintered at 888K are shown in Figure 45(a). Integration of the apparent heat capacity curves, yield variation of enthalpy for each sample which needs to be corrected for structural relaxation (Figure 45(b)). Then, the change of crystallinity (CC) as a function of temperature (Figure 45(c)) could be calculated using the following Equation:

$$\mathrm{CC}(T) = \frac{H_{\text{crystalline}}(T) - H_{\text{SAMX\%}}(T)}{H_{\text{crystalline}}(T_{\max}) - H_{\text{amorphous}}(T_{\max})} \tag{31}$$

The initial crystallinity of sintered SAM powder at 888K would be the difference between crystallinity change of the amorphous SAM powder and sintered specimen at maximum temperature which is 5%. Moreover, by adding the initial crystallinity value (5%) to the crystallinity change curve of sintered specimen, variation of crystallinity percentage as a function of temperature can be obtained which pinpoints the crystallinity percentage at any arbitrary temperature [Figure 45(d)]. For the case of the sintered SAM powder at 888K, the sample has an initial crystallinity of 5%. By increasing the temperature to about 1173K, the crystallinity percentage gradually increases and reaches 100%. Further increase in temperature does not change the crystallinity, as evidenced by the flattening of the curve in Figure 45(d).

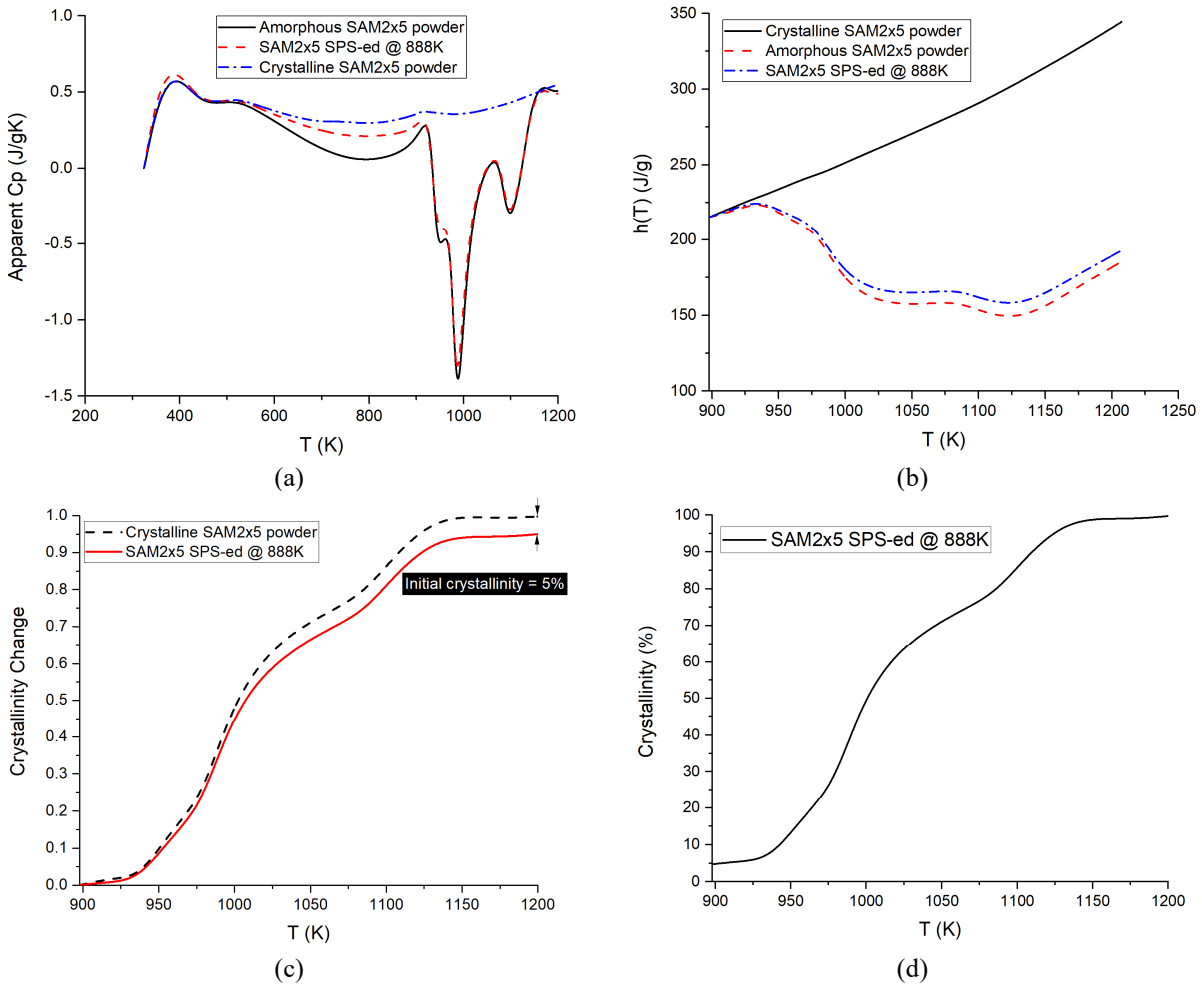

Figure 45. Variation of (a) apparent heat capacity, (b) enthalpy, (c) crystallinity change, and (d) crystallinity percentage as a function of temperature for amorphous, crystalline SAM powders, and bulk SAM sintered at 888K.

This procedure was repeated three times for every sintered specimen and the average value of initial crystallinity is shown in Figure 46.

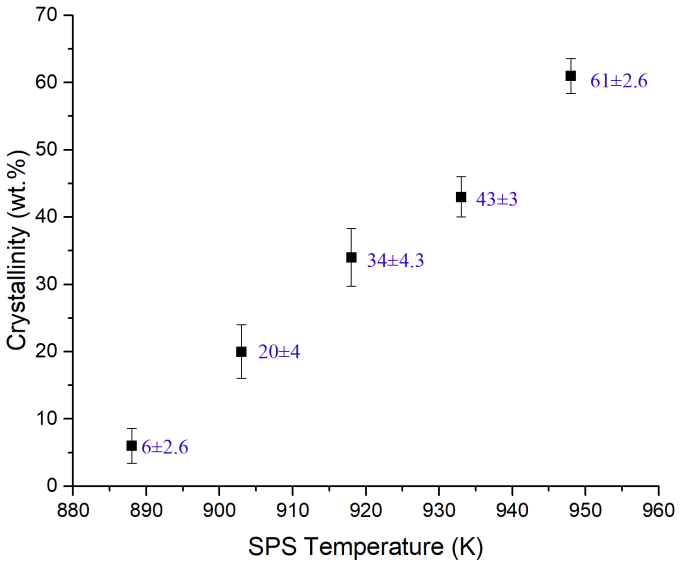

Figure 46. Variation of crystallinity percentage of bulk SAM samples as a function of SPS temperature.

Lowest sintering temperature yields a crystallinity of about 6%, while by increasing the temperature to 948K, the crystallinity increases to about 61% crystalline.

According to Figure 47, which shows the XRD patterns of samples sintered at different temperatures, the lowest sintering temperature (888K) provides an almost amorphous sample in which no sign of crystallization was captured using even small-step-size, long XRD runs. However, as was discussed before, DSC methodology shows that this sample contains about 6% of crystallinity. By increasing the sintering temperature, the amorphous hump starts to split, and BCC-Fe began to crystallize. At maximum SPS temperature (948K), along with BCC-structured Fe, carbides/borides devitrify as well.

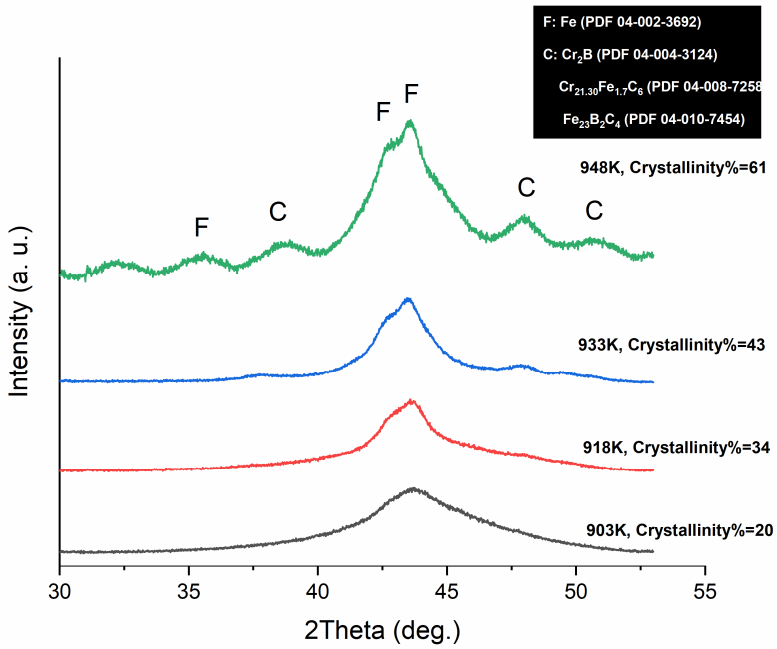

Figure 47. XRD patterns of SAM2×5-Dev specimens sintered at different temperatures ranging from 903 to 948 K.

SEM micrographs (Figure 48) of the polished cross sections show that grain boundaries are discernible for all samples [arrows in Figure 48(a)]. In addition to grain boundaries, the bulk samples contain different percentages of porosity. Some of these pores are marked with arrows in Figure 48 (b). Even at the maximum sintering temperature [Figure 48 (d)], minimal sub-micron and micrometer-sized pores are noted. SEM images were analyzed using ImageJ software to obtain the percent porosity. Specimens with crystallinity percentage of 20, 34, 43 and 61contain porosity percentage of 0.62 ± 0.08%, 0.57 ± 0.1%, 0.39 ± 0.05%, and 0.15 ± 0.06%, respectively. The results indicate that increasing the sintering temperature does not significantly increase the compaction and all specimens contain almost the same percentage of porosity.

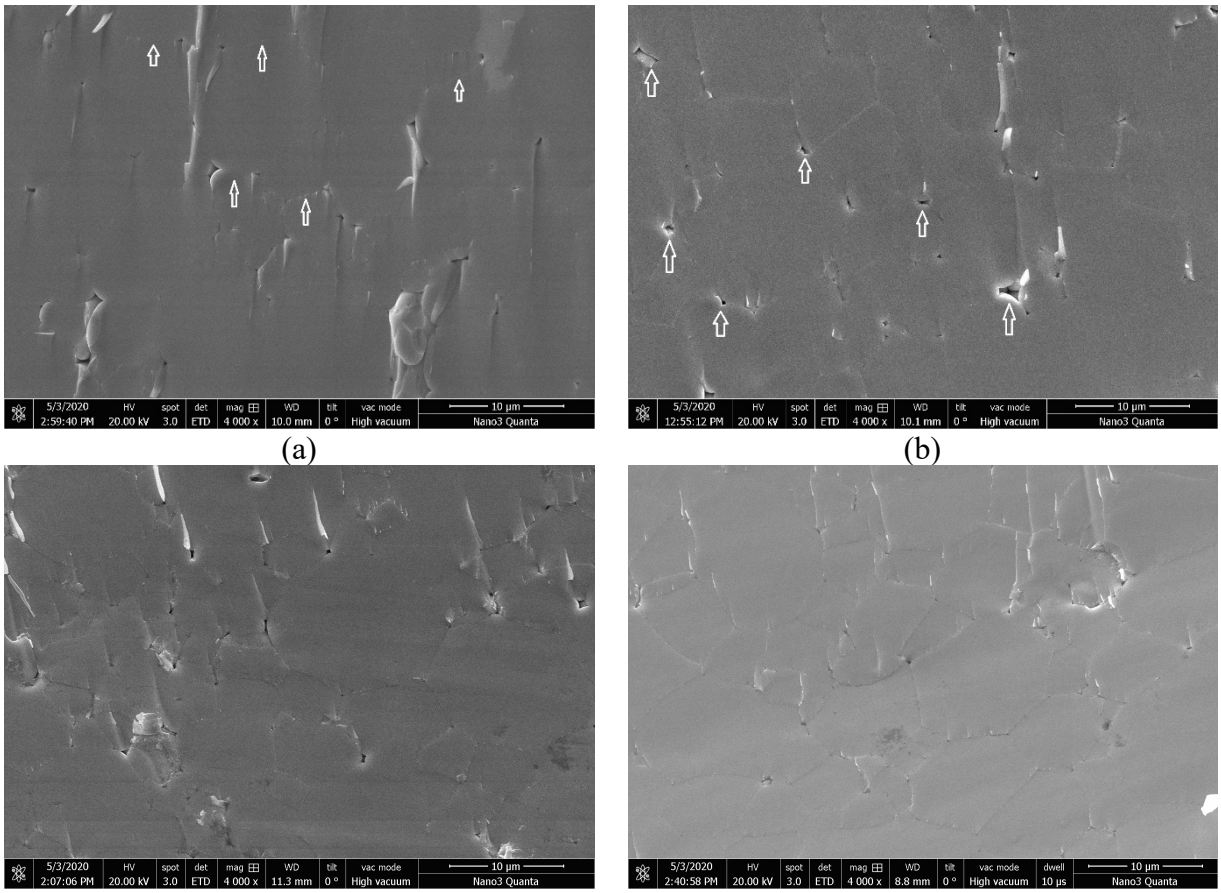

Figure 48. SEM micrographs of polished surfaces for the SAM2×5-Dev samples sintered at (a) 903 K, (b) 918 K, (c) 933 K, and (d) 948 K. Arrows in (a) and (b) point to some of the boundaries between sintered particles and pores, respectively. The porosity percentage of each specimen obtained from SEM image analysis indicates (a) 0.62 ± 0.08%, (b) 0.57 ± 0.1%, (c) 0.39 ± 0.05%, and (d) 0.15 ± 0.06% porosities.

High-resolution transmission electron microscopy (HR-TEM) was utilized to analyze the microstructure of composite samples after sintering. Figure 49 shows TEM images of specimen SPS-ed at 903K. According to the selected area diffraction pattern shown in the inset, sintered samples consist of an amorphous matrix (Figure 49(a)) in which nanocrystals with a size smaller than 20nm are homogeneously dispersed (Figure 49(b)). Figure 49(c) shows three crystalline domains in which the crystalline planes are clearly discernible in the insets.

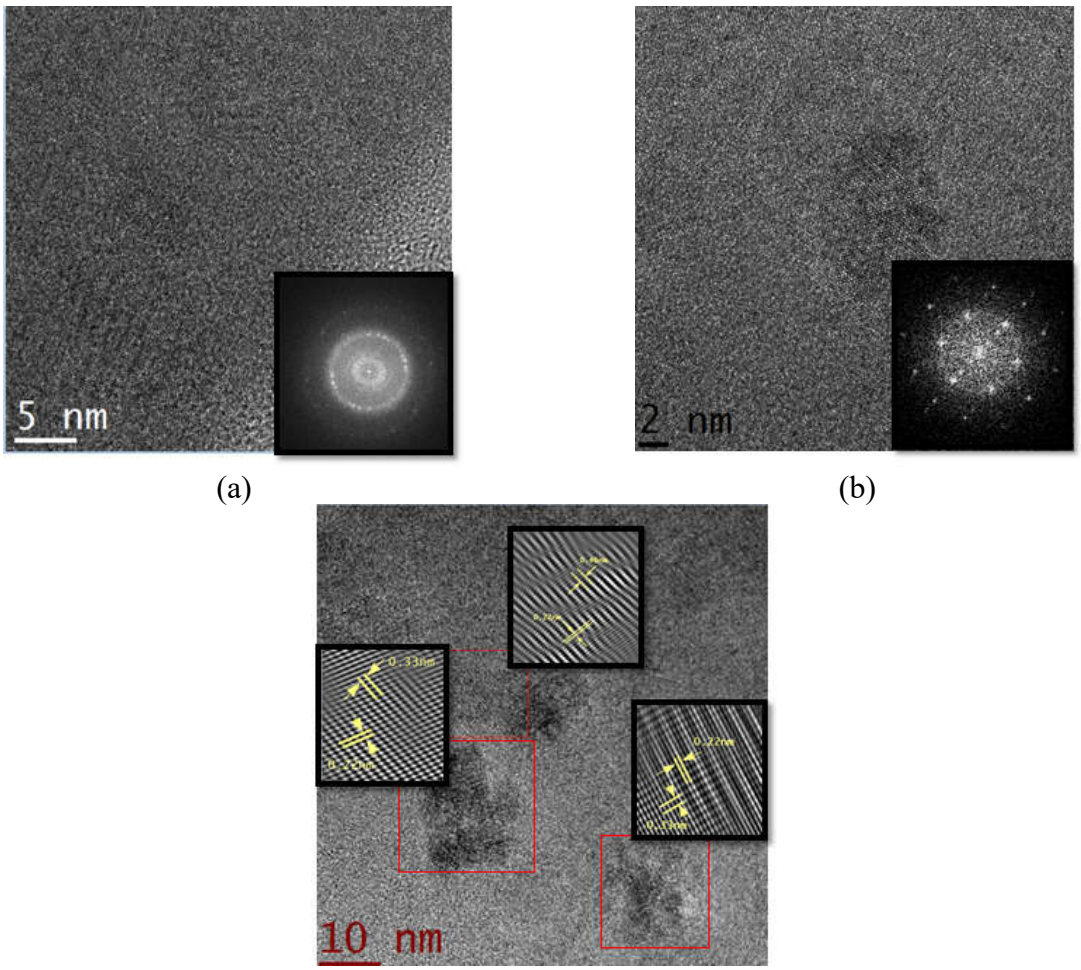

(a) (b) (c)

Figure 49. HR-TEM images from the polished surface of SAM2x5 powder sintered at (a) 888K, (b) 903K, (c) 918K, (d) 933K, and (e) 948K.

Densities of sintered samples were measured via Archimedes methodology and the results are graphed in relation to crystallinity in Figure 50. The two samples with crystallinity percentages of 43 and 61%, have almost the same density, exceeding the theoretical density of 7.75 g/cm^3 for fully amorphous SAM2×5 [281]. This happens because during the crystallization process, heavier carbide and boride phases form which push the density of sintered samples beyond the theoretical one.

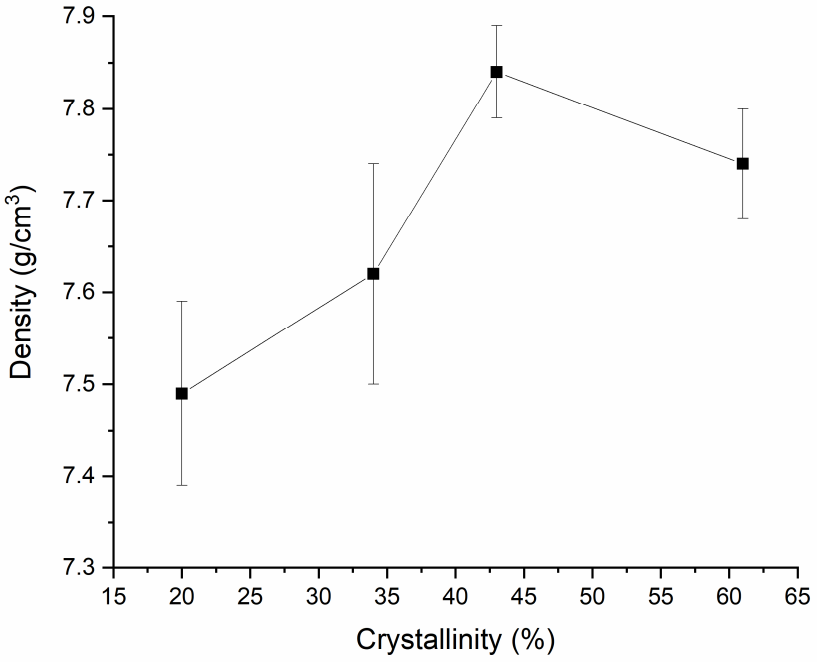

Figure 50. Variation of density for the SAM2×5 sintered specimens with respect to crystallinity percentage.

3. 3. 2. Mechanical properties

3. 3. 2. 1. Hardness and Toughness

Vickers hardness of the specimens requires the selection of an appropriate load when testing metallic glasses. Above a critical load, the initiation and propagation of cracks act as a supplementary dissipative mechanism along with shear band formation, which can lower the hardness [282]. According to Figure 51(a), there is an increase in micro-hardness with increasing the crystallinity, which can be mainly attributed to the annihilation of free volume through a structural relaxation process [282]. It has been shown that upon heating an amorphous material and during the relaxation process, rearrangement of atoms can take place that leads to enhanced packing and a decrease in the interatomic distance. This leads to strengthening of the bonds, which prevents the formation of shear bands, increases the resistance against the penetration of an

indenter, and consequently improves the hardness [283-285]. The content of free volume in a fully/partially amorphous sample can be qualitatively evaluated by means of DSC. The reduction of free volume upon heating is an exothermic thermal event which can be identified in the DSC thermogram as an exothermic peak preceding the glass transition temperature. The higher the content of free volume, the deeper the exothermic peak. Figure 51 (b) presents the change of apparent heat capacity as a function of temperature for all sintered specimens. The relaxation enthalpy which equals the area under the C_p curve, was calculated from 515 K (where the relaxation process starts) to 883 K (T_g). The enthalpy values are shown in Figure 51 (b).

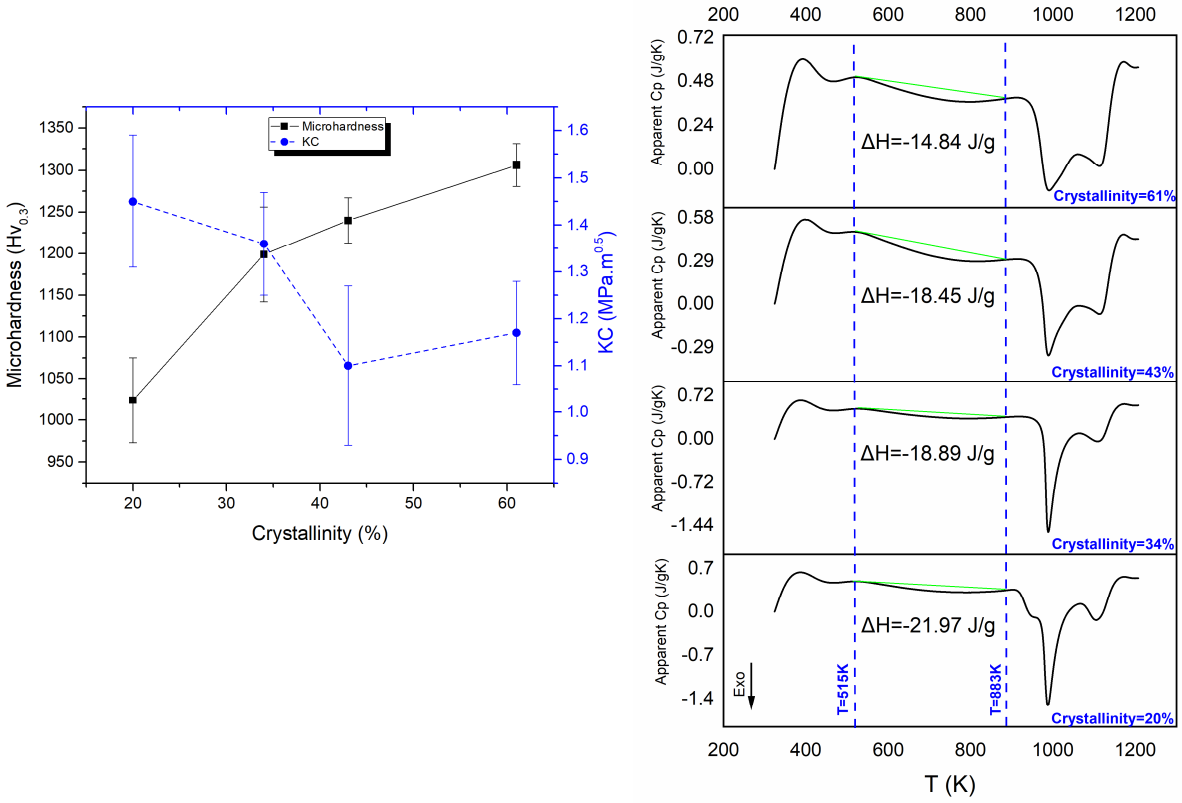

(a) (b)

Figure 51. (a) Variation of microhardness and indentation toughness of the specimens versus crystallinity percentage. (b) C_p curves of the specimens showing the exothermic peak associated with the structural relaxation process.

As the crystallinity percentage increases, the relaxation enthalpy decreases indicating that the exothermic reaction preceding the glass transition temperature is attenuated. Thus, by increasing the sintering temperature, the content of free volume decreases and the crystallinity increases. As explained previously, the process of reduction of free volume in a fully/partially amorphous sample increases the strength of atomic bonds, which leads to an enhancement of hardness.

Bulk metallic glasses generally benefit from high strength and elasticity [1, 83], whereas their fracture toughness values vary significantly from highly brittle to exceptionally tough [286, 287]. In fact, precise measurements and evaluation of BMG fracture toughness has proven challenging [288]. For instance, toughness values between 16 and 130 $MPa \bullet m^{0.5}$ have been reported for $Zr_{41.2}Ti_{12.5}Cu_{10}Ni_{10}Be_{22.5}$ [289-293], a significant scatter that merits further consideration. It has been proposed that the large scatter arises from the variety of sample geometries or loading modes [294-298], as well as complexities in the specimen preparation, such as difficulties in fabricating precise notches or pre-cracks, different cooling rates, casting defects, and compositional fluctuations during devitrification [288, 293]. The two most widely used methodologies for measuring the fracture toughness of Fe-based BMGs are notch fracture toughness and indentation fracture toughness. Notch fracture toughness is influenced by the elastic properties, porosity (location, size and type), inclusions, precipitate phases, cooling rate, and residual stress [288, 299]. On the other hand, indentation fracture toughness provides a prompt estimation of fracture toughness without the need for extensive fracture mechanical testing and expensive sample preparation [88, 299].

However, in indentation fracture toughness, the applied load should be optimized in such a way that it causes cracks to form at the corners of the indent. In this case, the indentation

toughness (K_c) could be extracted from the length of the cracks. The calculation of K_c depends on the crack geometry. When the corner cracks are visible at the free surface, they can be either half penny median-radial cracks [300] or Palmquist radial cracks [301]. When c/a>2.5, the crack is considered to have a half penny median-radial geometry, while Palmquist radial cracks is considered when c/a<2.5 [302, 303], where c (half length of the half penny crack) is the sum of the corner crack length (l) and indent half diagonal length (a). For a half penny median crack, K_c is expressed by Eq. (27) which obeys the Lawn–Evans–Marshall model and has been developed for measurement of fracture toughness of ceramics [300, 304]. In Equation 2, δ is a constant for the standard Vickers diamond indenter, E is Young's modulus, H is the hardness, P is the applied indentation load where cracks are observed, and d is a nondimensional constant that is primarily a function of indenter geometry. For radial or Palmquist radial cracks, K_c is determined by Equation (33). ϕ is the constraint factor, which is around 3 (obtained by curve fitting) [187, 305, 306].

$$K_c = \delta\left(\frac{E}{H}\right)^2 \frac{P}{c^{1.5}} \qquad \text{for c/a>2.5} \qquad (32)$$

$$K_c = 0.035 \frac{H\sqrt{a}}{\emptyset} \left(\frac{E\emptyset}{H}\right)^{0.4} \left(\frac{l}{a}\right)^{-0.5} \qquad \text{for c/a<2.5} \qquad (33)$$

In order to calculate the fracture toughness of our samples from Vickers indentation, the applied load was increased from 300 gf to 1 kgf to form cracks at the corners of the indents and the Palmquist radial model was used [Equation (33)]. Maximum measured toughness, corresponding to the specimen with the smallest percent crystallinity, is around 1.6 MPa•$m^{0.5}$ (Figure 51(b)). As the crystallinity increased, the fracture toughness decreased slightly to a value of approximately 1.2 MPa•$m^{0.5}$. This can be attributed to the reduction in free volume. As

mentioned previously, a shorter interatomic distance results in a higher bond strength, which hinders the formation of multiple shear bands and reduces the toughness [88, 283, 285].

3. 3. 2. 2. Macro-compression Testing

In order to study the compressive response of sintered SAM samples, they were strained under a deformation rate of 10^{-3} s^{-1}. The engineering stress-strain curves for all samples are shown in Figure 52(a). None of the specimens shows plastic deformation, however a significant elastic deformation of at least 8% was recorded. Figure 52(b) shows the yield strength and Young's modulus values.

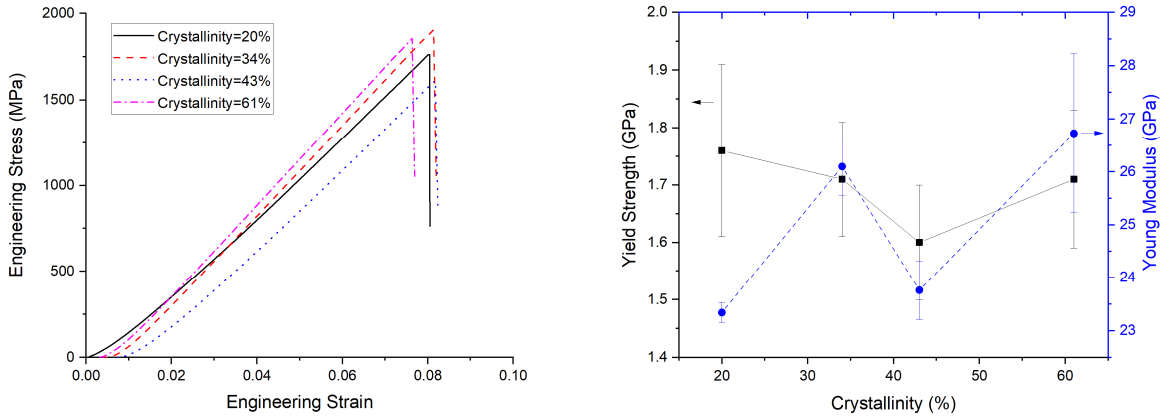

Figure 52. (a) Engineering compressive stress-strain curves, and (b) yield strength and Young's modulus with respect to crystallinity percentage for all specimens.

In BMGs, the initiation and propagation of shear upon fracture result in a unique fracture surface pattern [1, 307] that indicates the activation of very local sources of ductility whose contribution to improvement of ductility depends on their extension [308]. Post-compression SEM analysis was carried out on fracture surfaces to study their failure mechanism (Figure 53).

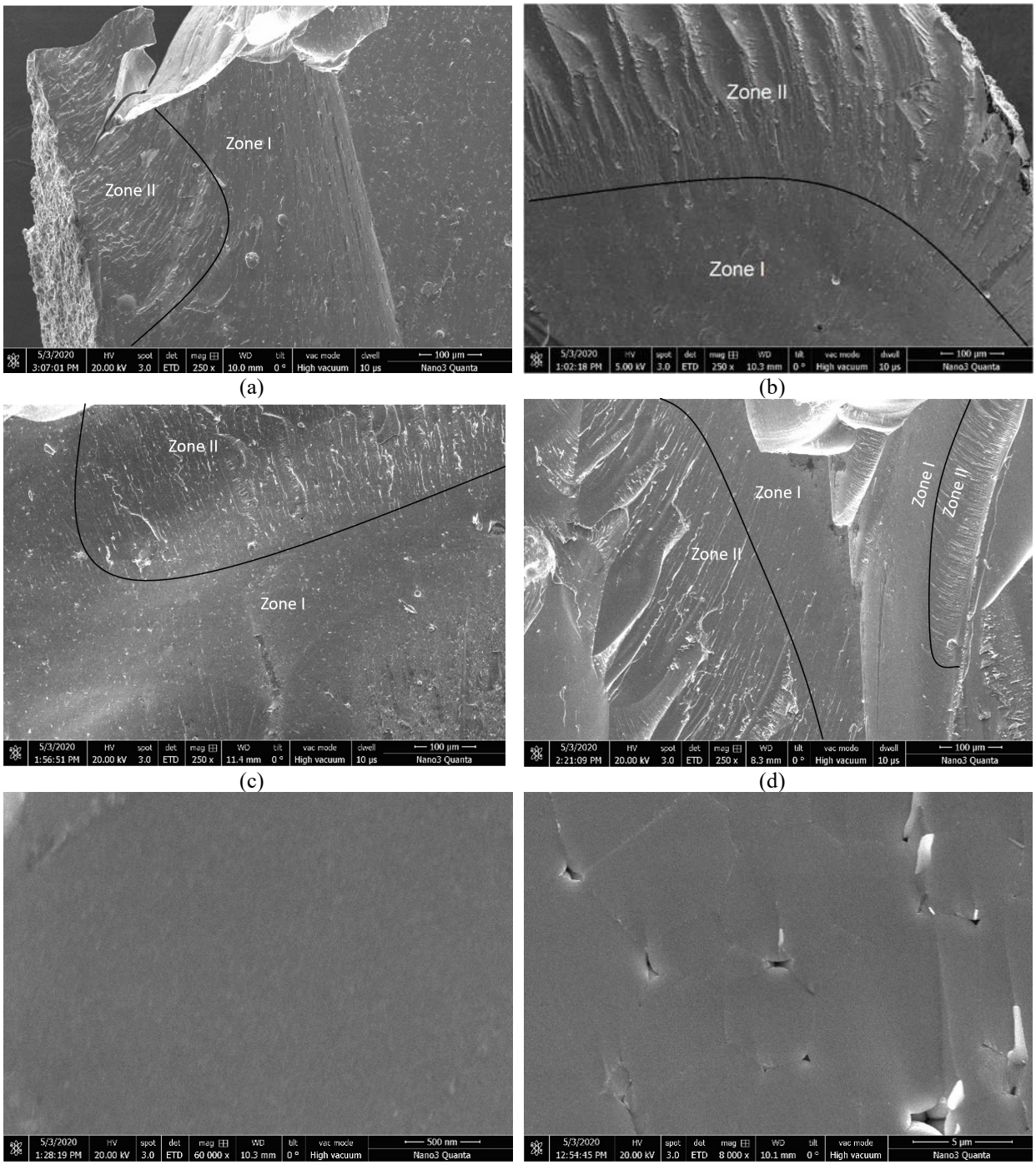

(a) (b) (c) (d) (e) (f)

Figure 53. Post compression fracture surface scanning electron micrographs of specimens with different crystallinity percentages of (a) 20%, (b) 34%, (c) 43%, and (d) 61%. (e) Higher magnification scanning electron micrographs from Zone I of (b), and (f) porosity from the same Zone in (b).

Figure 53 (a)-(d) represent the fracture surfaces of specimens with crystallinities of 20%, 34%, 43% and 61%, respectively. Regardless of the percentage of crystallinity, all sintered

samples exhibit the same fracture features. The fracture surfaces consist of two regions, a mirror zone [zone I in Figure 53(b)] and a shear band branching zone [zone II in Figure 53(b)]. Micrographs show that the extent of each of these zones on the fracture surface is almost the same. Zone II includes branch-like, massive shear bands indicating localized softening and shear instability [70]. A higher magnification scanning electron micrograph from zone I [Figure 53(e)] shows that this area is featureless even at the nanoscale. However, some pores with a wide range of sizes spanning from sub-micron to micrometers exist in both zones [Figure 53(f)]. On the other hand, fractography of bulk metallic glasses with some extent of ductility such as Ce-based ($K_C \sim$ 10 MPa•$m^{0.5}$) and Ti-based ($K_C \sim$ 50 MPa•$m^{0.5}$) BMGs show that their fracture surfaces consist of massive shear bands and mirror zones in which micro-voids are formed [308]. In the case of SAM2×5-Dev, the latter feature was not found in the mirror zone. It has been postulated that stress concentrations at crack tips might be enough to generate plasticity in the material at the vicinity of the crack tip, resulting in micro-void growth in these regions [308-310]. In brittle bulk metallic glasses, this local plasticity does not significantly contribute to the global toughness since it is extremely localized and the crack tip opening displacement (CTOD) needed to provide this plasticity is also very small. This situation leads to a low toughness that scales with CTOD. Tough bulk metallic glasses show a larger scale of local plasticity along with extensive crack bifurcation and branching, which consequently leads to a significantly higher CTOP and hence toughness enhancement [308]. It has also been postulated that the formation of damage micro-voids is independent of the chemical composition of bulk metallic glasses and is mainly associated with the glassy structure, which contains an amount of free volume and inherent atomic density fluctuations at the nanometer scale [311].

A correlation between the size of the plastic zone, fracture toughness and strength of BMGs is described by:

$$R_{\mathrm{p}} = \frac{1}{6\pi}\left(\frac{K_{\mathrm{c}}}{\sigma_{\mathrm{y}}}\right)^2 \tag{34}$$

Where R_{p} is radius of the plastic zone in the plain strain mode [312]. To determine the size of the plastic zones for our specimens, fracture toughness and yield strength values for each sample were extracted from Figure 51(a) and Figure 52(b), respectively. The specimens with crystallinity percentages of 20, 34, 43 and 61%, have plastic zones with radii of 20, 34, 25 and 25 nm, respectively.

Table 6 shows a summary of the fracture toughness, yield strength, size of plastic zone (measured and calculated) for some BMGs of a variety of chemical compositions.

Table 6. Measured and calculated length of plastic zone (R_{p}), fracture toughness, and yield strength values for a variety of bulk metallic glasses.

Chemical composition	Measured R_{p} (μm)	K_{C} (MPa•m$^{0.5}$)	σ_{y} (GPa)	Calculated R_{p} (μm)	Reference
$Zr_{41}Ti_{14}Cu_{12.5}Ni_{10}Be_{22.5}$	60	86	1.8	57.1	[290]
$Cu_{60}Zr_{20}Hf_{20}Ti_{10}$	35	67	1.7	38.8	[307]
$Ti_{50}Ni_{24}Cu_{20}B_1Si_2Sn_3$	20	50	2.1	14.2	[313]
$Pd_{77.5}Si1_{6.5}Cu_6$	15	45	1.57	20.5	[314]
$Ce_{60}Al_{20}Ni_{10}Cu_{10}$	5	10	0.6	6.9	[308]
$La_{55}Al_{25}Ni_5Cu_{10}Co_5$	1	5	0.7	1.3	[315]
$Mg_{65}Cu_{25}Tb_{10}$	0.1	2	0.66	0.2	[308]
$Fe_{46}Ni_{32}V_2Si_{14}B_6$	0.02	4	3.8	0.028	[316]
$Fe_{49.7}Cr_{17.7}Mn_{1.9}Mo_{7.4}W_{1.6}B_{15.2}C_{3.8}Si_{2.4}$	-	1.1-1.45	1.7-2.4	0.02-0.034	Present study

Depending on fracture toughness, the size of the plastic zone can vary from nanometers to micrometers for brittle and ductile bulk metallic glasses, respectively. In Zr-based BMGs with a high fracture toughness of 86 MPa•$m^{0.5}$, the size of the plastic zone is about 60 μm, while in brittle Fe-based BMGs with a fracture toughness of 4 MPa•$m^{0.5}$, the plastic zone has a sub-micron size.

Differences in the size of the plastic zone and consequently toughness of diverse bulk metallic glasses could be further investigated by analyzing the Poisson's ratio (ν). For isotropic materials, $-1 \leq \nu \leq 1/2$. In compact and weakly compressible materials such as liquids and rubbers, where stress mainly leads to change of shape, ν approaches 1/2. For most solids such as metals, polymers, and ceramics, $0.25 < \nu < 0.35$. Glasses and minerals are more compressible, thus, exhibit ν values which approach zero. Network structures are materials that can show a negative ν [317, 318]. Most common materials fall in between theses extremes. For instance, ceramics, glasses, and semiconductors have a Poisson's ratio close to 0.25 [319]. For stiff metals, ν varies from 0.25 to 0.42 [320].

Poisson's ratio depends on multiple factors one of which is packing density. Gold- or platinum-based bulk metallic glasses, which are known as some of the densest amorphous alloys, have a Poisson's ratio close to 0.5. On the other hand, crystalline metals which are less densely packed, have a Poisson's ratio of about 1/3 [317]. For crystalline materials, Poisson's ratio seems to increase with packing density. Hence, we are expecting ν of cubic diamond is less than the ν of body centered cubic metals, and the ν of face-centered cubic and hexagonal close-packed structures is even lower. Furthermore, for a given crystalline structure and valence, ν mostly increases with atomic number (*Z*) and, indeed, the electronic band structure as well as the valence electron density come into play. For example, metals with high electrical conductivity like copper, silver, and gold have a high Poisson's ratio [320, 321]. For tetravalent elements, assuming that

these polycrystalline solids are macroscopically isotropic, their Poisson's ratios have are ordered as ν_C (0.2) < ν_{Si} (0.22) < ν_{Ge} (0.278) [322]. Melting temperature is another factor that influences the Poisson's ratio. A higher melting temperature results in smaller Poisson's ratios. Thus, given tungsten is more refractory compared to molybdenum, tungsten has a smaller Poisson's ratio. This also explains why beryllium, combining low *Z* with a high melting point, presents a significantly small Poisson's ratio of 0.032 and is also very brittle [317]. It is interesting to note that there is a simple monotonic trend between Poisson's ratio of complex materials such as polycomponent glasses and their atomic packing density (C_g). Poisson's ratio of a wide range of inorganic glasses increases almost monotonically with atomic packing density. Within limited compositional ranges, linear trends could be observed [321]. For instance, a correlation $\nu = ½ - (1/7.2)$ for C_g has been proposed for silicate glasses [323]. However, it is important to remember that this Equation lacks information regarding the atomic glass network parameters such as interatomic distance and coordination number [317]. Processing/treatment condition is another factor that affects the Poisson's ratio. For specimens with identical chemical composition and initial structure, any treatment (isostatic pressing, agitation, annealing to trigger structural relaxation) that affects the packing density, can alter the Poisson's ratio [324-326]. For instance, the Poisson's ratio of silica glass is in the range of 0.15-0.19 under ambient conditions. After treatments under a high pressure (usually greater than 10 GPa), the Poisson's ratio increases to 0.25 [327] and reaches 0.33 as the pressure exceeds 30 GPa [324]. An increase of ν with C_g could be observed either along elastic loading paths or after permanent densification [327]. Rouxel *et al*. [327] studied the correlation between ν, C_g, and densification by implementing Vickers indentation technique (sharp contact loading) on as-quenched and densified (pressure up to 25 GPa) specimens of glasses with different chemical compositions. Densification in this context involves a collapse of matter into a more

loosely-packed structure and is a displacive transformation [328]. The primary response of the glass to a sharp contact loading is an almost instantaneous elastic sinking of the surface. The equilibrium mean contact pressure (elastic hardness) for a rigid conical indenter are typically 2-3 times larger than the hardness values and are large enough to enhance the densification in pressure sensitive glasses. Consequently, irreversible microscopic deformation events will initiate in a process zone near the indenter tip. These events have the purpose of efficiently relaxing the contact stress by increasing the surface area. The deformation mechanism is either densification in glasses with a relatively low atomic packing density (or equivalently a small Poisson's ratio) or shear flow in glasses with a close-packed atomic network (or equivalently a large Poisson's ratio) or a combination of both in general [327]. Shear flow results in the piling of matter in the vicinity of the indentation whereas densification leaves a well-defined indent surrounded by a weakly distorted flat surface. Both mechanisms are thermally activated, but the activation energy associated with the densification process was found much smaller than the one for shear flow [329, 330].

Connectivity is another parameter that strongly affects the value of Poisson's ratio. High packing density is incompatible with structures that are highly connected; random packing of balls (0D) versus rod (1D) in a box. Poisson's ratio is expected to decrease with increasing the connectivity. For glasses with covalently bonded atoms, the mean coordination number <n> is a helpful index of the connectivity. As <n> increases, covalent bonds come into play and a 3D network builds up which results in a significant decrease in Poisson's ratio [317]. Highly crosslinked networks such as silica lead to small Poisson's ratio (0.19), whereas weakly correlated networks such as chain-based chalcogenide glasses or cluster-based metallic glasses show Poisson's ratio values between 0.3 and 0.4 [321]. However, there are extreme cases such as silicon

oxycarbide glasses, where the formation of CSi_4 tetrahedra based on fourfold covalent carbon atoms further enhances the network cross-linking over that of a-SiO_2, with Poisson's ratio reaching 0.11 for the polymer-derived $SiO_{1.6}C_{0.8}$.

The Poisson's ratio was measured for the sintered samples and values of 0.088 ± 0.005, 0.069 ± 0.015, 0.098 ± 0.000, 0.085 ± 0.002 were obtained for specimens with crystallinity percentages of 20, 34, 43, and 61%, respectively. Ductile bulk metallic glasses are known to have shear modulus to bulk modulus (*G*/*K)* ratios <0.41-0.43 or equivalently Poisson's ratios >0.31-0.32. Gu *et al*. [115] reported a critical Poisson's ratio of 0.32 for Fe-based bulk metallic glasses in which transition from brittleness to plasticity takes place. Our sintered SAM2×5-Dev specimens have a very low Poisson's ratio that justifies their brittleness. It is also well-known that elastic and thermal properties of BMGs are linked with their mechanical characteristics. Generally, the plastic deformation of bulk metallic glasses could be studied as a competition between shear flow and cavitation. Shear flow is triggered via a shear banding process to create a plastic zone before cavitation takes place. The less the activation energy (energy barrier) to initiate the shear banding, the easier the shear banding appears and vice versa. At temperature of glass transition (T_g), the shear flow barrier (W) of a metallic glass is proportional to the shear modulus (G) and molar volume (V_m). This relationship could be expressed as $W(T_g)$ α $G(T_g)$ • $V_m(T_g)$. Factor V_m changes insignificantly within a certain alloy family. Hence, the shear flow barrier (W) of bulk metallic glasses is dominated by the shear modulus (G) and T_g [331]. SAM2×5 has a glass transition temperature (T_g) of ~883 K, which is significantly higher than that of other amorphous steels. Considering the points mentioned above, owing to a very low Poisson's ratio along with a remarkably high shear modulus and glass transition temperature, SAM2x5-Dev bulk specimens are expected to have a very low toughness as well as a very high strength. Nevertheless, the macro-

compressive strength values of sintered specimens [Figure 52(b)] are not comparable to those of other Fe-based bulk metallic glasses and their composites.

Table 7 summarizes the compressive properties, Young's modulus, and hardness of some typical amorphous steels and their composites and compares their properties with those of SAM2×5-Dev. It is worth noticing that SAM2×5-Dev specimens are partially crystalline. On the other hand, Table 7 includes mechanical properties of fully amorphous as well as partially crystalline Fe-based bulk metallic glasses. Since the number of reports that comprehensively studied the mechanical characteristics of Fe-based bulk metallic glass composites are handful, for the sake of wider inclusion, fully amorphous steels and their mechanical features have been tabulated in Table 7 and included in the comparison. One can conclude that FeP(C)-based BMGs have relatively smaller hardness values (<9.3 GPa) compared to FeB- and FeB(C)-based BMGs (above 10.8 GPa), such as SAM2×5-Dev. The SAM2×5-Dev composite with a high concentration (61%) of nanocrystals exhibits a hardness of 12.8 GPa, which is higher than the hardness of most amorphous steels. Although there are amorphous steels that show plastic strains larger than 50% [189], sintered SAM2×5-Dev specimens show no plasticity in room temperature compression tests. On the other hand, they show an elastic strain of about 7.5%, which is significantly higher than that of other bulk amorphous steels. Most of the amorphous steels listed in Table 7, have compressive strengths and Young's moduli of above 3 GPa and 160 GPa, respectively. Our sintered SAM2×5-Dev specimens have values of 1.6-1.76 GPa and 23-27 GPa, respectively.

A typical relationship between the yield strength (σ_y) and hardness (H) is $H / \sigma_y \sim 3.1$ [332]. Using this Equation, the theoretically predicted strength values for the sintered SAM2×5-Dev specimens change between 3230 MPa and 4120 MPa, which are significantly higher than the experimentally obtained compressive strength values which span 1600 MPa to 1760 MPa. Also,

the typical relationship between the yield strength (σ_y) and Young's modulus (E) is $E / \sigma_y \sim 50$ [332]. Employing the preceding Equation, the theoretically predicted Young's modulus values for sintered SAM2×5-Dev specimens with different crystallinities vary from 80 GPa to 118 GPa, which is greater than the experimentally obtained Young's modulus values that vary between 23 GPa and 27 GPa. Deviation of measured compressive strength and Young's modulus values from corresponding theoretical values is caused by the existence of pores in our specimens [307], as seen in Figure 53(f). Given the proven effect of porosity on mechanical properties of materials, the mechanical behavior of SAM2×5-Dev at macro-scale is strongly influenced by the existence of porosity. Due to the brittle characteristics of SAM2×5-Dev, pores significantly deteriorate the macro-strength and Young's modulus of this material.

Table 7. Macro-compressive properties, Young's modulus, and hardness of some typical Fe-based bulk metallic glasses and their composites.

Alloy Composition	σ_y (MPa)	σ_f (MPa)	ε_f (%)	ε_p (%)	E (GPa)	*H* (GPa)	Material's type	Ref.
$Fe_{49.7}Cr_{17.7}Mn_{1.9}Mo_{7.4}W_{1.6}B_{15.2}C_{3.8}Si_{2.4}$	-	1600-1760	7.5-8.2	0	23-27	10.04-12.80	BMG Composite	Present study
$Fe_{60}Co_8Zr_{10}Mo_5W_2B_{15}$	-	3800	-	-	-	13.34	BMG	[95]
$Fe_{51}Mn_{10}Cr_4Mo_{12}Y_2C_{15}B_6$	-	~4000	-	-	195	11.28-11.77	BMG	[156]
$(Fe_{44.3}Cr_5Co_5Mo_{12.8}Mn_{11.2}C_{12.8}B_{5.9})_{98.5}Y_{1.5}$	-	~3000	-	-	257.1 ±16.6	12.0±0.49	BMG	[100]
$[(Fe_{0.6}Co_{0.4})_{0.75}B_{0.2}Si_{0.05}]_{96}Nb_4$	-	4250	0.2	0.25	210	12.26	BMG	[333]
$Fe_{65.5}Cr_4Mo_4Ga_4P_{12}C_5B_{5.5}$	2820	2840	1.91	0.15	161	8.67	BMG	[334]
$[[(Fe_{0.5}Co_{0.5})_{0.75}B_{0.2}Si_{0.05}]_{96}Nb_4]_{99.75}Cu_{0.25}$	-	4050	2.27	0.6	220	-	BMG Composite	[205]
$Fe_{63}Cr_3Mo_{10}P_{12}C_{10}B_2$	2600	3400	-	3.2	178	9.13	BMG	[114]

Table 7 continued

$Fe_{76}Mo_2P_{10}C_{7.5}B_{2.5}Si_2$	3000	3280	-	5.7	-	-	BMG	[335]
$Fe_{77}Mo_5P_9C_{7.5}B_{1.5}$	2200	4300	-	30.6	-	-	BMG Composite	[197]
$[(Fe_{0.432}Co_{0.288}B_{0.192}Si_{0.048}Nb_{0.04})_{0.99}Cr_{0.01}]_{99.7}Cu_{0.3}$	4450	4480	-	2.2	-	-	BMG Composite	[198]
$(Fe_{71}Nb_6B_{23})_{99.5}Cu_{0.5}$	3755	3902	-	4.3	-	-	BMG Composite	[336]
$(Fe_{0.335}Co_{0.335}Nb_{0.06}B_{0.27})_{99.8}Cu_{0.2}$	4900	4930	-	2.4	-	12.06	BMG	[185]
$(Fe_{0.335}Co_{0.335}Nb_{0.06}B_{0.27})_{99.9}Cu_{0.1}$	4830	4890	-	3.7	-	11.95	BMG	[185]
$(Fe_{0.9}Ni_{0.1})_{77}Mo_5P_9C_{7.5}B_{1.5}$	2940	3260	-	8.1	-	-	BMG	[188]
$Fe_{70}Ni_{10}P_{13}C_7$	2690	-	-	>50	-	-	BMG	[189]
$Fe_{60}Ni_{20}P_{13}C_7$	2450	-	-	>50	-	-	BMG	[189]
$(Fe_{77}Mo_5P_9C_{7.5}B_{1.5})_{99.9}Cu_{0.1}$	-	3100	-	6.6	-	-	BMG Composite	[200]
$Fe_{43}Cr_{20}Mo_{10}W_4C_{15}B_6Y_2$	-	3990	-	-	-	12.14	BMG	[337]
$Fe_{66.7}Co_5B_{16.7}Si_{8.3}Zr_{3.3}$	-	-	-	-	191± 3	11.35± 0.08	BMG	[338]
$Fe_{62.5}Co_{10}B_{16.7}Si_{8.3}Hf_{2.5}$	-	-	-	-	212± 2	11.44± 0.12	BMG	[338]

While the crystallinity percentages of the specimens vary over a wide range from 20% to 61%, their fracture toughness and yield strength values fluctuate over a narrow range showing a very weak dependency on crystallinity percentage. This is in contrast with the results we have obtained so far since by increasing the crystallinity percentage in the sintered SAM2×5-Dev composites, their toughness and yield strength change only minimally. Analyzing what happens during the deformation of a BMG composite could shed light on this discrepancy. It was shown previously that the radius of the plastic zone in our specimens varies from 20 nm to 34 nm. On the other hand, according to Figure 49(c), the mean nanocrystal spacing is more than 20 nm. This

means that there are not many nanocrystals in the plastic zone in front of shear bands. As a result, an insignificant contribution of nanocrystals to the stabilization of shear bands and enhancement of the plasticity in sintered samples is logically expected. This is the main reason why the crystallinity percentage does not crucially affect the mechanical response of sintered SAM2×5-Dev under quasi-static deformation mode.

3. 3. 2. 3. Micro-compression Testing

Metallic glasses have recently received a great deal of attention as a potential material in micro-electro-mechanical systems (MEMs). Currently, there are four dominant categories of materials which are widely used for the fabrication of MEMs. These materials include (i) metals like Ni and Al, (ii) nonmetals like Si and Ge, (iii) polymers such as polyimmide, and finally ceramics such as carbides and diamond. However, there is another group of materials which are bulk metallic glasses which offer competitive mechanical superiority over their metallic and crystalline counterparts as well as economic benefits compared with ceramic ones [88, 339-341]. Hence, the mechanical behavior of BMGs at microscale is critical and worth exploring. Plastic deformation of brittle and quasi-brittle materials like BMGs could be properly studied by compression of micropillars machined by FIB in displacement-controlled mode [342-346]. Micro-compression tests were completed on specimens with crystallinity percentages of 34, 43, and 61%, with a diameter and a height of 3μm and 8μm, respectively, with a strain rate of $10^{-3}s^{-1}$, at room temperature, and under displacement-controlled mode (500nm). Figure 54(a) represents a truncated section of the load-displacement curves. There is a serrated pattern, with serrations narrowly spaced, in transitioning from elastic to plastic deformation. Bharathula *et al*. [347] have proposed that the serrated response originates from the non-localized flow of material under

loading which leads to the change of taper angle as well as plastic deformation induced by the formation of shear bands. There is a difference between serration and general onset of yielding. Serrated flow could be triggered and initiated at any stress-concentrating geometric imperfection, while the rest of the sample is still elastically loading, which will end up with brittle failure. On the other hand, general yielding takes place when the whole specimen is compressed to its elastic limit and shear banding deformation is continuously nucleated/reactivated [346]. It has been shown that this premature onset of serrated flow can lead to underestimating the intrinsic yield strength of the material [348]. Serration-accompanied deformation of BMG micropillars could be interpreted as a staircase-like response with pop-up events, which is an indication of serrated flow under load-control conditions. These pop-up events correspond to localized deformation along shear bands, which is very similar to what is seen during nanoindentation of amorphous metals [349, 350]. It has been shown that there is a one-to-one correspondence between the occurrence of a strain burst and appearance of a shear band [347] [351, 352]. However, there are reports [353] in which such a one-to-one correspondence has not been observed. The reason is that some of these stress drops are related to the slip of the top portion of the pillar with respect to the bottom part [343].

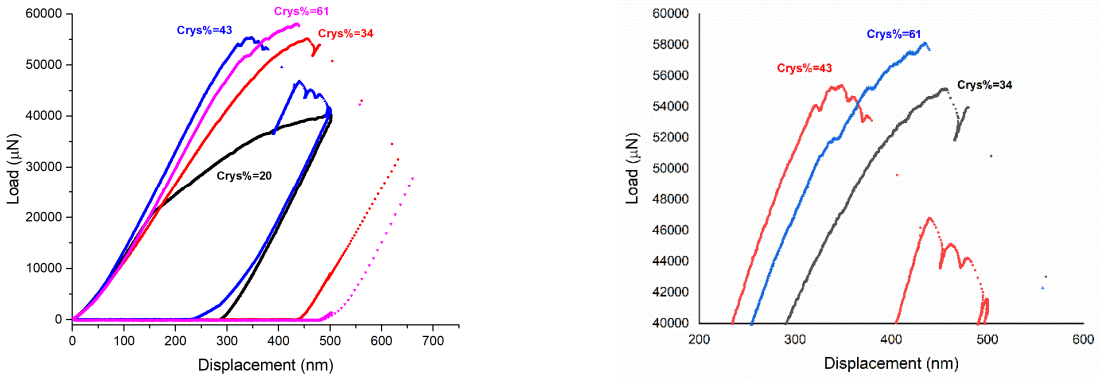

Figure 54. (a) Load-displacement curves during microcompression of micropillars, and (b) a truncated graph illustrating the transition from elastic to plastic deformation illustrated by the serrations in the curves for specimens with different crystallinity percentages.

Figure 55 shows typical SEM images of the micropillars before [Figure 55(a)] and after micro-compression testing [Figure 55(b)-(e)].

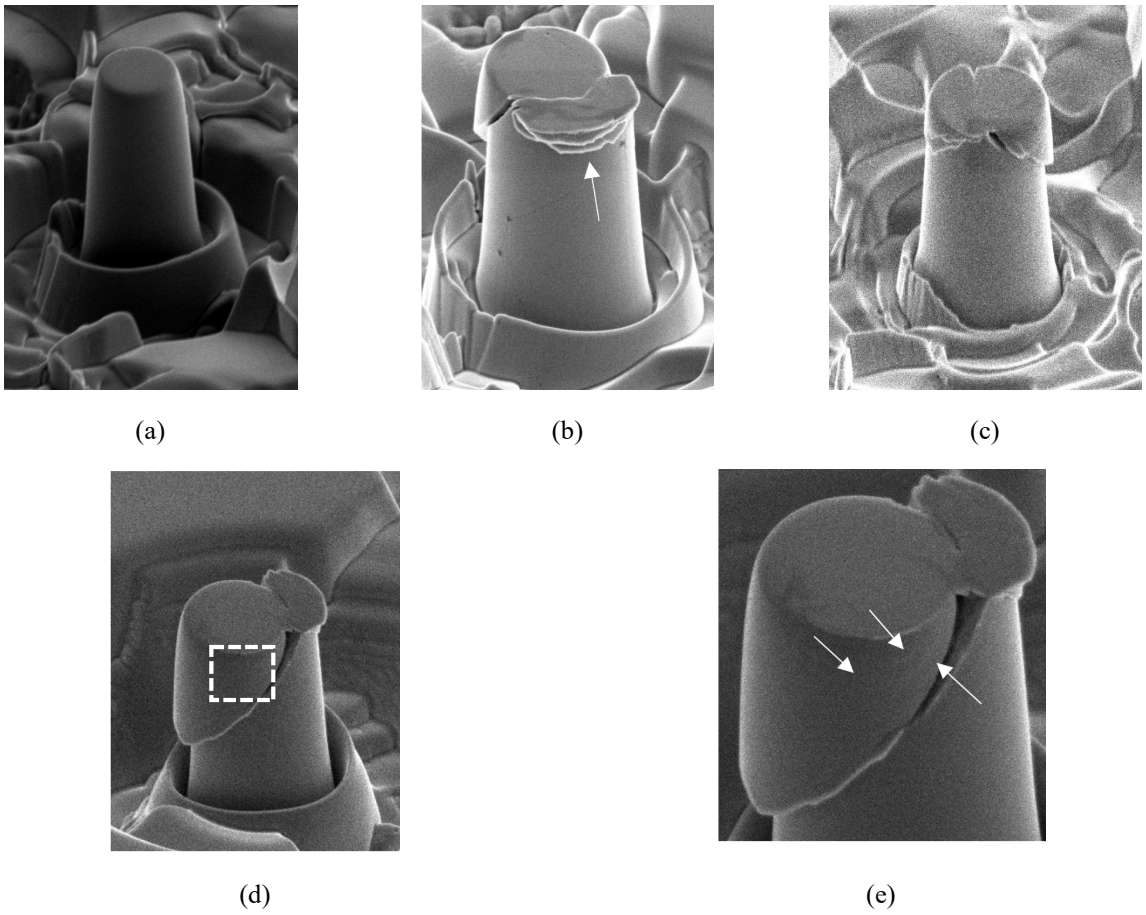

Figure 55. Scanning electron micrographs of (a) a typical micropillar before micro-compression testing and micro-pillars with crystallinity of (b) 34%, (c) 43%, (d) 61% after micro-compression testing. (e) A higher magnification image of (d). The arrow in (b) points to a lip formed at the top corner of pillar and the arrows in (e) show the multiple shear bands formed on the surface of the pillar. All pillars have a diameter of 3 μm and height and 8 μm.

In all samples, failure takes place through the formation and propagation of one principle shear band which causes shear on the micropillar. When implementing micro/nano compression experiments, it is highly likely that potential instrumental artifacts, such as machine lateral stiffness [354, 355], make the results inaccurate. In macro-compression experiments, it is common to use a lubricant between the sample top and the load cell platen that allows the lateral movement of the

sample top and consequently, avoids the constraints associated with the high lateral stiffness of the test setup. However, using lubricants for carrying out micro/nano-compression tests is not practical. Therefore, the recorded mechanical behavior might be strongly affected by lateral constraint. It is anticipated that the consequence of this constraining effect while testing metallic glass micro/nano-pillars would be the nucleation of shear bands near the pillar top assisted by the frictional stress field [352]. As a result, shear bands could be more densely populated near the contact surface. These shear bands intersect the top surface of the micro/nano-pillars where indenter and pillar come into contact, thereby protecting the pillar from catastrophic failure. Moreover, the stress-strain curves might show an artificially enhanced plasticity that is, in fact, a machine artifact [356]. Also, micropillars are integrated to the base material. This can impose constraint on the bottom side of the specimen and lead the plasticity to be initially confined to the upper region of the micropillar and propagate downward [346]. Another potential geometric artifact is the effect of non-planarity of the top of the micropillars. If the top surface of a pillar is not flat, upon contact with the flat punch, the stress state underneath the contact surface will not be uniaxial, affecting the accuracy of recorded response [356]. For instance, Wu *et al.* [357] conducted finite element modeling (FEM) and suggested that, due to the geometric concentration on the top of micro-pillars, non-negligible hydrostatic pressure evolves within the pillar near the contact surface. A hydrostatic stress state creates conditions under which the shear bands cannot form and propagate, leading to suppressed plasticity. The surface of our micropillars were flat and the mechanical response of the specimens was not affected by geometric artifacts. Higher magnification SEM images reveal the formation of multiple shear bands on the sidewalls [Figure 55(e)]. The formation of these premature shear bands is responsible for the local plastic deformation of micropillars after yield. The arrow in Figure 55(b) shows the formation of a lip at

the top corner of one of the deformed pillars. The measurement of the compression response loses its proper physical significance at high strains as soon as the flat punch presses into the remaining lower part of the pillar and forms a characteristic lip. Basically, after slipping of the upper part of the pillar and formation of deformed lip at high strains, the flat punch hits the top of the lower part. This phenomenon will adversely affect the accuracy and validity of plastic strain of micro-pillars. Hence, uniaxial micro-compression tests are mainly useful for evaluating the yield strength [343].

Starting with load-displacement curves, we calculated stress and strain based on the cross-sectional area at the top of the pillar before testing and the initial height obtained from the SEM images. Yield strength and Young's modulus values were extracted from the stress-strain curves and are tabulated in Table 8.

Table 8. Mechanical characteristics of sintered specimens as a function of the crystallinity. Yield strength and Young's modulus values were obtained from macro compression stress-strain curves. The same features at micro scale were extracted from stress-strain curves of micro pillars compression. Also, micro Yield strength and Young's modulus values were corrected for the tapering effect of the micro-pillars. Ultrasound technique (Non-destructive approach) was implemented to measure Young's modulus and Poisson's ratio values. σ_y: Yield strength, E: Young's modulus, R_p: Size of plastic zone, ν: Poisson's ratio.

	Macro-compression			Micro-compression					Non-destructive testing	
Crystallinity (%)	σ_y (GPa)	E (GPa)	R_p (nm)	σ_y (GPa)	E (GPa)	Corrected σ_y (GPa)	Corrected E (GPa)	R_p (nm)	E (GPa)	ν
20	2.4 ± 0.2	23.3 ± 0.2	20	NA	NA	NA	NA	NA	152.2 ± 1.5	0.088 ± 0.005
34	1.7 ± 0.1	26.1 ± 0.5	34	7.9 ± 0.54	224 ± 9	6.4 ± 0.4	153 ± 6	2.39	198.6 ± 2.2	0.069 ± 0.015
43	1.6 ± 0.1	23.8 ± 0.6	25	6.3 ± 0.9	269 ± 23	5.1 ± 0.7	183 ± 16	2.46	220.8 ± 0.9	0.098 ± 0.000
61	1.7 ± 0.2	26.7 ± 1.5	25	6.9 ± 0.45	238 ± 10	5.6 ± 0.4	162 ± 7	2.31	229.4 ± 0.5	0.085 ± 0.002

There are several ways to define yielding in the micro-compression of metallic glass micropillars. These methods include (i) the use of 0.2% strain offset during pop-in [353, 356, 358], (ii) the first detectable pronounced load drop or displacement excursion [343, 347, 357], and (iii) the average flow stress at the 5% plastic strain [359]. Because of different approaches for determining the yield strength, when comparing data from different resources, it is very important to make sure that the same approach for determining the yield strength has been employed. Here we chose the first detectable pronounced load drop or the point from which deformation curves deviate from linear elasticity. By doing so, we are able to compare our data with those presented in most reports. According to Table 8 and considering the standard deviation, one might conclude that all samples have a similar yield strength. Dubach *et al*. [343] carried out uniaxial compression tests on 0.3, 1 and 3 μm diameter micropillars of a Zr-based bulk metallic glass in as-cast, shotpeened and structurally relaxed conditions and concluded that while the samples contain different amounts of free volume, their micro-compression results do not show a significant difference. They proposed that this is because of intrinsic limitations of compression testing, especially for materials susceptible to inhomogeneous flow. For instance, friction between the loading plate and the specimen surface can induce plastic flow via shear band nucleation. The mechanical response of micro-pillars is always influenced by wall tapering, which takes place during manufacturing due to ion beam divergence. For instance, Ye *et al*. [360] examined micropillars with diverse taper angles and reported that a taper angle of 3 degrees can cause about 10% overestimation in strength. All of the pillars that were made and tested in this research were 3.2-5.5 degree tapered. We used methodologies proposed by Ye *et al*. [360] and Bharathula *et al*. [347] to correct the yield strength and Young's modulus for tapering effect. In order to accomplish this correction, we acquired three geometrical variables, the taper angle, the shear band angle, and

the distance from the root of the shear bands on the top surface to the center line of the micropillar. After these factors were determined, corrected yield strength and Young's moduli values were obtained and are reported in Table 8. Uncorrected Young's moduli values are close to the values reported for $Fe_{44.3}Cr_5Co_5Mo_{12.8}Mn_{11.2}C_{15.8}B_{5.9})_{98.5}Y_{1.5}$ of 230 GPa-245 GPa [360, 361] obtained under micro-compression. Young's moduli decrease after being corrected for the taper angle effect.

Table 9 summarizes the compressive response of micropillars with different sizes and chemical compositions reported in the literature. Figure 56 also illustrates the relationship between the room-temperature yield strength and diameter of micro-pillars (with diameters smaller than 4 μm) for various bulk metallic glasses and their composites. It is clearly seen that amorphous steels have a significantly higher strength compared to other categories of bulk metallic glasses, their composites, and nanolaminate micropillars with alternate layers of crystalline and amorphous phases. Micro-mechanical studies of bulk metallic glasses have mainly focused on amorphous specimens produced by melting and casting, or as thin films. There are few reports on conducting micro-compression tests on bulk metallic glass composites. For instance, Lu *et al*. [362] used laser additive manufacturing technology to create structural graded Zr-base bulk metallic glasses containing up to 13 vol.% of crystalline phases. They concluded that the elastic behavior of partially crystallized and fully amorphous specimens is almost identical, however, their yield stress gradually increased as the volume fraction of precipitated crystals increases. They reported an 18% enhancement in yield strength for "seriously crystallized" samples compared to the fully amorphous samples. This incremental trend was attributed to the dispersion strengthening effect from crystalline phases [362]. Sikan *et al*. [363] fabricated $(Zr_{50}Cu_{40}Al_{100})_{100-x}Sm_x$ (x = 0, 2, 4 at.%) ribbons containing different contents of micro-alloyed Sm. Increasing the content of Sm in

as-spun amorphous specimens caused the softening of the amorphous phase due to a decrease of the glass transition temperature. However, annealed (partially crystalline) specimens compared to as-spun (amorphous) ones, present a higher fracture strength due to the precipitation of nano-scale Cu_2Sm phase (precipitation hardening effect). Micro-compression testing showed that as-spun pillars (with and without Sm) exhibit serrated flow associated with the propagation of shear bands, while annealed samples catastrophically failed showing only a few strain bursts events and a very large displacement (offset) at fracture. Despite of improvement of strength, the presence of nano-crystals deteriorates the ductility of partially amorphous samples due to the brittle nature of the nano-crystals acting as rapid crack initiation as well as propagation sites (if amorphous/nanocrystal interface is not stable) [363]. So far, there are very few reports on the micro-compression of amorphous steels. In addition to SAM2×5-Dev, one more Fe-based BMG with a chemical composition of $(Fe_{44.3}Cr_5Co_5Mo_{12.8}Mn_{11.2}C_{15.8}B_{5.9})_{98.5}Y_{1.5}$ has been explored [360, 361]. In these two reports, the yield strength values have been determined using the same approach that we are incorporating in this research and corrected for the taper effect. Moreover, since the sizes of the micropillars are very close to each other and ours, a valid comparison can be made. The strongest fully amorphous or partially amorphous pillar made so far, shows a yield strength of about 4.4 GPa [360]. According to Table 8, the micropillars exhibit yield strength values of 6.4 GPa, 5.1 GPa, and 5.6 GPa, which makes SAM2×5-Dev the strongest bulk metallic glass composite micropillar manufactured so far.

Table 9. A summary of mechanical properties of micropillars with different sized and chemical compositions under compressive load.

Alloy Composition	Pillar size (μm)	σ_y (GPa)	σ_F (GPa)	E (GPa)	Material's type	Ref.
$Fe_{49.7}Cr_{17.7}Mn_{1.9}Mo_{7.4}W_{1.6}B_{15.2}C_{3.8}Si_{2.4}$	D=03, L=8	3.5-6.5	-	130-190	BMG Composite	Present study
$Zr_{63.8}Ni_{16.2}Cu_{15}Al_5$	D=3.8	-	1.99	80	BMG	[352]
$Zr_{63.8}Ni_{16.2}Cu_{15}Al_5$	D=1	-	2.35	81	BMG	[352]
$Zr_{63.8}Ni_{16.2}Cu_{15}Al_5$	D=0.7	-	2.59	88	BMG	[352]
$Zr_{50}Ti_{16.5}Cu_{15}Ni_{18.5}$	0.15	1.17	-	-	BMG	[351]
$Zr_{50}Ti_{16.5}Cu_{15}Ni_{18.5}$	0.5	1.66	-	-	BMG	[351]
$Zr_{50}Ti_{16.5}Cu_{15}Ni_{18.5}$	0.7	1.75	-	-	BMG	[351]
$Cu_{47}Ti_{33}Zr_{11}Ni_6Sn_2Si_1$	0.44	1.71	-	-	BMG	[364]
ZrCu	D=0.9-1, L=2.4-2.5	2.6	-	92	BMG	[365]
0° 500/500 nm ZrCu/ Crystalline Zr	D=0.9-1, L=2.4-2.5	2.2	-	113	Nano laminate	[365]
0° 500/800 nm ZrCu/ Crystalline Zr	D=0.9-1, L=2.4-2.5	2.6	-	124	Nano laminate	[365]
45° 500/500 nm ZrCu/ Crystalline Zr	D=0.9-1, L=2.4-2.5	1.9	-	42	Nano laminate	[365]
$Zr_{55}Pd_{10}Cu_{20}Ni_5Al_{10}$	1-4	2.2	-	88.3	BMG	[366]
$Zr_{58.5}Cu_{15.6}Ni_{12.8}Al_{10.3}Nb_{2.8}$	0.250	3	-	91.4	BMG	[347]
$Zr_{58.5}Cu_{15.6}Ni_{12.8}Al_{10.3}Nb_{2.8}$	1	2.3	-	100	BMG	[347]
$Zr_{58.5}Cu_{15.6}Ni_{12.8}Al_{10.3}Nb_{2.8}$	3.6	2.15	-	80	BMG	[347]
$Pd_{40}Ni_{40}P_{20}$	2.05-2.42	~2	-	-	BMG	[353]
$Zr_{48}Cu_{47.5}Al_4Fe_{0.5}$	Micron	1.39	-	93.2	BMG	[367]
$Zr_{48}Cu_{47}Al_4Co_1$	Micron	1.67	-	95.1	BMG	[367]
$Zr_{35}Ti_{30}Co_6Be_{29}$	0.1	2.56	-	-	BMG	[356]
$Zr_{35}Ti_{30}Co_6Be_{29}$	1.6	2	-	-	BMG	[356]
$Mg_{58}Cu_{31}Nd_5Y_6$	D=2.32, L=10.06	1.34	-	53	BMG	[361]
$Mg_{58}Cu_{31}Nd_5Y_6$	D=8.5, L=15.7	1.02	-	50	BMG	[361]
$Cu_{46.25}Zr_{44.25}Al_{7.5}Er_2$	D=2.07, L=7.42	2.35	-	103	BMG	[361]

Table 9 continued

$Cu_{46.25}Zr_{44.25}Al_{7.5}Er_2$	D=7.7, L=16.4	2.13	-	94.7	BMG	[361]
$(Fe_{44.3}Cr_5Co_5Mo_{12.8}Mn_{11.2}C_{15.8}B_{5.9})_{98.5}Y_{1.5}$	D=3.18, L=9.29	4.27	-	231	BMG	[361]
$(Fe_{44.3}Cr_5Co_5Mo_{12.8}Mn_{11.2}C_{15.8}B_{5.9})_{98.5}Y_{1.5}$	D=7.68, L=13.4	3.08	-	229	BMG	[361]
$Zr_{55}Cu_{30}Ni_5Al_{10}$	D=3.09, L=13.42	1.87	-	98	BMG	[361]
$Zr_{55}Cu_{30}Ni_5Al_{10}$	D=7.91, L=16.9	1.91	-	84	BMG	[361]
$Zr_{50}Cu_{40}Al_{10}$	D=.1.6, L=4.5	2.04	-	-	BMG	[368]
$Zr_{55}Cu_{31}Ti_{14}$ (ZrCuTi)	D=0.9, L=1.5	1.71	-	94	Nano laminate	[369]
50 nm-ZrCuTi/5 nm-Ta	D=0.9, L=1.5	1.91	-	106	Nano laminate	[369]
50 nm-ZrCuTi/50 nm-Ta	D=0.9, L=1.5	3.2	-	159	Nano laminate	[369]
$Zr_{50}Cu_{37}Al_{10}Pd_3$	0.5-8	2.5	-	99	BMG	[360]
$Mg_{58}Cu_{31}Nd_5Y_6$	0.5-8	1.2	-	56	BMG	[360]
$(Fe_{44.3}Cr_5Co_5Mo_{12.8}Mn_{11.2}C_{15.8}B_{5.9})_{98.5}Y_{1.5}$	0.5-8	4.4	-	245	BMG	[360]
$Au_{49}Ag_{5.5}Pd_{2.3}Cu_{26.9}Si_{16.3}$	D=1, L=2	-	1.65	-	BMG	[264]
$Au_{49}Ag_{5.5}Pd_{2.3}Cu_{26.9}Si_{16.3}$	D=3.8, L=7.6	-	1.68	-	BMG	[264]
$Ni_{78}P_{22}$	2	3.3	-	-	BMG	[370]
$Ni_{78}P_{22}$	3.2	1.9			BMG	[370]
$Al_{88}Fe_7Gd_5$	1	1.2			BMG	[371]
$Zr_{57}Ti_5Ni_8Cu_{20}Al_{10}$	D=8, L=18	2.25			BMG	[372]

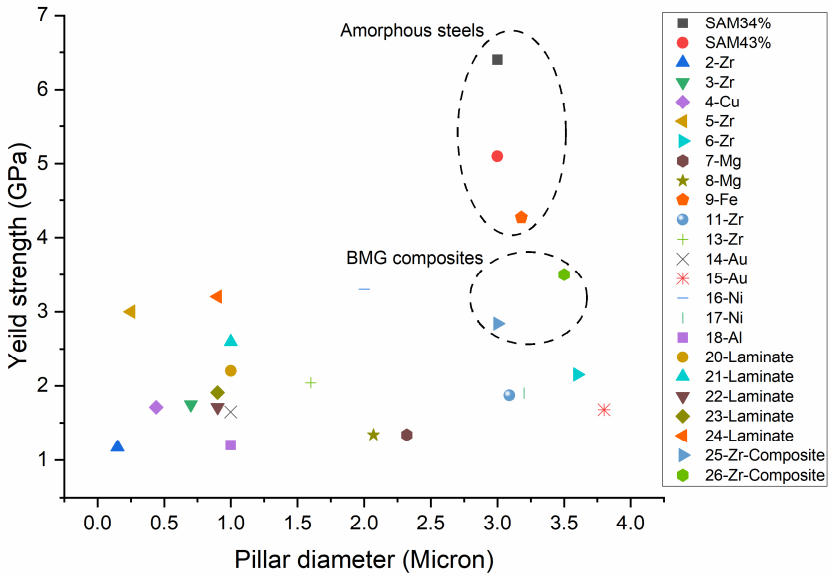

Figure 56. Variation of yield strength with micropillar's diameter for various bulk metallic glasses and composites with different chemical composition. 2: [351], 3: [351], 4: [364], 5: [347], 6: [347], 7: [361], 8: [361], 9: [361], 11: [361], 13: [368], 14: [264], 15: [264], 16: [370], 17: [370], 18: [371], 20: [365], 21: [365], 22: [369], 23: [369], 24: [369], 25: [362], 26: [363]

Similar to the results from macro-compression, the yield strength and Young's modulus from micro-compression of the sintered SAM2×5-Dev specimens are independent of the crystallinity percentage. The size of plastic zone was calculated using Equation (34) and values of 2.39, 2.46, and 2.31 nm were obtained for specimens with crystallinity percentages of 34, 43, and 61, respectively, which is significantly smaller than the mean space between nanocrystal (20 nm). This means that there are no crystals in the plastic zone in front of shear bands. As a result, an insignificant contribution of nanocrystals to the stabilization of shear bands and enhancement of the plasticity in sintered samples is logically expected. This is the main reason that the crystallinity percentage does not crucially affect the micro mechanical response of sintered SAM2×5-Dev under quasi static deformation mode. According to Table 8, for each sintered specimen, two different sizes of plastic zones were obtained. Using the strength recorded from macro-compression testing, the size of the plastic zone was determined to be 20-43 nm. However,

using the micro-compression strength values, the size of the plastic zone was calculated to be around 2.5 nm. Moreover, high resolution SEM images obtained from the fracture surface of macro-compressed specimens did not reveal any dimples with a size in the range 20-43 nm indicating that 2.5 nm is a more realistic value. The reason for obtaining two different numbers for the size of plastic zone in each sample is that, according to Equation (34), as yield strength decreases, the size of plastic zone increases. On the other hand, it was proved the macro-mechanical properties of the SAM2×5-Dev samples were adversely affected by the existence of pores meaning that the macro-compression yield strength values are underestimated which, according to Equation (34), results in a larger size of plastic zone. On the other hand, the yield strength of micro-pillars is less influenced by the presence of defects such as pores. This makes the micro-compression yield strength a better representative of the intrinsic strength of SAM2×5-Dev. This is also the case for the size of plastic zone. Moreover, it highlights the key role of fabrication methodology as well as strong influence of defects on mechanical properties of very brittle materials such as SAM2×5-Dev. Young's modulus of sintered specimens was also measured via resonant ultrasound spectroscopy and the results are tabulated in Table 8. Young's modulus values obtained from ultrasound spectroscopy are much closer to those extracted from micro-compression experiments compared to macro-compression. This finding highlights the role of structural defects on Young's modulus in addition to yield strength.

3. 3. 2. 4. Size effect

Sample miniaturizing can impede catastrophic failure if the size of the plastic zone in front of a sharp crack is larger than the sample size. For instance, Zheng *et al*. [373] observed plastic

deformation and non-catastrophic failure by reducing the size of $Mg_{61}Cu_{28}Gd_{11}$ bulk metallic glass. They postulated the existence of a significantly large plastic zone in front of the crack (10-100 μm), compared to the micropillar size (12 μm), is the main reason for the suppression of brittle fracture. As we will discussed later, the size of the plastic zone in front of crack tip in SAM2×5-Dev is about 2.5 nm, which is much smaller than the size of micropillars (~3 μm). This leads us to anticipate brittle fracture without a significant plastic deformation.

There are reports proposing that brittle failure could be suppressed when the sample size decreases even in brittle ceramics [342, 374] and BMGs [348, 373]. Comparing the yield strength of the SAM2×5-Dev specimens compressed at micro- and macro-scales (Table 8) reveals that, regardless of the crystallinity percentage, the yield strength of all sintered samples compressed at micro-scale is higher than that at macro-scale. The significant increase in the strength of the micro-pillars might be either because of experimental errors or intrinsic size scaling of strength. Experimental inaccuracies increase with decreases of sample size, which is due to the alignment of specimen and loading axis, deviation in diameter determination in the microscope or taper angle [343]. Stress-strain non-uniformity in the tapered micropillar geometries may lead to an overestimation of the mechanical properties [360]. Additionally, Ga-ion implantation during fabrication of micropillars via FIB could be another source of strengthening artifact [343, 352]. According to the literature, there is no report estimating the thickness of damaged layer caused by FIB on Fe-based BMGs. Bei *et al*. [375] examined the hardening of the FIB-milled Mo single crystal induced by various FIB beam voltages (5–30 kV), currents (1.4-7 nA) and exposure durations (7.8-39 min). Generally, the acceleration voltage determines the depth of Ga ion penetration and the current and time determine the degree of damage in the damage zone. It was found that as long as the beam energy, or voltage times current, is lower than 30 kV•nA, the

hardness increment is less than 25%. In another report, the thickness of the damaged area on Zr-based BMG micropillars was estimated by Auger electron spectroscopy to be about 4 nm. For a 0.3 μm pillar, the area contribution of damaged layer is about 5% [352]. On the other hand, Volkert *et al*. [359] proposed that the FIB damage in BMGs compared with that in micro-crystals is insignificant which is due to the lack of crystalline defects. In this research, we used a FIB beam voltage of 30 kV coupled with an initial current of 20 nA for rough beam milling in order to create the outer crater. Then, the beam current was progressively decreased to 1 nA for milling the pillar and finally to 0.1 nA for the final trimming. In the final step, the beam energy during FIB milling would be around 3 kV•nA, which is well below the threshold value to induce significant sample damage or partial crystallization in the metallic glasses [264]. Considering all sources of artificial strengthening with decrease of sample size, there are different reports on the extent of this phenomenon. Dubach *et al*. [343] and Schuster *et al*. [353] showed that by decreasing the sample size of Zr- and Pd-based BMGs, the yield strength increased by 7% and 9%, respectively. Lee *et al.* [376] reported that by decreasing the size of the specimen, the yield strength of Zr- and Mg-based BMGs enhances about 30% and 58%, respectively. For brittle materials, the strength variability and size-scaling of strength is due to their flaw sensitivity [343, 377] or reducing the defect population in the sample [82, 352, 378]. In other words, by decreasing the sample size, the critical flaw population also decreases, which results in enhancement of the strength [343]. Comparing the yield strength values from macro- and micro-compression tests, SAM2×5-Dev shows a very strong size-dependence. By decreasing the size, the yield strength of specimens with crystallinity of 34%, 43% and 61% is enhanced by 270%, 220% and 230%, respectively. Such a strong size effect has not been reported so far for any other bulk metallic glasses/composite. The reason is that SAM2×5-Dev has a very high flaw sensitivity. SAM2×5-Dev bulk samples were

manufactured by spark plasma sintering during which all pores might not be eliminated. Very small values of indentation toughness clearly prove that partially devitrified SAM2×5-Dev is a very brittle amorphous steel composite. Also, by using Equation (34) it was shown that the size of plastic zone in sintered SAM2×5-Dev composites is significantly smaller than the distance between nano-crystals, which weakens the dispersion strengthening effect. Thus, in the presence of a very small density of even small structural defects (such as pores), a shear band can easily initiate and propagate through the sample. Moreover, there is no counter force which can impede the propagation of shear bands and postpone the failure. Therefore, bulk SAM2×5-Dev specimens cannot withstand a very high stress and catastrophically fail under macro-compression.

Chapter 3, in part, is a reprint of the material as it appears in PLOS ONE 2020. A. Yazdani, G.W.H. Höhne, S.T. Misture, and O.A. Graeve. The dissertation/thesis author was the primary investigator and author of this paper.

Chapter 3, in part is currently being prepared for submission for publication of the material. A. Yazdani, D. Dewitt, W. Huang, R. Borja-Urby, H. Luo (Karagozian & Case, Inc.), J. Magallanes (Karagozian & Case, Inc.), D. Kisailus, J. E. Garay, O. A. Graeve. The dissertation/thesis author was the primary investigator and author of this material.

Chapter 4

Conclusions

4. Conclusions

In the first part of this research, a novel method based on differential scanning calorimetry (DSC) is introduced for the determination of initial crystallinity, change of crystallinity, and crystallinity percentage as a function of temperature for amorphous metal alloys by comparing the enthalpy of amorphous, crystalline and partially crystalline specimens. In order to ascertain that the values of calculated crystallinity are close to those of set crystallinities, five calibration samples with different crystallinities were prepared by mixing appropriate amounts of amorphous and crystalline powders. Due to the nature of the DSC technique, there is no need for homogenous mixing of calibration samples, which is considered a merit of this method compared to other characterization methodologies such as X-ray diffraction (XRD). Through a dynamic DSC approach, the variation of heat capacity and enthalpy of amorphous, crystalline and powder mixtures with a known crystallinity were calculated. A linear relationship between the true and calculated crystallinity values guarantees that, unlike conventional methods such as XRD, it is not necessary to prepare and test calibration samples before examining a target specimen. We also used the GUM methodology to quantify the contributions from random and systematic errors. We found that for the pre-mixed sample with composition of 5% crystalline and 95% amorphous content, our methodology yields a crystallinity of $3.0 \pm 1.6\%$. This methodology has a very high accuracy as well as a very broad applicability to diverse amorphous systems including metals, ceramics, polymers, and alloys regardless of crystallization temperature range, and devitrified products. The method loses its accuracy when analyzing amorphous systems in which the crystallization process is accompanied by the occurrence of other phase transformations at the same temperature. Also, to analyze materials in which melting takes place slightly after crystallization terminates, a significantly lower heating rate needs to be incorporated.

In the second part of this research, powder of an amorphous steel with a chemical composition of $Fe_{49.7}Cr_{17.7}Mn_{1.9}Mo_{7.4}W_{1.6}B_{15.2}C_{3.8}Si_{2.4}$ were sintered by spark plasma sintering at different temperatures ranging from 903 K to 948 K. The crystallinity percentage of the sintered specimens, named SAM2×5-Dev, varied from 20% to 61%. Sintered samples consisted of nano-crystals with a size below 20 nm, which were homogenously distributed within the amorphous matrix. A high degree of compaction was achieved for most samples, which resulted in hardness values above 9.8 GPa. The reduction in free volume during the structural relaxation was likely the cause for the increasing hardness. Indentation toughness of all samples was calculated to be below 1.6 $MPa•m^{0.5}$. The room temperature compressive response of the specimens under quasi-static deformation regime showed the yield strengths of the samples was below 2 GPa. Although the hardness of SAM2×5-Dev is comparable to that of other amorphous steels, SAM2×5-Dev has a lower yield strength that is influenced by the sub-micrometer and micrometer-sized pores in the sintered specimens. The fracture surfaces of all specimens consisted of a featureless mirror zone and a shear band branching zone that included massive shear bands indicating localized softening and shear instability. The change of crystallinity percentage does not significantly affect the fracture toughness and yield strength of SAM2×5-Dev under quasi-static deformation regime. The reason is that the radius of the plastic zone in front of a shear band is smaller than the space between nanocrystals. As a result, nanocrystals cannot contribute to impeding shear band propagation. Micro-compression tests were completed on micro-pillars of the SAM2×5-Dev specimens. All the pillars failed through the initiation and propagation of a principle shear band. Nonetheless, multiple shear bands were observed on the side wall of the pillars. Yield strength values corrected for the taper angle effect are in the range of 5.1-6.4 GPa which makes SAM2×5-Dev the strongest bulk metallic glass composite compared to other BMGs and their composites. Such a high strength

was shown to originate from two sources: (i) a very low Poisson's ratio (high shear modulus and low bulk modulus), which impedes the multiplication of shear bands and makes transition from a shear band into crack energetically easier, and (ii) a significantly high glass transition temperature, which creates a larger energy barrier to initiate the shear banding. Failure analysis of micro-pillars proves that the propagation of a principle shear band is responsible for pillar fracture. It was found that the change of crystallinity percentage does not affect the room temperature micro-mechanical behavior of this material. Also, we observed there is a significant size effect in SAM2×5-Dev and found that the yield strength of the micro-pillars is at least 200% higher than that of bulk samples, due to a remarkably high defect sensitivity of SAM2×5-Dev.

References

[1] W.H. Wang, C. Dong, C.H. Shek, Bulk metallic glasses, Materials Science and Engineering: R: Reports, 44 (2004) 45-89.

[2] M. Jafary-Zadeh, G. Praveen Kumar, P.S. Branicio, M. Seifi, J.J. Lewandowski, F. Cui, A Critical Review on Metallic Glasses as Structural Materials for Cardiovascular Stent Applications, J Funct Biomater, 9 (2018) 19.

[3] A.L. Greer, Metallic Glasses, Science, 267 (1995) 1947-1953.

[4] A. Inoue, High Strength Bulk Amorphous Alloys with Low Critical Cooling Rates (Overview), Materials Transactions, JIM, 36 (1995) 866-875.

[5] W.L. Johnson, Bulk Glass-Forming Metallic Alloys: Science and Technology, MRS Bulletin, 24 (1999) 42-56.

[6] M.M. Khan, A. Nemati, Z.U. Rahman, U.H. Shah, H. Asgar, W. Haider, Recent Advancements in Bulk Metallic Glasses and Their Applications: A Review, Critical Reviews in Solid State and Materials Sciences, 43 (2018) 233-268.

[7] M. Chen, A brief overview of bulk metallic glasses, NPG Asia Materials, 3 (2011) 82-90.

[8] A.L. Greer, E. Ma, Bulk Metallic Glasses: At the Cutting Edge of Metals Research, MRS Bulletin, 32 (2007) 611-619.

[9] J.J. Kruzic, Bulk Metallic Glasses as Structural Materials: A Review, Advanced Engineering Materials, 18 (2016) 1308-1331.

[10] R. Busch, The thermophysical properties of bulk metallic glass-forming liquids, JOM, 52 (2000) 39-42.

[11] W. Klement, R.H. Willens, P.O.L. Duwez, Non-crystalline Structure in Solidified Gold–Silicon Alloys, Nature, 187 (1960) 869-870.

[12] H.S. Chen, Thermodynamic considerations on the formation and stability of metallic glasses, Acta Metallurgica, 22 (1974) 1505-1511.

[13] A.J. Drehman, A.L. Greer, D. Turnbull, Bulk formation of a metallic glass: $Pd_{40}Ni_{40}P_{20}$, Applied Physics Letters, 41 (1982) 716-717.

[14] H.W. Kui, A.L. Greer, D. Turnbull, Formation of bulk metallic glass by fluxing, Applied Physics Letters, 45 (1984) 615-616.

[15] A. Inoue, T. Zhang, T. Masumoto, Zr–Al–Ni Amorphous Alloys with High Glass Transition Temperature and Significant Supercooled Liquid Region, Materials Transactions, JIM, 31 (1990) 177-183.

[16] A. Inoue, T. Zhang, T. Masumoto, Al–La–Ni Amorphous Alloys with a Wide Supercooled Liquid Region, Materials Transactions, JIM, 30 (1989) 965-972.

[17] A. Inoue, T. Nakamura, N. Nishiyama, T. Masumoto, Mg–Cu–Y Bulk Amorphous Alloys with High Tensile Strength Produced by a High-Pressure Die Casting Method, Materials Transactions, JIM, 33 (1992) 937-945.

[18] A. Inoue, T. Zhang, N. Nishiyama, K. Ohba, T. Masumoto, Preparation of 16 mm Diameter Rod of Amorphous $Zr_{65}Al_{7.5}Ni_{10}Cu_{17.5}$ Alloy, Materials Transactions, JIM, 34 (1993) 1234-1237.

[19] D. Turnbull, Under what conditions can a glass be formed?, Contemporary Physics, 10 (1969) 473-488.

[20] A. Inoue, T. Zhang, T. Masumoto, Glass-forming ability of alloys, Journal of Non-Crystalline Solids, 156-158 (1993) 473-480.

[21] I.W. Donald, H.A. Davies, Prediction of glass-forming ability for metallic systems, Journal of Non-Crystalline Solids, 30 (1978) 77-85.

[22] T. Egami, Universal criterion for metallic glass formation, Materials Science and Engineering: A, 226-228 (1997) 261-267.

[23] J. Yi, W. Xu, X. Xiong, L. Kong, M. Ferry, J. Li, Glass-Forming Ability and Crystallization Behavior of $Al_{86}Ni_9La_5$ Metallic Glass with Si Addition Advanced Engineering Materials, 18 (2016) 972-977.

[24] E.S. Park, D.H. Kim, Design of Bulk metallic glasses with high glass forming ability and enhancement of plasticity in metallic glass matrix composites: A review, Metals and Materials International, 11 (2005) 19-27.

[25] A. Inoue, A. Takeuchi, Recent development and application products of bulk glassy alloys, Acta Materialia, 59 (2011) 2243-2267.

[26] A. Peker, W.L. Johnson, A highly processable metallic glass: $Zr_{41.2}Ti_{13.8}Cu_{12.5}Ni_{10.0}Be_{22.5}$, Applied Physics Letters, 63 (1993) 2342-2344.

[27] Y.Q. Cheng, E. Ma, H.W. Sheng, Alloying strongly influences the structure, dynamics, and glass forming ability of metallic supercooled liquids, Applied Physics Letters, 93 (2008) 111913.

[28] E.S. Park, H.J. Chang, D.H. Kim, Effect of addition of Be on glass-forming ability, plasticity and structural change in Cu–Zr bulk metallic glasses, Acta Materialia, 56 (2008) 3120-3131.

[29] D.B. Miracle, D.V. Louzguine-Luzgin, L.V. Louzguina-Luzgina, A. Inoue, An assessment of binary metallic glasses: correlations between structure, glass forming ability and stability, International Materials Reviews, 55 (2010) 218-256.

[30] D.C. Hofmann, W.L. Johnson, Improving Ductility in Nanostructured Materials and Metallic Glasses: “Three Laws”, Materials Science Forum, 633-634 (2010) 657-663.

[31] A. Inoue, B. Shen, A. Takeuchi, Developments and Applications of Bulk Glassy Alloys in Late Transition Metal Base System, Materials Transactions, 47 (2006) 1275-1285.

[32] E. Ma, Z. Zhang, Reflections from the glass maze, Nature Materials, 10 (2011) 10-11.

[33] A. Hirata, P. Guan, T. Fujita, Y. Hirotsu, A. Inoue, A.R. Yavari, T. Sakurai, M. Chen, Direct observation of local atomic order in a metallic glass, Nature Materials, 10 (2011) 28-33.

[34] Y.Q. Cheng, E. Ma, Atomic-level structure and structure–property relationship in metallic glasses, Progress in Materials Science, 56 (2011) 379-473.

[35] X. Yue, A. Inoue, C.-T. Liu, C. Fan, The Development of Structure Model in Metallic Glasses, Materials Research, 20 (2017) 326-338.

[36] C.P. Royall, S.R. Williams, The role of local structure in dynamical arrest, Physics Reports, 560 (2015) 1-75.

[37] M. Jafary-Zadeh, R. Tavakoli, J.J. Koh, Z.H. Aitken, Y.W. Zhang, Effect of chemical composition and affinity on the short- and medium-range order structures and mechanical properties of Zr-Ni-Al metallic glass, Journal of Non-Crystalline Solids, 456 (2017) 68-75.

[38] F.C. Frank, J.S. Kasper, Complex alloy structures regarded as sphere packings. I. Definitions and basic principles, Acta Crystallographica, 11 (1958) 184-190.

[39] F.C. Frank, J.S. Kasper, Complex alloy structures regarded as sphere packings. II. Analysis and classification of representative structures, Acta Crystallographica, 12 (1959) 483-499.

[40] N. Mattern, P. Jóvári, I. Kaban, S. Gruner, A. Elsner, V. Kokotin, H. Franz, B. Beuneu, J. Eckert, Short-range order of Cu–Zr metallic glasses, Journal of Alloys and Compounds, 485 (2009) 163-169.

[41] J. Ding, Y.-Q. Cheng, E. Ma, Full icosahedra dominate local order in Cu64Zr34 metallic glass and supercooled liquid, Acta Materialia, 69 (2014) 343-354.

[42] Z.D. Sha, Q.X. Pei, Ab initio study on the electronic origin of glass-forming ability in the binary Cu–Zr and the ternary Cu–Zr–Al(Ag) metallic glasses, Journal of Alloys and Compounds, 619 (2015) 16-19.

[43] H.W. Sheng, Y.Q. Cheng, P.L. Lee, S.D. Shastri, E. Ma, Atomic packing in multicomponent aluminum-based metallic glasses, Acta Materialia, 56 (2008) 6264-6272.

[44] C. Tang, C.H. Wong, A molecular dynamics simulation study of solid-like and liquid-like networks in $Zr_{46}Cu_{46}Al_8$ metallic glass, Journal of Non-Crystalline Solids, 422 (2015) 39-45.

[45] X.W. Gu, M. Jafary-Zadeh, D.Z. Chen, Z. Wu, Y.-W. Zhang, D.J. Srolovitz, J.R. Greer, Mechanisms of Failure in Nanoscale Metallic Glass, Nano Letters, 14 (2014) 5858-5864.

[46] M. Jafary-Zadeh, R. Tavakoli, D.J. Srolovitz, Y.-W. Zhang, Thermally induced failure mechanism transition and its correlation with short-range order evolution in metallic glasses, Extreme Mechanics Letters, 9 (2016) 215-225.

[47] R. Liontas, M. Jafary-Zadeh, Q. Zeng, Y.-W. Zhang, W.L. Mao, J.R. Greer, Substantial tensile ductility in sputtered Zr-Ni-Al nano-sized metallic glass, Acta Materialia, 118 (2016) 270-285.

[48] M. Stoica, N. Van Steenberge, J. Bednarčik, N. Mattern, H. Franz, J. Eckert, Changes in short-range order of $Zr_{55}Cu_{30}Al_{10}Ni_5$ and $Zr_{55}Cu_{20}Al_{10}Ni_{10}Ti_5$ BMGs upon annealing, Journal of Alloys and Compounds, 506 (2010) 85-87.

[49] A.L. Greer, Metallic glasses…on the threshold, Materials Today, 12 (2009) 14-22.

[50] H. Guo, P.F. Yan, Y.B. Wang, J. Tan, Z.F. Zhang, M.L. Sui, E. Ma, Tensile ductility and necking of metallic glass, Nature Materials, 6 (2007) 735-739.

[51] R.T.O. T. C. Hufnagel, and J. Almer, Structural aspects of elastic deformation of a metallic glass, Physical Review B, 73 (2006) 064204.

[52] M.F. Ashby, A.L. Greer, Metallic glasses as structural materials, Scripta Materialia, 54 (2006) 321-326.

[53] H.A. Bruck, A.J. Rosakis, W.L. Johnson, The dynamic compressive behavior of beryllium bearing bulk metallic glasses, Journal of Materials Research, 11 (1996) 503-511.

[54] N. Nishiyama, K. Amiya, A. Inoue, Novel applications of bulk metallic glass for industrial products, Journal of Non-Crystalline Solids, 353 (2007) 3615-3621.

[55] S.-W. Lee, M. Jafary-Zadeh, D.Z. Chen, Y.-W. Zhang, J.R. Greer, Size Effect Suppresses Brittle Failure in Hollow Cu60Zr40 Metallic Glass Nanolattices Deformed at Cryogenic Temperatures, Nano Letters, 15 (2015) 5673-5681.

[56] A.L. Greer, Y.Q. Cheng, E. Ma, Shear bands in metallic glasses, Materials Science and Engineering: R: Reports, 74 (2013) 71-132.

[57] S. Takeuchi, K. Edagawa, Atomistic simulation and modeling of localized shear deformation in metallic glasses, Progress in Materials Science, 56 (2011) 785-816.

[58] H.J. Fecht, Defect-induced melting and solid-state amorphization, Nature, 356 (1992) 133-135.

[59] P. Limthongkul, Y.-I. Jang, N.J. Dudney, Y.-M. Chiang, Electrochemically-driven solid-state amorphization in lithium-silicon alloys and implications for lithium storage, Acta Materialia, 51 (2003) 1103-1113.

[60] L.E. Rehn, P.R. Okamoto, J. Pearson, R. Bhadra, M. Grimsditch, Solid-state amorphization of Zr3Al: Evidence of an elastic instability and first-order phase transformation, Phys Rev Lett, 59 (1987) 2987-2990.

[61] Y.G. Chukalkin, B.N. Goshchitskii, Radiation amorphization of orthoferrite YFeO3, physica status solidi (a), 200 (2003) R9-R11.

[62] F. Shimizu, S. Ogata, J. Li, Theory of Shear Banding in Metallic Glasses and Molecular Dynamics Calculations, Materials Transactions, 48 (2007) 2923-2927.

[63] Q.-K. Li, M. Li, Atomic scale characterization of shear bands in an amorphous metal, Applied Physics Letters, 88 (2006) 241903.

[64] Q.-K. Li, M. Li, Assessing the critical sizes for shear band formation in metallic glasses from molecular dynamics simulation, Applied Physics Letters, 91 (2007) 231905.

[65] Y. Shi, Size-independent shear band formation in amorphous nanowires made from simulated casting, Applied Physics Letters, 96 (2010) 121909.

[66] Y. Shi, M.L. Falk, Stress-induced structural transformation and shear banding during simulated nanoindentation of a metallic glass, Acta Materialia, 55 (2007) 4317-4324.

[67] Q. Xiao, L. Huang, Y. Shi, Suppression of shear banding in amorphous ZrCuAl nanopillars by irradiation, Journal of Applied Physics, 113 (2013) 083514.

[68] J.X. Li, G.B. Shan, K.W. Gao, L.J. Qiao, W.Y. Chu, In situ SEM study of formation and growth of shear bands and microcracks in bulk metallic glasses, Materials Science and Engineering: A, 354 (2003) 337-343.

[69] A.C. Lund, C.A. Schuh, The Mohr–Coulomb criterion from unit shear processes in metallic glass, Intermetallics, 12 (2004) 1159-1165.

[70] F. Spaepen, A microscopic mechanism for steady state inhomogeneous flow in metallic glasses, Acta Metallurgica, 25 (1977) 407-415.

[71] P.E. Donovan, Compressive deformation of amorphous $Pd_{40}Ni_{40}P_{20}$, Materials Science and Engineering, 98 (1988) 487-490.

[72] C.T. Liu, L. Heatherly, J.A. Horton, D.S. Easton, C.A. Carmichael, J.L. Wright, J.H. Schneibel, M.H. Yoo, C.H. Chen, A. Inoue, Test environments and mechanical properties of Zr-base bulk amorphous alloys, Metallurgical and Materials Transactions A, 29 (1998) 1811-1820.

[73] W.J. Wright, R.B. Schwarz, W.D. Nix, Localized heating during serrated plastic flow in bulk metallic glasses, Materials Science and Engineering: A, 319-321 (2001) 229-232.

[74] H. Chen, Y. He, G.J. Shiflet, S.J. Poon, Deformation-induced nanocrystal formation in shear bands of amorphous alloys, Nature, 367 (1994) 541-543.

[75] H.J. Leamy, T.T. Wang, H.S. Chen, Plastic flow and fracture of metallic glass, Metallurgical and Materials Transactions B, 3 (1972) 699.

[76] W.H. Jiang, M. Atzmon, The effect of compression and tension on shear-band structure and nanocrystallization in amorphous $Al_{90}Fe_5Gd_5$: a high-resolution transmission electron microscopy study, Acta Materialia, 51 (2003) 4095-4105.

[77] J.-J. Kim, Y. Choi, S. Suresh, A.S. Argon, Nanocrystallization During Nanoindentation of a Bulk Amorphous Metal Alloy at Room Temperature, Science, 295 (2002) 654-657.

[78] P. Wesseling, P. Lowhahphandu, J.J. Lewandowski, Effects of Superimposed Pressure on Flow and Fracture of Two Bulk Amorphous Metals, MRS Proceedings, 754 (2002) CC11.10.

[79] J. Li, F. Spaepen, T.C. Hufnagel, Nanometre-scale defects in shear bands in a metallic glass, Philosophical Magazine A, 82 (2002) 2623-2630.

[80] P.E. Donovan, W.M. Stobbs, The structure of shear bands in metallic glasses, Acta Metallurgica, 29 (1981) 1419-1436.

[81] Z.F. Zhang, J. Eckert, L. Schultz, Difference in compressive and tensile fracture mechanisms of Zr59Cu20Al10Ni8Ti3 bulk metallic glass, Acta Materialia, 51 (2003) 1167-1179.

[82] A.S. Argon, Plastic deformation in metallic glasses, Acta Metallurgica, 27 (1979) 47-58.

[83] C.A. Schuh, T.C. Hufnagel, U. Ramamurty, Mechanical behavior of amorphous alloys, Acta Materialia, 55 (2007) 4067-4109.

[84] P.S. Steif, F. Spaepen, J.W. Hutchinson, Strain localization in amorphous metals, Acta Metallurgica, 30 (1982) 447-455.

[85] D. Turnbull, M.H. Cohen, Concerning Reconstructive Transformation and Formation of Glass, The Journal of Chemical Physics, 29 (1958) 1049-1054.

[86] V.A. Khonik, The Kinetics of Irreversible Structural Relaxation and Homogeneous Plastic Flow of Metallic Glasses, physica status solidi (a), 177 (2000) 173-189.

[87] P. Duwez, S.C.H. Lin, Amorphous Ferromagnetic Phase in Iron-Carbon-Phosphorus Alloys, Journal of Applied Physics, 38 (1967) 4096-4097.

[88] H.X. Li, Z.C. Lu, S.L. Wang, Y. Wu, Z.P. Lu, Fe-based bulk metallic glasses: Glass formation, fabrication, properties and applications, Progress in Materials Science, 103 (2019) 235-318.

[89] K. Yamauchi, Y. Nakagawa, Amorphous Ferromagnetic Fe-P-B Alloys Prepared by a New Technique of Splat Cooling, Japanese Journal of Applied Physics, 10 (1971) 1730-1730.

[90] M. Kikuchi, H. Fujimori, Y. Obi, T. Masumoto, New Amorphous Ferromagnets with Low Coercive Force, Japanese Journal of Applied Physics, 14 (1975) 1077-1078.

[91] M.E. McHenry, M.A. Willard, D.E. Laughlin, Amorphous and nanocrystalline materials for applications as soft magnets, Progress in Materials Science, 44 (1999) 291-433.

[92] R.B. Schwarz, T.D. Shen, U. Harms, T. Lillo, Soft ferromagnetism in amorphous and nanocrystalline alloys, Journal of Magnetism and Magnetic Materials, 283 (2004) 223-230.

[93] A. Inoue, Y. Shinohara, J.S. Gook, Thermal and Magnetic Properties of Bulk Fe-Based Glassy Alloys Prepared by Copper Mold Casting, Materials Transactions, JIM, 36 (1995) 1427-1433.

[94] A. Inoue, J.S. Gook, Effect of Additional Elements (M) on the Thermal Stability of Supercooled Liquid in $Fe_{72-x}Al_5Ga_2P_{11}C_6B_4M_x$ Glassy Alloys, Materials Transactions, JIM, 37 (1996) 32-38.

[95] A. Inoue, T. Zhang, A. Takeuchi, Bulk amorphous alloys with high mechanical strength and good soft magnetic properties in Fe–TM–B (TM=IV–VIII group transition metal) system, Applied Physics Letters, 71 (1997) 464-466.

[96] W. Zhang, A. Inoue, Formation and Magnetic Properties of Bulk Glassy Fe–Co–Nd–Dy–B Alloys with High Boron Concentrations, Materials Transactions, JIM, 41 (2000) 1679-1682.

[97] B. Shen, H. Kimura, A. Inoue, T. Mizushima, Bulk Glassy Fe–Co–Ga–P–C–B Alloys with High Glass-Forming Ability, High Saturation Magnetization and Good Soft Magnetic Properties, Materials Transactions, JIM, 41 (2000) 1675-1678.

[98] B.-L. Shen, H. Koshiba, T. Mizushima, A. Inoue, Bulk Amorphous Fe-Ga-P-B-C Alloys with a Large Supercooled Liquid Region, Materials Transactions, JIM, 41 (2000) 873-876.

[99] T.D. Shen, R.B. Schwarz, Bulk ferromagnetic glasses in the Fe–Ni–P–B System, Acta Materialia, 49 (2001) 837-847.

[100] V. Ponnambalam, S.J. Poon, G.J. Shiflet, Fe-based bulk metallic glasses with diameter thickness larger than one centimeter, Journal of Materials Research, 19 (2004) 1320-1323.

[101] Z.P. Lu, C.T. Liu, J.R. Thompson, W.D. Porter, Structural amorphous steels, Phys Rev Lett, 92 (2004) 245503.

[102] A. Inoue, F.L. Kong, Q.K. Man, B.L. Shen, R.W. Li, F. Al-Marzouki, Development and applications of Fe- and Co-based bulk glassy alloys and their prospects, Journal of Alloys and Compounds, 615 (2014) S2-S8.

[103] N. Nishiyama, K. Takenaka, H. Miura, N. Saidoh, Y. Zeng, A. Inoue, The world's biggest glassy alloy ever made, Intermetallics, 30 (2012) 19-24.

[104] H.B. Lou, X.D. Wang, F. Xu, S.Q. Ding, Q.P. Cao, K. Hono, J.Z. Jiang, 73 mm-diameter bulk metallic glass rod by copper mould casting, Applied Physics Letters, 99 (2011) 051910.

[105] M.Q. Tang, H.F. Zhang, Z.W. Zhu, H.M. Fu, A.M. Wang, H. Li, Z.Q. Hu, TiZr-base Bulk Metallic Glass with over 50 mm in Diameter, Journal of Materials Science & Technology, 26 (2010) 481-486.

[106] T. Zhang, R. Li, S. Pang, Effect of similar elements on improving glass-forming ability of La–Ce-based alloys, Journal of Alloys and Compounds, 483 (2009) 60-63.

[107] Q. Zhang, W. Zhang, A. Inoue, Fabrication of New $Cu_{34}Pd_2Zr_{48}Ag_8Al_8$ Bulk Glassy Alloy with a Diameter of 30 mm, Materials Transactions, 48 (2007) 3031-3033.

[108] Q. Zheng, J. Xu, E. Ma, High glass-forming ability correlated with fragility of Mg–Cu(Ag)–Gd alloys, Journal of Applied Physics, 102 (2007) 113519.

[109] Y. Zeng, N. Nishiyama, T. Yamamoto, A. Inoue, Ni-Rich Bulk Metallic Glasses with High Glass-Forming Ability and Good Metallic Properties, Materials Transactions, 50 (2009) 2441-2445.

[110] J. Schroers, W.L. Johnson, Highly processable bulk metallic glass-forming alloys in the Pt–Co–Ni–Cu–P system, Applied Physics Letters, 84 (2004) 3666-3668.

[111] K.F. Yao, C.Q. Zhang, Fe-based bulk metallic glass with high plasticity, Applied Physics Letters, 90 (2007) 061901.

[112] X. Li, H. Kato, K. Yubuta, A. Makino, A. Inoue, Effect of Cu on nanocrystallization and plastic properties of FeSiBPCu bulk metallic glasses, Materials Science and Engineering: A, 527 (2010) 2598-2602.

[113] J.M. Park, D.H. Kim, J. Eckert, Enhanced plasticity of Fe–Nb–B–(Ni, Cu) bulk metallic glasses by controlling the heterogeneity and elastic constants, Journal of Alloys and Compounds, 536 (2012) S70-S73.

[114] X.J. Gu, S.J. Poon, G.J. Shiflet, M. Widom, Ductility improvement of amorphous steels: Roles of shear modulus and electronic structure, Acta Materialia, 56 (2008) 88-94.

[115] X.J. Gu, A.G. McDermott, S.J. Poon, G.J. Shiflet, Critical Poisson's ratio for plasticity in Fe–Mo–C–B–Ln bulk amorphous steel, Applied Physics Letters, 88 (2006) 211905.

[116] J.J. Lewandowski, X.J. Gu, A.S. Nouri, S.J. Poon, G.J. Shiflet, Tough Fe-based bulk metallic glasses, Applied Physics Letters, 92 (2008) 091918.

[117] C. Suryanarayana, A. Inoue, Iron-based bulk metallic glasses, International Materials Reviews, 58 (2013) 131-166.

[118] A.L. Greer, Confusion by design, Nature, 366 (1993) 303-304.

[119] Q. Li, J. Li, P. Gong, K. Yao, J. Gao, H. Li, Formation of bulk magnetic ternary Fe80P13C7 glassy alloy, Intermetallics, 26 (2012) 62-65.

[120] M. Stoica, K. Hajlaoui, A. LeMoulec, A.R. Yavari, New ternary Fe-based bulk metallic glass with high boron content, Philosophical Magazine Letters, 86 (2006) 267-275.

[121] J. Wang, R. Li, N. Hua, L. Huang, T. Zhang, Ternary Fe–P–C bulk metallic glass with good soft-magnetic and mechanical properties, Scripta Materialia, 65 (2011) 536-539.

[122] A. Inoue, Stabilization of metallic supercooled liquid and bulk amorphous alloys, Acta Materialia, 48 (2000) 279-306.

[123] Y.T. Sun, H.Y. Bai, M.Z. Li, W.H. Wang, Machine Learning Approach for Prediction and Understanding of Glass-Forming Ability, The Journal of Physical Chemistry Letters, 8 (2017) 3434-3439.

[124] H.J. Fecht, W.L. Johnson, Thermodynamic properties and metastability of bulk metallic glasses, Materials Science and Engineering: A, 375-377 (2004) 2-8.

[125] R. Busch, W. Liu, W.L. Johnson, Thermodynamics and kinetics of the $Mg_{65}Cu_{25}Y_{10}$ bulk metallic glass forming liquid, Journal of Applied Physics, 83 (1998) 4134-4141.

[126] S.F. Guo, K.C. Chan, S.H. Xie, P. Yu, Y.J. Huang, H.J. Zhang, Novel centimeter-sized Fe-based bulk metallic glass with high corrosion resistance in simulated acid rain and seawater, Journal of Non-Crystalline Solids, 369 (2013) 29-33.

[127] J. Shen, Q. Chen, J. Sun, H. Fan, G. Wang, Exceptionally high glass-forming ability of an FeCoCrMoCBY alloy, Applied Physics Letters, 86 (2005) 151907.

[128] H. Li, W. Luo, Q. Zeng, Z. Lin, H. Luo, Y. Zhang, Method for the determination of blood methotrexate by high performance liquid chromatography with online post-column electrochemical oxidation and fluorescence detection, Journal of Chromatography B, 845 (2007) 164-168.

[129] R.D. Ma, H.F. Zhang, H.S. Yu, Z.Q. Hu, The effect of Al substitution on thermal and mechanical properties of Fe-based bulk metallic glass, Journal of Alloys and Compounds, 454 (2008) 370-373.

[130] F. Li, B. Shen, A. Makino, A. Inoue, Excellent soft-magnetic properties of (Fe,Co)–Mo–(P,C,B,Si) bulk glassy alloys with ductile deformation behavior, Applied Physics Letters, 91 (2007) 234101.

[131] H.X. Li, J.E. Gao, Z.B. Jiao, Y. Wu, Z.P. Lu, Glass-forming ability enhanced by proper additions of oxygen in a Fe-based bulk metallic glass, Applied Physics Letters, 95 (2009) 161905.

[132] C.Y. Luo, Y.H. Zhao, X.K. Xi, G. Wang, D.Q. Zhao, M.X. Pan, W.H. Wang, S.Z. Kou, Making amorphous steel in air by rare earth microalloying, Journal of Non-Crystalline Solids, 352 (2006) 185-188.

[133] T.A. Waniuk, R. Busch, A. Masuhr, W.L. Johnson, Equilibrium viscosity of the $Zr_{41.2}Ti_{13.8}Cu_{12.5}Ni_{10}Be_{22.5}$ bulk metallic glass-forming liquid and viscous flow during relaxation, phase separation, and primary crystallization, Acta Materialia, 46 (1998) 5229-5236.

[134] J.H. Na, M.D. Demetriou, W.L. Johnson, Fragility of iron-based glasses, Applied Physics Letters, 99 (2011) 161902.

[135] Y. Lu, Y. Huang, W. Zheng, J. Shen, Free volume and viscosity of Fe–Co–Cr–Mo–C–B–Y bulk metallic glasses and their correlation with glass-forming ability, Journal of Non-Crystalline Solids, 358 (2012) 1274-1277.

[136] Y. Lu, Y. Huang, J. Shen, X. Lu, Z. Qin, Z. Zhang, Effect of Co addition on the shear viscosity of Fe-based bulk metallic glasses, Journal of Non-Crystalline Solids, 403 (2014) 62-66.

[137] A. Inoue, Slowly-Cooled Bulk Amorphous Alloys, Materials Science Forum, 179-181 (1995) 691-700.

[138] Z.P. Lu, C.T. Liu, Role of minor alloying additions in formation of bulk metallic glasses: A Review, Journal of Materials Science, 39 (2004) 3965-3974.

[139] J.E. Gao, Z.P. Chen, Q. Du, H.X. Li, Y. Wu, H. Wang, X.J. Liu, Z.P. Lu, Fe-based bulk metallic glass composites without any metalloid elements, Acta Materialia, 61 (2013) 3214-3223.

[140] D.E. Polk, Structural model for amorphous metallic alloys, Scripta Metallurgica, 4 (1970) 117-122.

[141] Y. Wu, X.D. Hui, Z.P. Lu, Z.Y. Liu, L. Liang, G.L. Chen, Effects of metalloid elements on the glass-forming ability of Fe-based alloys, Journal of Alloys and Compounds, 467 (2009) 187-190.

[142] L. Xia, S.S. Fang, Q. Wang, Y.D. Dong, C.T. Liu, Thermodynamic modeling of glass formation in metallic glasses, Applied Physics Letters, 88 (2006) 171905.

[143] S.L. Wang, H.X. Li, X.F. Zhang, S. Yi, Effects of Cr contents in Fe-based bulk metallic glasses on the glass forming ability and the corrosion resistance, Materials Chemistry and Physics, 113 (2009) 878-883.

[144] H.X. Li, K.B. Kim, S. Yi, Enhanced glass-forming ability of Fe-based bulk metallic glasses prepared using hot metal and commercial raw materials through the optimization of Mo content, Scripta Materialia, 56 (2007) 1035-1038.

[145] Y. Fu, B. Shen, H. Kimura, A. Makino, A. Inoue, Enhanced glass-forming ability of FeCoBSiNb bulk glassy alloys prepared using commercial raw materials through the optimization of Nb content, Journal of Applied Physics, 107 (2010) 09A315.

[146] H.X. Li, Z.B. Jiao, J.E. Gao, Z.P. Lu, Synthesis of bulk glassy Fe–C–Si–B–P–Ga alloys with high glass-forming ability and good soft-magnetic properties, Intermetallics, 18 (2010) 1821-1825.

[147] S. Joseph, G.J. Shiflet, V. Ponnambalam, V.M. Keppens, R. Taylor, G. Petculescu, Synthesis and Properties of High-Manganese Iron-Based Bulk Amorphous Metals as Non-Ferromagnetic Amorphous Steel Alloys, MRS Proceedings, 754 (2002) CC1.2.

[148] P. Pawlik, K. Pawlik, H.A. Davies, J.J. Wysłocki, W. Kaszuwara, M. Leonowicz, Glass forming abilities and magnetic properties of soft magnetic Fe–Co–Zr–W–B bulk glassy alloys, Journal of Magnetism and Magnetic Materials, 304 (2006) e733-e735.

[149] H.W. Chang, Y.C. Huang, C.W. Chang, C.H. Chiu, W.C. Chang, Glass formability and soft magnetic properties of bulk Y–Fe–B–Ti metals, Journal of Alloys and Compounds, 462 (2008) 68-72.

[150] H. Koshiba, A. Inoue, A. Makino, Fe-based soft magnetic amorphous alloys with a wide supercooled liquid region, Journal of Applied Physics, 85 (1999) 5136-5138.

[151] Y. Long, W. Zhang, X. Wang, A. Inoue, Effects of transition metal substitution on the glass-formation ability and magnetic properties of $Fe_{62}Co_{9.5}Nd_3Dy_{0.5}B_{25}$ glassy alloy, Journal of Applied Physics, 91 (2002) 5227-5229.

[152] A. Makino, A. Kazahari, W. Zhang, K. Yubuta, T. Kubota, A. Inoue, Synthesis of soft/hard magnetic FePt-based glassy alloys with supercooled liquid region, Journal of Applied Physics, 104 (2008) 103540.

[153] Z.B. Jiao, H.X. Li, J.E. Gao, Y. Wu, Z.P. Lu, Effects of alloying elements on glass formation, mechanical and soft-magnetic properties of Fe-based metallic glasses, Intermetallics, 19 (2011) 1502-1508.

[154] A. Takeuchi, A. Inoue, Classification of Bulk Metallic Glasses by Atomic Size Difference, Heat of Mixing and Period of Constituent Elements and Its Application to Characterization of the Main Alloying Element, Materials Transactions, 46 (2005) 2817-2829.

[155] Z.P. Lu, C.T. Liu, X.Z. Wang, Minor additions of Sn in a bulk glass-forming Fe-based system, Journal of Materials Research, 21 (2006) 3180-3186.

[156] V. Ponnambalam, S.J. Poon, G.J. Shiflet, Fe–Mn–Cr–Mo–(Y,Ln)–C–B (Ln = Lanthanides) bulk metallic glasses as formable amorphous steel alloys, Journal of Materials Research, 19 (2004) 3046-3052.

[157] K. Hono, D.H. Ping, M. Ohnuma, H. Onodera, Cu clustering and Si partitioning in the early crystallization stage of an $Fe_{73.5}Si_{13.5}B_9Nb_3Cu_1$ amorphous alloy, Acta Materialia, 47 (1999) 997-1006.

[158] M. Stoica, R. Li, S. Roth, J. Eckert, G. Vaughan, A.R. Yavari, $[(Fe_{0.5}Co_{0.5})_{0.75}B_{0.20}Si_{0.05}]_{96}Nb_4$ Metallic Glasses with Small Cu Additions, Metallurgical and Materials Transactions A, 42 (2011) 1476-1480.

[159] L. Dou, H. Liu, L. Hou, L. Xue, W. Yang, Y. Zhao, C. Chang, B. Shen, Effects of Cu substitution for Fe on the glass-forming ability and soft magnetic properties for Fe-based bulk metallic glasses, Journal of Magnetism and Magnetic Materials, 358-359 (2014) 23-26.

[160] Z. Li, A. Wang, C. Chang, Y. Wang, B. Dong, S. Zhou, FeSiBPNbCu alloys with high glass-forming ability and good soft magnetic properties, Intermetallics, 54 (2014) 225-231.

[161] H.X. Li, J.E. Gao, Y. Wu, Z.B. Jiao, D. Ma, A.D. Stoica, X.L. Wang, Y. Ren, M.K. Miller, Z.P. Lu, Enhancing glass-forming ability via frustration of nano-clustering in alloys with a high solvent content, Scientific Reports, 3 (2013) 1983.

[162] A. Hirata, Y. Hirotsu, K. Amiya, A. Inoue, Quasicrystal-like structure and its crystalline approximant in an Fe48Cr15Mo14C15B6Tm2 bulk metallic glass, Journal of Alloys and Compounds, 504 (2010) S186-S189.

[163] Y.H. A. Hirata, E. Matsubara, T. Ohkubo, K. Hono, Mechanism of nanocrystalline microstructure formation in amorphous Fe-Nb-B alloys, Physical Reviewe B, 74 (2006) 184204-184210.

[164] G. Herzer, Modern soft magnets: Amorphous and nanocrystalline materials, Acta Materialia, 61 (2013) 718-734.

[165] A. Inoue, Bulk amorphous alloys with soft and hard magnetic properties, Materials Science and Engineering: A, 226-228 (1997) 357-363.

[166] A. Inoue, A. Takeuchi, T. Zhang, Ferromagnetic bulk amorphous alloys, Metallurgical and Materials Transactions A, 29 (1998) 1779-1793.

[167] H. Grahl, S. Roth, J. Eckert, L. Schultz, Stability and magnetic properties of Fe-based amorphous alloys with supercooled liquid region, Journal of Magnetism and Magnetic Materials, 254-255 (2003) 23-25.

[168] W.M. Wang, A. Gebert, S. Roth, U. Kuehn, L. Schultz, Effect of Si on the glass-forming ability, thermal stability and magnetic properties of Fe–Co–Zr–Mo–W–B alloys, Journal of Alloys and Compounds, 459 (2008) 203-208.

[169] C. Yang, T. Wei, J. Zeng, L.H. Liu, S.G. Qu, Y.Y. Li, Microstructure evolution and thermal properties in FeMoPCB alloy during mechanical alloying, Journal of Non-Crystalline Solids, 358 (2012) 1459-1464.

[170] M.A. Nowroozi, H. Shokrollahi, Magnetic and structural properties of amorphous/nanocrystalline $Fe_{42}Ni_{28}Zr_8Ta_2B_{10}C_{10}$ soft magnetic alloy produced by mechanical alloying, Advanced Powder Technology, 24 (2013) 1100-1108.

[171] Y.B. Kim, D.H. Jang, H.K. Seok, K.Y. Kim, Fabrication of Fe–Si–B based amorphous powder cores by cold pressing and their magnetic properties, Materials Science and Engineering: A, 449-451 (2007) 389-393.

[172] M. Yagi, I. Endo, I. Otsuka, H. Yamamoto, R. Okuno, H. Koshimoto, A. Shintani, Magnetic properties of Fe-based amorphous powder cores produced by a hot-pressing method, Journal of Magnetism and Magnetic Materials, 215-216 (2000) 284-287.

[173] S. Yoshida, T. Mizushima, A. Makino, A. Inoue, Structure and soft magnetic properties of bulk Fe-Al-Ga-P-C-B-Si glassy alloys prepared by consolidating amorphous powders, Materials Science and Engineering: A, 304-306 (2001) 1019-1022.

[174] G. Xie, D.V. Louzguine-Luzgin, A. Inoue, Formation and properties of two-phase bulk metallic glasses by spark plasma sintering, Journal of Alloys and Compounds, 509 (2011) S214-S218.

[175] X. Li, A. Makino, H. Kato, A. Inoue, T. Kubota, Fe76Si9.6B8.4P6 glassy powder soft-magnetic cores with low core loss prepared by spark-plasma sintering, Materials Science and Engineering: B, 176 (2011) 1247-1250.

[176] S. Lesz, R. Babilas, M. Nabiałek, M. Szota, M. Dośpiał, R. Nowosielski, The characterization of structure, thermal stability and magnetic properties of Fe–Co–B–Si–Nb bulk amorphous and nanocrystalline alloys, Journal of Alloys and Compounds, 509 (2011) S197-S201.

[177] Z.H. Gan, H.Y. Yi, J. Pu, J.F. Wang, J.Z. Xiao, Preparation of bulk amorphous Fe–Ni–P–B–Ga alloys from industrial raw materials, Scripta Materialia, 48 (2003) 1543-1547.

[178] Q. Li, Formation of ferromagnetic bulk amorphous $Fe_{40}Ni_{40}P_{14}B_6$ alloys, Materials Letters, 60 (2006) 3113-3117.

[179] Z. Mahbooba, L. Thorsson, M. Unosson, P. Skoglund, H. West, T. Horn, C. Rock, E. Vogli, O. Harrysson, Additive manufacturing of an iron-based bulk metallic glass larger than the critical casting thickness, Applied Materials Today, 11 (2018) 264-269.

[180] S. Pauly, L. Löber, R. Petters, M. Stoica, S. Scudino, U. Kühn, J. Eckert, Processing metallic glasses by selective laser melting, Materials Today, 16 (2013) 37-41.

[181] H.Y. Jung, S.J. Choi, K.G. Prashanth, M. Stoica, S. Scudino, S. Yi, U. Kühn, D.H. Kim, K.B. Kim, J. Eckert, Fabrication of Fe-based bulk metallic glass by selective laser melting: A parameter study, Materials & Design, 86 (2015) 703-708.

[182] N. Li, J. Zhang, W. Xing, D. Ouyang, L. Liu, 3D printing of Fe-based bulk metallic glass composites with combined high strength and fracture toughness, Materials & Design, 143 (2018) 285-296.

[183] W. Wu, H. Du, H. Sui, B. Sun, B. Wang, Z. Yu, H. Ni, G. Li, J. Zhao, Study of printing parameters of pneumatic-injection 3D printing of Fe-based metallic glass, Journal of Non-Crystalline Solids, 489 (2018) 50-56.

[184] E. Williams, N. Lavery, Laser processing of bulk metallic glass: A review, Journal of Materials Processing Technology, 247 (2017) 73-91.

[185] C. Zhao, C. Dun, Q. Man, B. Shen, Enhancement of plastic deformation in FeCoNbB bulk metallic glass with superhigh strength, Intermetallics, 32 (2013) 408-412.

[186] X.J. Gu, S.J. Poon, G.J. Shiflet, Effects of carbon content on the mechanical properties of amorphous steel alloys, Scripta Materialia, 57 (2007) 289-292.

[187] X.J. Gu, S.J. Poon, G.J. Shiflet, Mechanical properties of iron-based bulk metallic glasses, Journal of Materials Research, 22 (2011) 344-351.

[188] A. Seifoddini, M. Stoica, M. Nili-Ahmadabadi, S. Heshmati-Manesh, U. Kühn, J. Eckert, New $(Fe_{0.9}Ni_{0.1})_{77}Mo_5P_9C_{7.5}B_{1.5}$ glassy alloys with enhanced glass-forming ability and large compressive strain, Materials Science and Engineering: A, 560 (2013) 575-582.

[189] C. Wan, W. Yang, H. Liu, M. Zuo, Q. Li, Z. Ma, Y. Zhao, A. Inoue, Ductile Fe-based bulk metallic glasses at room temperature, Materials Science and Technology, 34 (2018) 751-756.

[190] W. Yang, H. Liu, Y. Zhao, A. Inoue, K. Jiang, J. Huo, H. Ling, Q. Li, B. Shen, Mechanical properties and structural features of novel Fe-based bulk metallic glasses with unprecedented plasticity, Scientific Reports, 4 (2014) 6233.

[191] H.-K. Kim, K.-B. Lee, J.-C. Lee, Ductile Fe-based amorphous alloy, Materials Science and Engineering: A, 552 (2012) 399-403.

[192] J.M. Park, J.H. Na, D.H. Kim, K.B. Kim, N. Mattern, U. Kühn, J. Eckert, Medium range ordering and its effect on plasticity of Fe–Mn–B–Y–Nb bulk metallic glass, Philosophical Magazine, 90 (2010) 2619-2633.

[193] B. Sarac, Y.P. Ivanov, A. Chuvilin, T. Schöberl, M. Stoica, Z. Zhang, J. Eckert, Origin of large plasticity and multiscale effects in iron-based metallic glasses, Nature Communications, 9 (2018) 1333.

[194] W. Chen, K.C. Chan, S.F. Guo, P. Yu, Plasticity improvement of an Fe-based bulk metallic glass by geometric confinement, Materials Letters, 65 (2011) 1172-1175.

[195] F.-F. Wu, Z.-F. Zhang, B.-L. Shen, S.X.-Y. Mao, J. Eckert, Size Effect on Shear Fracture and Fragmentation of a $Fe_{57.6}Co_{14.4}B_{19.2}Si_{4.8}Nb_4$ Bulk Metallic Glass, Advanced Engineering Materials, 10 (2008) 727-730.

[196] Y. Wu, H.X. Li, Z.B. Jiao, J.E. Gao, Z.P. Lu, Size effects on the compressive deformation behaviour of a brittle Fe-based bulk metallic glass, Philosophical Magazine Letters, 90 (2010) 403-412.

[197] S.F. Guo, L. Liu, N. Li, Y. Li, Fe-based bulk metallic glass matrix composite with large plasticity, Scripta Materialia, 62 (2010) 329-332.

[198] X. Li, H. Kato, K. Yubuta, A. Makino, A. Inoue, Improved plasticity of iron-based high-strength bulk metallic glasses by copper-induced nanocrystallization, Journal of Non-Crystalline Solids, 357 (2011) 3002-3005.

[199] A. Makino, X. Li, K. Yubuta, C. Chang, T. Kubota, A. Inoue, The effect of Cu on the plasticity of Fe–Si–B–P-based bulk metallic glass, Scripta Materialia, 60 (2009) 277-280.

[200] S. Guo, C. Su, Micro/nano ductile-phases reinforced Fe-based bulk metallic glass matrix composite with large plasticity, Materials Science and Engineering: A, 707 (2017) 44-50.

[201] J.J. Lewandowski, W.H. Wang, A.L. Greer, Intrinsic plasticity or brittleness of metallic glasses, Philosophical Magazine Letters, 85 (2005) 77-87.

[202] H.S. Chen, J.T. Krause, E. Coleman, Elastic constants, hardness and their implications to flow properties of metallic glasses, Journal of Non-Crystalline Solids, 18 (1975) 157-171.

[203] S.F. Guo, J.L. Qiu, P. Yu, S.H. Xie, W. Chen, Fe-based bulk metallic glasses: Brittle or ductile?, Applied Physics Letters, 105 (2014) 161901.

[204] X.M. Huang, X.D. Wang, Y. He, Q.P. Cao, J.Z. Jiang, Are there two glass transitions in Fe–M–Y–B (M=Mo, W, Nb) bulk metallic glasses?, Scripta Materialia, 60 (2009) 152-155.

[205] B. Shen, H. Men, A. Inoue, Fe-based bulk glassy alloy composite containing in situ formed α-(Fe,Co) and (Fe,Co)23B6 microcrystalline grains, Applied Physics Letters, 89 (2006) 101915.

[206] S.-f. Guo, J.-f. Wang, H.-j. Zhang, S.-h. Xie, Enhanced plasticity of Fe-based bulk metallic glass by tailoring microstructure, Transactions of Nonferrous Metals Society of China, 22 (2012) 348-353.

[207] T.D. Bennett, S. Horike, Liquid, glass and amorphous solid states of coordination polymers and metal–organic frameworks, Nature Reviews Materials, 3 (2018) 431-440.

[208] M.M. Trexler, N.N. Thadhani, Mechanical properties of bulk metallic glasses, Progress in Materials Science, 55 (2010) 759-839.

[209] J. L. Bouvard, D. K. Ward, D. Hossain, S. Nouranian, E. B. Marin, M.F. Horstemeyer, Review of Hierarchical Multiscale Modeling to Describe the Mechanical Behavior of Amorphous Polymers, Journal of Engineering Materials and Technology, 131 (2009) 1-15.

[210] E. Axinte, Glasses as engineering materials: A review, Materials & Design, 32 (2011) 1717-1732.

[211] J. Li, G. Doubek, L. McMillon-Brown, A.D. Taylor, Recent Advances in Metallic Glass Nanostructures: Synthesis Strategies and Electrocatalytic Applications, Advanced Materials, 31 (2019) 1802120.

[212] D. Loke, T.H. Lee, W.J. Wang, L.P. Shi, R. Zhao, Y.C. Yeo, T.C. Chong, S.R. Elliott, Breaking the Speed Limits of Phase-Change Memory, Science, 336 (2012) 1566-1569.

[213] J. Hegeds, S.R. Elliott, Microscopic origin of the fast crystallization ability of Ge-Sb-Te phase-change memory materials, Nature Materials, 7 (2008) 399-405.

[214] M. Wuttig, N. Yamada, Phase-change materials for rewritable data storage, Nature Materials, 6 824-832.

[215] K.V. Sreekanth, Q. Ouyang, S. Sreejith, S. Zeng, W. Lishu, E. Ilker, W. Dong, M. ElKabbash, Y. Ting, C.T. Lim, M. Hinczewski, G. Strangi, K.-T. Yong, R.E. Simpson, R. Singh, Phase-Change-Material-Based Low-Loss Visible-Frequency Hyperbolic Metamaterials for Ultrasensitive Label-Free Biosensing, Advanced Optical Materials, 7 (2019) 1900081.

[216] E. Sharma, H.H. Hegazy, V. Sharma, P. Sharma, Topological behavior and glassy framework of GeTeSeGa chalcogenide glasses, Physica B: Condensed Matter, 562 (2019) 100-106.

[217] Y. Chen, R. Wang, X. Shen, J. Wang, T. Xu, New Methods Versus Old Questions: Crystallization Kinetics of S, Se, and Te, Crystal Growth & Design, 19 (2019) 1103-1110.

[218] D. Biswas, L.S. Singh, A.S. Das, S. Bhattacharya, An investigation of S–Se–Te semiconducting glassy alloys: Structural characterization and electrical conductivity, Journal of Non-Crystalline Solids, 510 (2019) 101-111.

[219] B.J. Eggleton, B. Luther-Davies, K. Richardson, Chalcogenide photonics, Nature Photonics, 5 (2011) 141-148.

[220] C. Lin, C. Rüssel, S. Dai, Chalcogenide glass-ceramics: Functional design and crystallization mechanism, Progress in Materials Science, 93 (2018) 1-44.

[221] A. Inoue, Bulk glassy and nonequilibrium crystalline alloys by stabilization of supercooled liquid: fabrication, functional properties and applications (Part 1), Proceedings of the Japan Academy, Series B, 81 (2005) 156-171.

[222] N. Yodoshi, R. Yamada, A. Kawasaki, A. Makino, Micro viscous flow processing of Fe-based metallic glassy particles, Journal of Alloys and Compounds, 615 (2014) S61-S66.

[223] R. Hasegawa, Applications of amorphous magnetic alloys in electronic devices, Journal of Non-Crystalline Solids, 287 (2001) 405-412.

[224] C. Lei, J. Lei, Z. Yang, Y. Zhou, Improved micro fluxgate sensor with double-layer Fe-based amorphous core, Microsystem Technologies, 19 (2013) 167-172.

[225] P. Meagher, E.D. O'Cearbhaill, J.H. Byrne, D.J. Browne, Bulk Metallic Glasses for Implantable Medical Devices and Surgical Tools, Advanced Materials, 28 (2016) 5755-5762.

[226] N. Hua, W. Chen, Q. Wang, Q. Guo, Y. Huang, T. Zhang, Tribocorrosion behaviors of a biodegradable $Mg_{65}Zn_{30}Ca_5$ bulk metallic glass for potential biomedical implant applications, Journal of Alloys and Compounds, 745 (2018) 111-120.

[227] W.L. Johnson, Bulk amorphous metal—An emerging engineering material, JOM, 54 (2002) 40-43.

[228] L. Huang, C. Pu, R.K. Fisher, D.J.H. Mountain, Y. Gao, P.K. Liaw, W. Zhang, W. He, A Zr-based bulk metallic glass for future stent applications: Materials properties, finite element modeling, and in vitro human vascular cell response, Acta Biomaterialia, 25 (2015) 356-368.

[229] M. Dittmer, C. Rüssel, Colorless and high strength $MgO/Al_2O_3/SiO_2$ glass–ceramic dental material using zirconia as nucleating agent, Journal of Biomedical Materials Research Part B: Applied Biomaterials, 100B (2012) 463-470.

[230] T. Irifune, K. Kawakami, T. Arimoto, H. Ohfuji, T. Kunimoto, T. Shinmei, Pressure-induced nano-crystallization of silicate garnets from glass, Nature Communications, 7 (2016) 13753.

[231] G.R. Khanolkar, M.B. Rauls, J.P. Kelly, O.A. Graeve, A.M. Hodge, V. Eliasson, Shock Wave Response of Iron-based In Situ Metallic Glass Matrix Composites, Scientific Reports, 6 (2016) 22568.

[232] C.C. Cao, Y.G. Wang, L. Zhu, Y. Meng, X.B. Zhai, Y.D. Dai, J.K. Chen, F.M. Pan, Local structure, nucleation sites and crystallization behavior and their effects on magnetic properties of $Fe_{81}Si_x B_{10}P_{8-x}Cu_1$ (x = 0~8), Scientific reports, 8 (2018) 1243-1243.

[233] V. Zhukova, J.M. Blanco, M. Ipatov, M. Churyukanova, S. Taskaev, A. Zhukov, Tailoring of magnetoimpedance effect and magnetic softness of Fe-rich glass-coated microwires by stress-annealing, Scientific Reports, 8 (2018) 3202.

[234] Y. Xu, Y. Sun, X. Dai, B. Liao, S. Zhou, D. Chen, Microstructure and magnetic properties of amorphous/nanocrystalline Ti50Fe50 alloys prepared by mechanical alloying, Journal of Materials Research and Technology, 8 (2019) 2486-2493.

[235] M.M. Vasić, T. Žák, N. Pizúrová, P. Roupcová, D.M. Minić, D.M. Minić, Thermally induced microstructural transformations and anti-corrosion properties of $Co_{70}Fe_5Si_{10}B_{15}$ amorphous alloy, Journal of Non-Crystalline Solids, 500 (2018) 326-335.

[236] G.S. Frankel, J.D. Vienna, J. Lian, J.R. Scully, S. Gin, J.V. Ryan, J. Wang, S.H. Kim, W. Windl, J. Du, A comparative review of the aqueous corrosion of glasses, crystalline ceramics, and metals, npj Materials Degradation, 2 (2018) 15.

[237] X. Zhou, K.D. Ralston, K.J. Laws, J.D. Cao, R.K. Gupta, M. Ferry, N. Birbilis, Effect of the Degree of Crystallinity on the Electrochemical Behavior of $Mg_{65}Cu_{25}Y_{10}$ and $Mg_{70}Zn_{25}Ca_5$ Bulk Metallic Glasses, Corrosion, 69 (2013) 781-792.

[238] G. Höhne, W. F. Hemminger, H.-J. Flammersheim, Differential Scanning Calorimetry, 2 ed. ed., Springer-Verlag Berlin Heidelberg, 2003.

[239] J.E.K. Schawe, Remarks regarding the determination of the initial crystallinity by temperature modulated DSC, Thermochimica Acta, 657 (2017) 151-155.

[240] P.H. Hermans, A. Weidinger, Quantitative X-Ray Investigations on the Crystallinity of Cellulose Fibers. A Background Analysis, Journal of Applied Physics, 19 (1948) 491-506.

[241] P.H. Hermans, A. Weidinger, Quantitative investigation of x-ray diffraction by “amorphous” polymers and some other noncrystalline substances, Journal of Polymer Science, 5 (1950) 269-281.

[242] A. Saleki-Gerhardt, C. Ahlneck, G. Zografi, Assessment of disorder in crystalline solids, International Journal of Pharmaceutics, 101 (1994) 237-247.

[243] R. Suryanarayanan, X-ray powder diffractometry, In H. G. Brittain (ed.) ed., Physical Characterization of Pharmaceutical Sciences, Marcel Dekker, New York, 1995.

[244] C. Nunes, A. Mahendrasingam, R. Suryanarayanan, Quantification of Crystallinity in Substantially Amorphous Materials by Synchrotron X-ray Powder Diffractometry, Pharmaceutical Research, 22 (2005) 1942-1953.

[245] G.A. Stephenson, R.A. Forbes, S.M. Reutzel-Edens, Characterization of the solid state: quantitative issues, Advanced Drug Delivery Reviews, 48 (2001) 67-90.

[246] X. Zhou, D. Liu, H. Bu, L. Deng, H. Liu, P. Yuan, P. Du, H. Song, XRD-based quantitative analysis of clay minerals using reference intensity ratios, mineral intensity factors, Rietveld, and full pattern summation methods: A critical review, Solid Earth Sciences, 3 (2018) 16-29.

[247] M.M. Nowell, R.A. Witt, B.W. True, EBSD Sample Preparation: Techniques, Tips, and Tricks, Microscopy Today, 13 (2005) 44-49.

[248] D. Katrakova, F. Mücklich, Specimen preparation for electron backscatter diffraction - Part I: Metals, Praktische Metallographie/Practical Metallography, 38 (2001) 547-565.

[249] D. Katrakova, F. Mücklich, Specimen preparation for electron backscatter diffraction (EBSD) - Part II: Ceramics, Praktische Metallographie/Practical Metallography, 39 (2002) 644-662.

[250] T. Paul, A. Loganathan, A. Agarwal, S.P. Harimkar, Kinetics of isochronal crystallization in a Fe-based amorphous alloy, Journal of Alloys and Compounds, 753 (2018) 679-687.

[251] P. Ramasamy, M. Stoica, A.H. Taghvaei, K.G. Prashanth, R. Kumar, J. Eckert, Kinetic analysis of the non-isothermal crystallization process, magnetic and mechanical properties of FeCoBSiNb and FeCoBSiNbCu bulk metallic glasses, Journal of Applied Physics, 119 (2016) 073908.

[252] W.A. Johnson, R.F. Mehl, Reaction Kinetics in Processes of Nucleation and Growth, Transactions of the American Institute of Mining & Metallurgical Engineers, 135 (1939) 416-442.

[253] M. Avrami, Kinetics of Phase Change. I General Theory, The Journal of Chemical Physics, 7 (1939) 1103-1112.

[254] C.S. Ray, W. Huang, D.E. Day, Crystallization Kinetics of a Lithia–Silica Glass: Effect of Sample Characteristics and Thermal Analysis Measurement Techniques, Journal of the American Ceramic Society, 74 (1991) 60-66.

[255] J.E.K. Schawe, U. Hess, Influence of Moisture on the Glass Transition of A Spray-Dried Compound Using the Isosteptm Method, Journal of Thermal Analysis and Calorimetry, 68 (2002) 741-749.

[256] L.T.S. Sauerbrunn, Determination of Initial Crystallinity in Polymers by Modulated Differential Scanning Calorimetry, Amer. Lab, 27 (1995) 19-22.

[257] P. Roura, D. Sanchez-Rodriguez, J. Farjas, Measurement by differential scanning calorimetry of specific heat capacity variation due to crystallization: Application to amorphous silicon, Thermochimica Acta, 522 (2011) 161-165.

[258] G. Ferrer, C. Barreneche, A. Solé, I. Martorell, L.F. Cabeza, New proposed methodology for specific heat capacity determination of materials for thermal energy storage (TES) by DSC, Journal of Energy Storage, 11 (2017) 1-6.

[259] J.H. J. Farmer, S. Day, T. Lian, C-K. Saw, P. Hailey, J-S. Choi, R. Rebak The corrosion resistance of Fe-based amorphous metals: $Fe_{49.7}Cr_{17.7}Mn_{1.9}Mo_{7.4}W_{1.6}B_{15.2}C_{3.8}Si_{2.4}$ and other compositions, Mater Sci Tech-Assoc Iron Steel Tech, 4 (2007) 2285.

[260] J. Blink, J. Farmer, J. Choi, C. Saw, Applications in the Nuclear Industry for Thermal Spray Amorphous Metal and Ceramic Coatings, Metallurgical and Materials Transactions A, 40 (2009) 1344-1354.

[261] J. Farmer, J.-S. Choi, C. Saw, J. Haslam, D. Day, P. Hailey, T. Lian, R. Rebak, J. Perepezko, J. Payer, D. Branagan, B. Beardsley, A. D'amato, L. Aprigliano, Iron-Based Amorphous Metals: High-Performance Corrosion-Resistant Material Development, Metallurgical and Materials Transactions A, 40 (2009) 1289-1305.

[262] J.P. Kelly, S.M. Fuller, K. Seo, E. Novitskaya, V. Eliasson, A.M. Hodge, O.A. Graeve, Designing in situ and ex situ bulk metallic glass composites via spark plasma sintering in the super cooled liquid state, Materials & Design, 93 (2016) 26-38.

[263] J.E. Garay, Current-Activated, Pressure-Assisted Densification of Materials, Annual Review of Materials Research, 40 (2010) 445-468.

[264] C.J. Lee, Y.H. Lai, C.W. Tang, J.C. Huang, J.S.C. Jang, Mechanical Behavior of Au-Based Metallic Glass in Micro-Scale at Ambient and Elevated Temperatures, Materials Transactions, 50 (2009) 2795-2800.

[265] D.S. Smith, N.J. Lybeck, J.K. Wright, R.N. Wright, Thermophysical properties of Alloy 709, Nuclear Engineering and Design, 322 (2017) 331-335.

[266] H.S. Chen, The influence of structural relaxation on the density and Young's modulus of metallic glasses, Journal of Applied Physics, 49 (1978) 3289-3291.

[267] T. Egami, Structural relaxation in amorphous alloys - compositional short range ordering, Materials Research Bulletin, 13 (1978) 557-562.

[268] A.L. Greer, Structural relaxation and atomic transport in amorphous alloys, H.H. Liebermann (Ed.), Rapidly solidified alloys, Marcel Dekker, New York, US, 1993.

[269] A. Van Den Beukel, S. Radelaar, On the kinetics of structural relaxation in metallic glasses, Acta Metallurgica, 31 (1983) 419-427.

[270] S.L. Shamblin, G. Zografi, Enthalpy relaxation in binary amorphous mixtures containing sucrose, Pharmaceutical research, 15 (1998) 1828-1834.

[271] B.C. Hancock, S.L. Shamblin, G. Zografi, Molecular Mobility of Amorphous Pharmaceutical Solids Below Their Glass Transition Temperatures, Pharmaceutical Research, 12 (1995) 799-806.

[272] R. Surana, A. Pyne, R. Suryanarayanan, Effect of Preparation Method on Physical Properties of Amorphous Trehalose, Pharmaceutical Research, 21 (2004) 1167-1176.

[273] D.J. Wang, Y.J. Huang, L.Z. Wu, J. Shen, Mechanical behaviors of diamond reinforced Ti-based bulk metallic glassy composites prepared by spark plasma sintering, Materials Science and Engineering: A, 560 (2013) 841-846.

[274] Y. Huang, Y.L. Chiu, J. Shen, J.J.J. Chen, J. Sun, Nanoindentation study of Ti-based metallic glasses, Journal of Alloys and Compounds, 479 (2009) 121-128.

[275] A. van den Beukel, J. Sietsma, The glass transition as a free volume related kinetic phenomenon, Acta Metallurgica et Materialia, 38 (1990) 383-389.

[276] A. Slipenyuk, J. Eckert, Correlation between enthalpy change and free volume reduction during structural relaxation of $Zr_{55}Cu_{30}Al_{10}Ni_5$ metallic glass, Scripta Materialia, 50 (2004) 39-44.

[277] A. Ananthanarayanan, G. Tricot, G.P. Kothiyal, L. Montagne, A Comparative Overview of Glass-Ceramic Characterization by MAS-NMR and XRD, Critical Reviews in Solid State and Materials Sciences, 36 (2011) 229-241.

[278] J.C.f.G.i.M. (JCGM), Evaluation of Measurement Data—Guide to the Expression of Uncertainty in Measurement (GUM 1995 with Minor Corrections), (2008).

[279] https://www.socscistatistics.com/tests/pearson/default2.aspx (accessed on 6 October 2019). in.

[280] O.G. Arash Yazdani, A Method to Quantify the Degree of Crystallization in Amorphous Metals: A Differential Scanning Calorimetry Study Under prep.

[281] I.-C. Cheng, J.P. Kelly, E. Novitskaya, V. Eliasson, A.M. Hodge, O.A. Graeve, Mechanical Properties of an Fe-Based SAM2×5-630 Metallic Glass Matrix Composite with Tungsten Particle Additions, Advanced Engineering Materials, 20 (2018) 1800023.

[282] D.R. Maddala, R.J. Hebert, Sliding wear behavior of $Fe_{50-x}Cr_{15}Mo_{14}C_{15}B_6Er_x$ (x=0, 1, 2at%) bulk metallic glass, Wear, 294-295 (2012) 246-256.

[283] S. Lesz, Effect of cooling rates on the structure, density and micro-indentation behavior of the Fe, Co-based bulk metallic glass, Materials Characterization, 124 (2017) 97-106.

[284] Y. Liu, H. Bei, C.T. Liu, E.P. George, Cooling-rate induced softening in a $Zr_{50}Cu_{50}$ bulk metallic glass, Applied Physics Letters, 90 (2007) 071909.

[285] M. Song, Y.Y. Sun, Y.H. He, S.F. Guo, Structure related hardness and elastic modulus of bulk metallic glass, Journal of Applied Physics, 111 (2012) 053518.

[286] W. Chen, Z. Liu, J. Ketkaew, R.M.O. Mota, S.-H. Kim, M. Power, W. Samela, J. Schroers, Flaw tolerance of metallic glasses, Acta Materialia, 107 (2016) 220-228.

[287] M.D. Demetriou, M.E. Launey, G. Garrett, J.P. Schramm, D.C. Hofmann, W.L. Johnson, R.O. Ritchie, A damage-tolerant glass, Nature Materials, 10 (2011) 123-128.

[288] J. Xu, U. Ramamurty, E. Ma, The fracture toughness of bulk metallic glasses, JOM, 62 (2010) 10-18.

[289] P. Lowhaphandu, J.J. Lewandowski, Fracture toughness and notched toughness of bulk amorphous alloy: Zr-Ti-Ni-Cu-Be, Scripta Materialia, 38 (1998) 1811-1817.

[290] R.D. Conner, A.J. Rosakis, W.L. Johnson, D.M. Owen, Fracture toughness determination for a beryllium-bearing bulk metallic glass, Scripta Materialia, 37 (1997) 1373-1378.

[291] C.J. Gilbert, V. Schroeder, R.O. Ritchie, Mechanisms for fracture and fatigue-crack propagation in a bulk metallic glass, Metallurgical and Materials Transactions A, 30 (1999) 1739-1753.

[292] D. Suh, R.H. Dauskardt, Effects of open-volume regions on relaxation time scales and fracture behavior of a Zr–Ti–Ni–Cu–Be bulk metallic glass, Journal of Non-Crystalline Solids, 317 (2003) 181-186.

[293] K.M. Flores, R.H. Dauskardt, Enhanced toughness due to stable crack tip damage zones in bulk metallic glass, Scripta Materialia, 41 (1999) 937-943.

[294] K.M. Flores, R.H. Dauskardt, Crack-tip plasticity in bulk metallic glasses, Materials Science and Engineering: A, 319-321 (2001) 511-515.

[295] K.M. Flores, R.H. Dauskardt, Mode II fracture behavior of a Zr-based bulk metallic glass, Journal of the Mechanics and Physics of Solids, 54 (2006) 2418-2435.

[296] P. Tandaiya, U. Ramamurty, R. Narasimhan, Mixed mode (I and II) crack tip fields in bulk metallic glasses, Journal of the Mechanics and Physics of Solids, 57 (2009) 1880-1897.

[297] R.L. Narayan, P. Tandaiya, G.R. Garrett, M.D. Demetriou, U. Ramamurty, On the variability in fracture toughness of ‘ductile’ bulk metallic glasses, Scripta Materialia, 102 (2015) 75-78.

[298] B. Gludovatz, S.E. Naleway, R.O. Ritchie, J.J. Kruzic, Size-dependent fracture toughness of bulk metallic glasses, Acta Materialia, 70 (2014) 198-207.

[299] S.V. Madge, Toughness of Bulk Metallic Glasses Metals, Metals, 5 (2015) 1279-1305.

[300] B. Lawn, Fracture of Brittle Solids, 2 ed., Cambridge University Press, Cambridge, 1993.

[301] S. Palmqvist, Method of determining the toughness of brittle materials particularly sintered carbides, Jernkontorets Annaler 141 (1957) 300-305.

[302] G.R. Antis, P. Chantikul, B.R. Lawn, D.B. Marshal, A Critical Evaluation of Indentation Techniques for Measuring Fracture Toughness: I, Direct Crack Measurements, Journal of the American Ceramic Society, 64 (1981) 533-538.

[303] R.M. K. Niihara, D. P. H. Hasselman, Evaluation ofKIc of brittle solids by the indentation method with low crack-to-indent ratios, Journal of Materials Science Letters, 1 (1982) 13-16.

[304] B.R. Lawn, A.G. Evans, D.B. Marshal, Elastic/Plastic Indentation Damage in Ceramics: The Median/Radial Crack System, Journal of the American Ceramic Society, 63 (1980) 574-581.

[305] K. Niihara, R. Morena, D.P.H. Hasselman, Evaluation ofKIc of brittle solids by the indentation method with low crack-to-indent ratios, Journal of Materials Science Letters, 1 (1982) 13-16.

[306] P.A. Hess, S.J. Poon, G.J. Shiflet, R.H. Dauskardt, Indentation fracture toughness of amorphous steel, Journal of Materials Research, 20 (2005) 783-786.

[307] P. Wesseling, T.G. Nieh, W.H. Wang, J.J. Lewandowski, Preliminary assessment of flow, notch toughness, and high temperature behavior of $Cu_{60}Zr_{20}Hf_{10}Ti_{10}$ bulk metallic glass, Scripta Materialia, 51 (2004) 151-154.

[308] X.K. Xi, D.Q. Zhao, M.X. Pan, W.H. Wang, Y. Wu, J.J. Lewandowski, Fracture of brittle metallic glasses: brittleness or plasticity, Physical Review Letter, 94 (2005) 125510.

[309] A.S. Argon, M. Salama, The mechanism of fracture in glassy materials capable of some inelastic deformation, Materials Science and Engineering, 23 (1976) 219-230.

[310] K.M. Flores, R.H. Dauskardt, Local heating associated with crack tip plasticity in Zr–Ti–Ni–Cu–Be bulk amorphous metals, Journal of Materials Research, 14 (1999) 638-643.

[311] A. Inoue, X.M. Wang, Bulk amorphous FC20 (Fe–C–Si) alloys with small amounts of B and their crystallized structure and mechanical properties, Acta Materialia, 48 (2000) 1383-1395.

[312] S. Cardinal, J.M. Pelletier, G.Q. Xie, F. Mercier, F. Dalmas, Enhanced compressive plasticity in a Cu-Zr-Al – Based metallic glass composite, Journal of Alloys and Compounds, 782 (2019) 59-68.

[313] S.M. WIEDERHORN, Fracture Surface Energy of Glass, Journal of the American Ceramic Society, 52 (1969) 99-105.

[314] H. Kimura, T. Masumoto, Deformation and fracture of an amorphous Pd□Cu□Si alloy in V-notch bending tests—II: Ductile-brittle transition, Acta Metallurgica, 28 (1980) 1677-1693.

[315] N. Nagendra, U. Ramamurty, T.T. Goh, Y. Li, Effect of crystallinity on the impact toughness of a La-based bulk metallic glass, Acta Materialia, 48 (2000) 2603-2615.

[316] C.H. Shek, G.M. Lin, K.L. Lee, J.K.L. Lai, Fractal fracture of amorphous $Fe_{46}Ni_{32}V_2Si_{14}B_6$ alloy, Journal of Non-Crystalline Solids, 224 (1998) 244-248.

[317] G.N. Greaves, A.L. Greer, R.S. Lakes, T. Rouxel, Poisson's ratio and modern materials, Nature Materials, 10 (2011) 823-837.

[318] R. LAKES, Foam Structures with a Negative Poisson's Ratio, Science, 235 (1987) 1038-1040.

[319] A. Kelly, W.R. Tyson, A.H. Cottrell, Ductile and brittle crystals, The Philosophical Magazine: A Journal of Theoretical Experimental and Applied Physics, 15 (1967) 567-586.

[320] M.Q. Jiang, L.H. Dai, Short-range-order effects on intrinsic plasticity of metallic glasses, Philosophical Magazine Letters, 90 (2010) 269-277.

[321] T. Rouxel, Elastic Properties and Short-to Medium-Range Order in Glasses, Journal of the American Ceramic Society, 90 (2007) 3019-3039.

[322] A. Fukumoto, First-principles pseudopotential calculations of the elastic properties of diamond, Si, and Ge, Phys Rev B Condens Matter, 42 (1990) 7462-7469.

[323] A. Makishima, J.D. Mackenzie, Calculation of bulk modulus, shear modulus and Poisson's ratio of glass, Journal of Non-Crystalline Solids, 17 (1975) 147-157.

[324] C. Zha, R.J. Hemley, H. Mao, T.S. Duffy, C. Meade, Acoustic velocities and refractive index of SiO_2 glass to 57.5 GPa by Brillouin scattering, Phys Rev B Condens Matter, 50 (1994) 13105-13112.

[325] S.M. Antao, C.J. Benmore, B. Li, L. Wang, E. Bychkov, J.B. Parise, Network rigidity in $GeSe_2$ glass at high pressure, Phys Rev Lett, 100 (2008) 115501.

[326] J. Nicholas, S. Sinogeikin, J. Kieffer, J. Bass, A high pressure Brillouin scattering study of vitreous boron oxide up to 57GPa, Journal of Non-Crystalline Solids, 349 (2004) 30-34.

[327] T. Rouxel, H. Ji, J.P. Guin, F. Augereau, B. Rufflé, Indentation deformation mechanism in glass: Densification versus shear flow, Journal of Applied Physics, 107 (2010) 094903.

[328] T. Rouxel, H. Ji, T. Hammouda, A. Moréac, Poisson's ratio and the densification of glass under high pressure, Phys Rev Lett, 100 (2008) 225501.

[329] J.D. Mackenzie, High-Pressure Effects on Oxide Glasses: I, Densification in Rigid State, Journal of the American Ceramic Society, 46 (1963) 461-470.

[330] S. Yoshida, S. Isono, J. Matsuoka, N. Soga, Shrinkage Behavior of Knoop Indentations in Silica and Soda–Lime–Silica Glasses, Journal of the American Ceramic Society, 84 (2001) 2141-2143.

[331] W.L. Johnson, K. Samwer, A universal criterion for plastic yielding of metallic glasses with a (T/T_g) 2/3 temperature dependence, Phys Rev Lett, 95 (2005) 195501.

[332] H.A. Davies, B.G. Lewis, A generalised kinetic approach to metallic glass formation, Scripta Metallurgica, 9 (1975) 1107-1112.

[333] B. Shen, A. Inoue, C. Chang, Superhigh strength and good soft-magnetic properties of (Fe,Co)–B–Si–Nb bulk glassy alloys with high glass-forming ability, Applied Physics Letters, 85 (2004) 4911-4913.

[334] M. Stoica, J. Eckert, S. Roth, Z.F. Zhang, L. Schultz, W.H. Wang, Mechanical behavior of $Fe_{65.5}Cr_4Mo_4Ga_4P_{12}C_5B_{5.5}$ bulk metallic glass, Intermetallics, 13 (2005) 764-769.

[335] F. Liu, S. Pang, R. Li, T. Zhang, Ductile Fe–Mo–P–C–B–Si bulk metallic glasses with high saturation magnetization, Journal of Alloys and Compounds, 483 (2009) 613-615.

[336] J. Man Park, D. Hyang Kim, M. Stoica, N. Mattern, R. Li, J. Eckert, The influence of in situ formed precipitates on the plasticity of Fe–Nb–B–Cu bulk metallic glasses, Journal of Materials Research, 26 (2011) 2080-2086.

[337] D.-d. Liang, X.-s. Wei, C.-t. Chang, J.-w. Li, X.-m. Wang, J. Shen, Effect of W addition on the glass forming ability and mechanical properties of Fe-based metallic glass, Journal of Alloys and Compounds, 731 (2018) 1146-1150.

[338] Y.X. Geng, X. Lin, J. Li, S.M. Fan, H.B. Ju, L.H. Yu, J.H. Xu, Y.M. Wang, Super-high hardness of (Fe,Co)-B-Si-Zr/Hf bulk glassy alloys, Journal of Alloys and Compounds, 753 (2018) 351-355.

[339] G. Kumar, H.X. Tang, J. Schroers, Nanomoulding with amorphous metals, Nature, 457 (2009) 868-872.

[340] Y.-C. Lin, Y.-C. Tsai, T. Ono, P. Liu, M. Esashi, T. Gessner, M. Chen, Metallic Glass as a Mechanical Material for Microscanners, Advanced Functional Materials, 25 (2015) 5677-5682.

[341] J. Schroers, T. Nguyen, S. O'Keeffe, A. Desai, Thermoplastic forming of bulk metallic glass—Applications for MEMS and microstructure fabrication, Materials Science and Engineering: A, 449-451 (2007) 898-902.

[342] J. Michler, K. Wasmer, S. Meier, F. Östlund, K. Leifer, Plastic deformation of gallium arsenide micropillars under uniaxial compression at room temperature, Applied Physics Letters, 90 (2007) 043123.

[343] A. Dubach, R. Raghavan, J.F. Löffler, J. Michler, U. Ramamurty, Micropillar compression studies on a bulk metallic glass in different structural states, Scripta Materialia, 60 (2009) 567-570.

[344] O.V. Kuzmin, Y.T. Pei, C.Q. Chen, J.T.M. De Hosson, Intrinsic and extrinsic size effects in the deformation of metallic glass nanopillars, Acta Materialia, 60 (2012) 889-898.

[345] F. Östlund, P.R. Howie, R. Ghisleni, S. Korte, K. Leifer, W.J. Clegg, J. Michler, Ductile–brittle transition in micropillar compression of GaAs at room temperature, Philosophical Magazine, 91 (2011) 1190-1199.

[346] J.M. Wheeler, R. Raghavan, J. Michler, Temperature invariant flow stress during microcompression of a Zr-based bulk metallic glass, Scripta Materialia, 67 (2012) 125-128.

[347] A. Bharathula, S.-W. Lee, W.J. Wright, K.M. Flores, Compression testing of metallic glass at small length scales: Effects on deformation mode and stability, Acta Materialia, 58 (2010) 5789-5796.

[348] Y.-Y. Zhao, E. Ma, J. Xu, Reliability of compressive fracture strength of Mg–Zn–Ca bulk metallic glasses: Flaw sensitivity and Weibull statistics, Scripta Materialia, 58 (2008) 496-499.

[349] C.A. Schuh, A.C. Lund, T.G. Nieh, New regime of homogeneous flow in the deformation map of metallic glasses: elevated temperature nanoindentation experiments and mechanistic modeling, Acta Materialia, 52 (2004) 5879-5891.

[350] C.A. Schuh, T.G. Nieh, A nanoindentation study of serrated flow in bulk metallic glasses, Acta Materialia, 51 (2003) 87-99.

[351] C. Chen, Y. Pei, J.T.M.D. Hosson, A statistical physics consideration about the strength of small size metallic glass pillars, Journal of Physics: Conference Series, 240 (2010) 012156.

[352] Y.H. Lai, C.J. Lee, Y.T. Cheng, H.S. Chou, H.M. Chen, X.H. Du, C.I. Chang, J.C. Huang, S.R. Jian, J.S.C. Jang, T.G. Nieh, Bulk and microscale compressive behavior of a Zr-based metallic glass, Scripta Materialia, 58 (2008) 890-893.

[353] B.E. Schuster, Q. Wei, M.H. Ervin, S.O. Hruszkewycz, M.K. Miller, T.C. Hufnagel, K.T. Ramesh, Bulk and microscale compressive properties of a Pd-based metallic glass, Scripta Materialia, 57 (2007) 517-520.

[354] D. Kiener, C. Motz, G. Dehm, Micro-compression testing: A critical discussion of experimental constraints, Materials Science and Engineering: A, 505 (2009) 79-87.

[355] P.A. Shade, R. Wheeler, Y.S. Choi, M.D. Uchic, D.M. Dimiduk, H.L. Fraser, A combined experimental and simulation study to examine lateral constraint effects on microcompression of single-slip oriented single crystals, Acta Materialia, 57 (2009) 4580-4587.

[356] D. Jang, C.T. Gross, J.R. Greer, Effects of size on the strength and deformation mechanism in Zr-based metallic glasses, International Journal of Plasticity, 27 (2011) 858-867.

[357] X.L. Wu, Y.Z. Guo, Q. Wei, W.H. Wang, Prevalence of shear banding in compression of $Zr_{41}Ti_{14}Cu_{12.5}Ni_{10}Be_{22.5}$ pillars as small as 150nm in diameter, Acta Materialia, 57 (2009) 3562-3571.

[358] D. Jang, J.R. Greer, Transition from a strong-yet-brittle to a stronger-and-ductile state by size reduction of metallic glasses, Nature Materials, 9 (2010) 215-219.

[359] C.A. Volkert, A. Donohue, F. Spaepen, Effect of sample size on deformation in amorphous metals, Journal of Applied Physics, 103 (2008) 083539.

[360] J.C. Ye, J. Lu, Y. Yang, P.K. Liaw, Extraction of bulk metallic-glass yield strengths using tapered micropillars in micro-compression experiments, Intermetallics, 18 (2010) 385-393.

[361] H.B. Ke, B.A. Sun, C.T. Liu, Y. Yang, Effect of size and base-element on the jerky flow dynamics in metallic glass, Acta Materialia, 63 (2014) 180-190.

[362] Y. Lu, Y. Huang, J. Wu, Laser additive manufacturing of structural-graded bulk metallic glass, Journal of Alloys and Compounds, 766 (2018) 506-510.

[363] F. Sıkan, S.E. Atabay, A. Motallebzadeh, S. Özerinç, I. Kalay, Y.E. Kalay, Effect of Sm on thermal and mechanical properties of Cu-Zr-Al bulk metallic glasses, Materials Science and Engineering: A, 743 (2019) 168-174.

[364] J.T.M.D. Hosson, Advances in Transmission Electron Microscopy: In Situ Straining and In Situ Compression Experiments on Metallic Glasses, Microscopy Research and Technology Technique, 72 (2009) 250–260.

[365] M.C. Liu, J.C. Huang, Y.T. Fong, S.P. Ju, X.H. Du, H.J. Pei, T.G. Nieh, Assessing the interfacial strength of an amorphous–crystalline interface, Acta Materialia, 61 (2013) 3304-3313.

[366] Z.Y. Liu, Y. Yang, S. Guo, X.J. Liu, J. Lu, Y.H. Liu, C.T. Liu, Cooling rate effect on Young's modulus and hardness of a Zr-based metallic glass, Journal of Alloys and Compounds, 509 (2011) 3269-3273.

[367] S. González, P. Pérez, E. Rossinyol, S. Suriñach, M. Dolors Baró, E. Pellicer, J. Sort, Drastic influence of minor Fe or Co additions on the glass forming ability, martensitic transformations and mechanical properties of shape memory Zr–Cu–Al bulk metallic glass composites, Science and Technology of Advanced Materials, 15 (2014) 035015.

[368] D. Jang, R. Maaß, G. Wang, P.K. Liaw, J.R. Greer, Fatigue deformation of microsized metallic glasses, Scripta Materialia, 68 (2013) 773-776.

[369] H.S. Chou, X.H. Du, C.J. Lee, J.C. Huang, Enhanced mechanical properties of multilayered micropillars of amorphous ZrCuTi and nanocrystalline Ta layers, Intermetallics, 19 (2011) 1047-1051.

[370] F.C. Li, T.Y. Wang, Q.F. He, B.A. Sun, C.Y. Guo, T. Feng, Y. Yang, Micromechanical mechanism of yielding in dual nano-phase metallic glass, Scripta Materialia, 154 (2018) 186-191.

[371] C.C. Wang, J. Ding, Y.Q. Cheng, J.C. Wan, L. Tian, J. Sun, Z.W. Shan, J. Li, E. Ma, Sample size matters for $Al_{88}Fe_7Gd_5$ metallic glass: Smaller is stronger, Acta Materialia, 60 (2012) 5370-5379.

[372] S. Cheng, X.-L. Wang, H. Choo, P.K. Liaw, Global melting of $Zr_{57}Ti_5Ni_8Cu_{20}Al_{10}$ bulk metallic glass under microcompression, Applied Physics Letters, 91 (2007) 201917.

[373] Q. Zheng, S. Cheng, J.H. Strader, E. Ma, J. Xu, Critical size and strength of the best bulk metallic glass former in the Mg–Cu–Gd ternary system, Scripta Materialia, 56 (2007) 161-164.

[374] S. Korte, W.J. Clegg, Micropillar compression of ceramics at elevated temperatures, Scripta Materialia, 60 (2009) 807-810.

[375] H. Bei, S. Shim, M.K. Miller, G.M. Pharr, E.P. George, Effects of focused ion beam milling on the nanomechanical behavior of a molybdenum-alloy single crystal, Applied Physics Letters, 91 (2007) 111915.

[376] C.J. Lee, Y.H. Lai, J.C. Huang, X.H. Du, L. Wang, T.G. Nieh, Strength variation and cast defect distribution in metallic glasses, Scripta Materialia, 63 (2010) 105-108.

[377] W.F. Wu, Y. Li, C.A. Schuh, Strength, plasticity and brittleness of bulk metallic glasses under compression: statistical and geometric effects, Philosophical Magazine, 88 (2008) 71-89.

[378] C.J. Lee, J.C. Huang, T.G. Nieh, Sample size effect and microcompression of $Mg_{65}Cu_{25}Gd_{10}$ metallic glass, Applied Physics Letters, 91 (2007) 161913.